Development and characterization of a Penning ion source using helium

by

Nicolas Savard

B.Sc., McGill University, 2014

M.Sc., The University of Victoria, 2016

A THESIS SUBMITTED IN PARTIAL FULFILLMENT
OF THE REQUIREMENTS FOR THE DEGREE OF

Doctor of Philosophy

in

THE FACULTY OF GRADUATE AND POSTDOCTORAL STUDIES

(Physics)

The University of British Columbia

(Vancouver)

April 2022

The following individuals certify that they have read, and recommend to the Faculty of Graduate and Postdoctoral Studies for acceptance, the thesis entitled:

Development and characterization of a Penning ion source using helium

submitted by **Nicolas Savard** in partial fulfillment of the requirements for the degree of **Doctor of Philosophy** in **Physics**.

Examining Committee:

Reiner Kruecken, Professor, Physics, UBC
Supervisor

Morgan Dehnel, Adjunct Professor, Physics, UBCO
Co-Supervisor

Janis McKenna, Professor, Physics, UBC
Supervisory Committee Member

Mark Thachuk, Associate Professor, Chemistry, UBC
University Examiner

Richard Johnson, Emeritus Professor, Physics, UBC
University Examiner

Additional Supervisory Committee Members:

Jeremy Heyl, Professor, Physics, UBC
Supervisory Committee Member

Thomas Mattison, Associate Professor, Physics, UBC
Supervisory Committee Member

Abstract

Penning ion sources are relatively inexpensive and compact ion sources, and therefore could be used to replace costly Electron Cyclotron Resonance ion sources for high current α-particle production in medical accelerators. To be able to optimize a Penning ion source for high current α-particle production, one first needs to be able to characterize and understand the plasma dynamics within it under helium operation. For this reason, a test stand and prototype Penning ion source is developed which allows for the confining magnetic field (0.1 - 0.9 T), inlet helium gas flow (5-25 sccm), arc voltage (1 - 2 kV), and extraction voltage ($\leq$ 15 kV) of the ion source to vary. This thesis describes the design and engineering of the Penning ion source using helium gas. In addition, plasma simulations using COMSOL Multiphysics™ are used to model how this ion source responds to various input parameters, and diagnostics tools such as optical emission spectroscopy are used to measure the plasma properties as these parameters are varied. The latter was done by creating a collisional-radiative model which compares well with Yacora on the Web from IPP Garching and improves upon it by adding radiation trapping approximations. The optical emission spectroscopy diagnostic is compared to Langmuir probe measurements in a TRIUMF-licensed Volume Cusp ion source to verify trends observed using this diagnostic. It is found that the plasma simulations and optical emission spectroscopy diagnostics agree on observed trends of electron and ion density for each varied operational parameter. This is confirmed by observing the same trends when extracting the He^+ ions from the ion source. However, it is clear that the non-Maxwellian behavior of electrons can have a significant effect on plasma dynamics, which cannot be resolved with the current diagnostics or plasma models. Thus future studies will need to be performed to analyze the elec-

tron kinetics within the plasma to better determine how α particle density changes as a function of the various input parameters, and thus how to optimize the ion source for α production.

Lay Summary

This thesis describes the design and engineering of an ion source (called the Penning ion source), which is the source of ions in a particle accelerator. The purpose is to produce a certain type of particle, called an α-particle, with high intensity. This particle is used to produce radioisotopes which can be used for localized cancer treatments within the body. Accelerators currently use an expensive ion source to produce α-particles, and the accelerator community would like to replace these ion sources with cheaper options, such as the Penning ion source. In order to do this, we need to study the mechanisms of the Penning ion source to find out how to produce α-particles to the appropriate intensity to replace these expensive ion sources. This work is done in this thesis using experimental measurements, which are compared to simulations.

Preface

Most of the work conducted within this thesis was done at Buckley Systems Ltd. in Auckland NZ, which is where the Ion Source Test Facility (ISTF) is located. This was later shipped to D-Pace Inc. in Nelson BC in the last year of this thesis, where the rest of the work was completed.

A portion of chapter 3 describing the initial design of the ion source was presented as a poster at the 2018 IPAC [1]. I was responsible for the technical design and all physics simulations. In addition, the majority of assembly, setup, and programming of the Penning ion source system was done by myself. All writing was done by myself. Co-authors are D-Pace engineers who did the mechanical designs and took management responsibilities.

Most of chapter 3 describing the revised design was published in a conference proceedings at ICIS 2021 [2]. I did all the simulations and the initial CAD design for the ion source, which was completed by Alexey Groutso of Buckley Systems. I designed and tested the electron trap electrodes, and was responsible for writing the paper. Other co-authors gave advice and took management responsibilities.

Chapter 4 has not yet been published, but has been recently submitted to a journal as of March 21, 2022. I was responsible for everything done in this chapter.

Chapter 5 will be a poster presentation at a conference. I was responsible for everything done in this chapter.

Table of Contents

Abstract . . . . . **iii**

Lay Summary . . . . . **v**

Preface . . . . . **vi**

Table of Contents . . . . . **vii**

List of Tables . . . . . **xi**

List of Figures . . . . . **xii**

List of Abbreviations . . . . . **xviii**

List of Programs . . . . . **xx**

Acknowledgments . . . . . **xxi**

Dedication . . . . . **xxiii**

1 Introduction **1**

1.1 Accelerators for Medicine 1

1.1.1 α Production 2

1.2 Penning Ion Source 2

1.3 Purpose of PIG development 5

2 Theoretical Concepts **8**

2.1 Plasma Defined 8
2.2 Atomic Structure 8
2.2.1 Helium Structure 9
2.2.2 Spontaneous Emission 10
2.3 Electron Impact Collisions 11
2.3.1 Cross Sections and Rate Coefficients 11
2.3.2 Elastic Collisions 12
2.3.3 Coulomb Collisions 12
2.4 Charged Particle Losses 13
2.4.1 Electron-Ion Recombination 13
2.4.2 Wall Neutralization 14
2.5 Plasma Physics 14
2.5.1 Fluid Model 15
2.5.2 Plasma Confinement with Magnetic Fields 18
2.6 DC Discharges 19
2.6.1 Collisionless Sheath 20
2.6.2 Electron Cathode Emission 21

3 Ion Source System Design 24
3.1 Magnet Design 24
3.1.1 Magnet Simulations 26
3.2 Vacuum Box 30
3.3 Igniting and Sustaining a Plasma 33
3.4 First Ion Source Design 33
3.5 Second Ion Source design 37
3.5.1 Electrostatics 37
3.5.2 Ion Extraction 40
3.5.3 Electron Trapping 46
3.5.4 Cathode Heating 51
3.5.5 Materials 54

4 Plasma Diagnostics 56
4.1 Langmuir Probe 56

4.1.1 Non-Maxwellian Distributions . . . 57
4.2 Optical Emission Spectroscopy . . . 60
4.2.1 Optical Emission . . . 60
4.3 Spectroscopy 0-D Models . . . 62
4.3.1 Corona and Equilibrium Models . . . 62
4.3.2 Collisional-Radiative Model . . . 62
4.4 Helium CR Code . . . 65
4.4.1 Yacora on the Web . . . 65
4.4.2 Core Model . . . 66
4.4.3 Absorption and Radiation Trapping . . . 71
4.4.4 Yacora Comparison . . . 74
4.4.5 Effects of Radiation Trapping . . . 76
4.4.6 Comparison with n=10 States . . . 79
4.4.7 Effect of Non-Maxwellian Behavior . . . 81
4.5 Volume Cusp Ion Source Comparison . . . 84
4.5.1 Langmuir Probe Measurements . . . 85
4.5.2 OES system . . . 88
4.5.3 Langmuir and OES Comparison for Helium . . . 91
4.6 Cold Cathode Penning Ion Source . . . 101
4.6.1 OES Measurements . . . 103

5 Plasma Modeling . . . 110
5.1 Plasma Modeling in Ion Sources . . . 110
5.2 Comsol Plasma Model . . . 111
5.2.1 Particle Transport . . . 111
5.2.2 Magnetic Field Effects . . . 112
5.2.3 Heavy Particle Drift . . . 115
5.3 1-D Model . . . 115
5.3.1 1-D Results . . . 122
5.3.2 Applied 1-D Model . . . 125
5.3.3 Charged-Particle Tracing Ionization . . . 132
5.4 2-D Axi-Symmetric Model . . . 137
5.4.1 2-D Model Results . . . 141

5.4.2 Applied 2-D Model 146

6 Beam Extraction and Conclusion 152
6.1 Beam Extraction 152
6.2 Conclusion 160
6.2.1 Future studies 163

Bibliography 165

Appendix 173

List of Tables

Table 4.1 Index of each term in population column vector, along with its LS term, energy level (only up to three decimal places), and statistical weight g 68

Table 5.1 Reactions and their types in the COMSOL™ model. 118

List of Figures

Figure 1.1 Simplified schematic of a Penning ion source. 4

Figure 2.1 Spatial sheath profile example as a function of electron/ion density and electric potential. 21

Figure 2.2 Example transitions between various states of DC discharges. 23

Figure 3.1 Simplified schematic of ion source beam diagnostic. 25

Figure 3.2 Simulation model of magnet. 27

Figure 3.3 Volume-averaged radial diffusion coefficient ratio for electrons as a function of distance of ion source from center. 29

Figure 3.4 Example of Penning ion source extraction simulation at 0.4 T. 30

Figure 3.5 Cross section of Penning system with V-Box, magnet, ion source, and Faraday cup (F-Cup) shown. 31

Figure 3.6 Schematic for electronics used in PIG ion source ignition. . . 34

Figure 3.7 First PIG ion source design, with different parts labeled. . . . 35

Figure 3.8 Example picture of the overall setup, with the magnet, vacuum box, turbo pump, water cooling lines, and stand shown. 35

Figure 3.9 Glowing discharge along insulators shows primary area of HV breakdown. 36

Figure 3.10 Simulation of two axi-symmetric 6 mm radius electrodes separated by 4 mm. 37

Figure 3.11 Ion Source CAD design shown in V-Box. 38

Figure 3.12 Ion Source CAD design shown with hollow bracket and water cooling copper tubes used to cool the anode and cathode. . . . 38

Figure 3.13 2-D slice showing electric field strength in V/m. 39
Figure 3.14 Magnitude of electric field along 2-D slice of insulator, with anode in grey (15 kV) and puller in black (ground). 41
Figure 3.15 CAD models used for studying extraction of helium ions from PIG source using Charged Particle Tracing with space charge effects in COMSOL™. 42
Figure 3.16 Sweep of parameters of puller offet (a), puller outer chamfer (b), puller distance from anode (c), puller slit height (d), and puller slit width (e) with the resultant current for each particle on the puller. 44
Figure 3.17 Sweep of parameters of a) Anode chamfer angle and b) Anode chamfer offset with the resultant current for each particle on the puller. 45
Figure 3.18 Cross Section of ion source which shows the puller and anode plate. Both puller and anode plate have symmetric slants so that the electric field can offset the magnetic field curvature. . 46
Figure 3.19 E×B drift direction and logarithm of magnitude along the center of the magnet pole gap. 48
Figure 3.20 Outer and cross sectional view of the added electrodes used as an electron trap. 49
Figure 3.21 Charged particle tracing simulations of electron trapped in E×B electron trap and picture showing electron dumping locations. 50
Figure 3.22 CAD view of cathode design. 52
Figure 3.23 For a set power of 1 kW total, the average anode column temperature and total thermionic cathode current is shown as a function of the portion of power on the cathode. 54

Figure 4.1 Example Langmuir probe curve with a fit for the Maxwellian EEDF case (eq. 4.1). 58
Figure 4.2 Helium energy levels for LS designated states used in Yacora on the Web and the CR-model within this thesis. 66
Figure 4.3 Simplified flow chart for calculating the plasma parameters from an OES measurement when assuming a Maxwellian EEDF. 74

Figure 4.4 Ratio of intensities of 728 nm and 706 nm line for the (a) NSCR model and (b) Yacora on the Web. 76
Figure 4.5 Percent difference between the NSCR and Yacora model for the common intensity ratios: (a) I_{728}/I_{706} and (b) $_{667}/I_{728}$. . . . 77
Figure 4.6 I_{728}/I_{706} and I_{667}/I_{728} ratios with (a,b) and without (c,d) radiation trapping 78
Figure 4.7 Percent difference between the NSCR(n=4) and NSCR(n=10) model for the common intensity ratios: (a) I_{728}/I_{706} and (b) $_{667}/I_{728}$. 80
Figure 4.8 Mean percent difference between the NSCR n=4 and n=10 model along the T_e axis as a function of n_e for various n_g values. 81
Figure 4.9 Multiplicative factor that the I_{728}/I_{706} and I_{667}/I_{728} ratios are increased by (when compared to pure Maxwellian EEDF) for a bi-Maxwellian EEDF and Flat plus Maxwellian EEDF. . . . 83
Figure 4.10 Cross sections of TRIUMF-licensed Volume Cusp ion source. 86
Figure 4.11 Electron density and temperature as a function of position from TRIUMF filament ion source back plate as measured by the Langmuir probe. 88
Figure 4.12 a) Electron density and temperature and b) β for a Maxwellian + flat EEDF as measured by the Langmuir probe. 89
Figure 4.13 Simplified schematic of OES diagnostic setup for the TRIUMF ion source. 90
Figure 4.14 Example spectrum measurements (after relative calibration applied) from TRIUMF ion source with helium at 120 V, 2 A, and 18 sccm. 91
Figure 4.15 Measured and fit neutral gas density vs gas flow in TRIUMF-licensed volume cusp ion source 92
Figure 4.16 OES measurements without radiation trapping included, and Langmuir probe measurements. 94
Figure 4.17 Variations of electron temperature and electron density as a function of gas flow, arc current and arc voltage. 95
Figure 4.18 Variations of electron temperature and electron density as a function of gas flow, arc current and arc voltage. 97

Figure 4.19 Variations of β (proportion of electrons in colder Maxwellian EEDF) as function of gas flow, arc current, and arc voltage. . . 99
Figure 4.20 OES measurements using various OEFs within the NSCR code. Measurements are for a) electron density and b) electron temperature. 100
Figure 4.21 OES measurements using typical two ratios, additional I_{501}/I_{728}, I_{447}/I_{706}, and I_{492}/I_{728} ratios, and using these additional ratios combined with iterations to include radiation trapping from the metastable states. 102
Figure 4.22 Graphite cathode for cold cathode operation after use. 103
Figure 4.23 I_{arc} as a function of gas flow, V_{arc}, and magnet field strength in the high pressure low magnetic field regime. 104
Figure 4.24 I_{arc} as a function of gas flow, V_{arc}, and magnet field strength in the low pressure high magnetic field regime. 105
Figure 4.25 Simplified schematic of OES diagnostic setup for the Penning ion source. 106
Figure 4.26 Neutral gas density vs gas flow within the Penning ion source using MolFlow+ 107
Figure 4.27 n_e (black) and T_e (red) as a function of gas flow, V_{arc}, and magnet field strength in the high pressure low magnetic field regime. 108
Figure 4.28 n_e (black) and T_e (red) as a function of gas flow, V_{arc}, and magnet field strength in the low pressure high magnetic field regime. 109

Figure 5.1 Schematic for resistive drift waves. 114
Figure 5.2 Schematic of 1-D model in COMSOL™ 117
Figure 5.3 Ion and electron kinetic energy calculated from $\frac{1}{2}mv^2$, where v is calculated from the drift velocities, as a function of the potential energy gain in voltage along the source length for the 1-D model using only the standard drift-diffusion equation. . . 123
Figure 5.4 Ion and electron kinetic energy calculated from $\frac{1}{2}mv^2$, where v is calculated from the drift velocities, as a function of the potential energy gain in voltage along the source length. . . . 124

Figure 5.5 Charged particle densities and voltage as a function of distance from the cathode. 125
Figure 5.6 Electron temperature and ionization rate for He→He^+ and $He^+ \rightarrow \alpha$ as a function of distance from the cathode. 126
Figure 5.7 n_e and T_e as a function of gas flow, V_{arc}, and magnet field strength in the high pressure low magnetic field regime. 129
Figure 5.8 n_e and T_e as a function of gas flow, V_{arc}, and magnet field strength in the low pressure high magnetic field regime. 130
Figure 5.9 Calculated secondary emission coefficient at cathode boundary for 1-D model as function of gas flow at (a) high pressure and low magnetic field and (b) low pressure and high magnetic field. 131
Figure 5.10 Schematic of 2-D Charged-Particle Tracing model in COMSOL™ 133
Figure 5.11 Normalized ionization rates along the discharge length from the charged particle tracing simulation and the plasma 1-D model. 136
Figure 5.12 Mean electron energy from the CPT simulation and plasma 1-D model, along with the electric potential from the plasma 1-D model. 137
Figure 5.13 Normalized electron density from CPT simulation and plasma 1-D model, along with the electric potential from the plasma 1-D model. 138
Figure 5.14 Simple schematic of the 2-D axi-symmetric plasma model. . . 139
Figure 5.15 Example plots of a) electron density b) electron temperature and c) electric potential within the 2-D plasma model for parameter of 20 sccm, 1.5 kV, and 0.05 T. 142
Figure 5.16 Example plots of a) electron density b) electron temperature and c) electric potential within the 2-D plasma model for parameter of 4 sccm, 1.45 kV, and 0.4 T. 143
Figure 5.17 Average a) ion density, b) electron temperature, and c) electric potential as a function of radius for various cross field transport coefficients in the high pressure low magnetic field condition. 144

Figure 5.18 Average a) ion density, b) electron temperature, and c) electric potential as a function of radius for various cross field transport coefficients in the low pressure high magnetic field condition. 145
Figure 5.19 n_e and T_e as a function of gas flow, V_{arc}, and magnet field strength in the high pressure low magnetic field regime using the 2-D model. 147
Figure 5.20 n_e and T_e as a function of gas flow, V_{arc}, and magnet field strength in the low pressure high magnetic field regime using the 2-D model. 149
Figure 5.21 α density as a function of gas flow, V_{arc}, and magnet field strength in the low pressure high magnetic field regime using the 2-D and 1-D model. 151

Figure 6.1 Schematic of the Ion Source and the F-Cup setup. The beam comes out from the puller and rotates. 153
Figure 6.2 Example of simulated and measured F-Cup current. 155
Figure 6.3 Total current from bias power supply (red) and discharge arc current (blue) as a function of extraction voltage between puller electrode and anode. 157
Figure 6.4 Variations of He^+ and beam dump current are shown as a function of variations in gas flow, arc voltage and magnetic field at V_{ext} = 2.5 kV. 158
Figure 6.5 Variations of α current (red) and puller current (blue) are shown as a function of variations in gas flow, arc voltage and magnetic field at V_{ext} = 2.5 kV. 159

List of Abbreviations

AC Alternating Current

CAD Computer-aided Design

CCD Charged-coupled device

CCPS Capacitor Charging Power Supply

CPT Charged Particle Tracing

CPU Central Processing Unit

CR Collisional-Radiative Model

DAQ Data Acquisition

DC Direct Current

ECR Electron Cyclotron Resonance

EEDF Electron Energy Distribution Function

E×B Cross Product of Electric and Magnetic Fields

F-Cup Faraday Cup

HV High Voltage

ID Inner Diameter

ISTF Ion Source Test Facility

MACOR™ Machinable glass-ceramic from Corning Inc.

MC Monte-Carlo

MCC Monte-Carlo Collision

ND Neutral Density

NSCR Nicolas Savard Collisional-Radiative

OD Outer Diameter

OEF Optical Escape Factor

OES Optical Emission Spectroscopy

PDE Partial-Differential Equation

PIC Particle-in-cell

PID Proportional-integral-derivative

PIG Penning Ion Gauge

PLC Programmable Logic Controller

PS Power Supply

PTFE Polytetrafluoroethylene

TRIUMF TRI-University Meson Facility

UV Ultra-violet

V-Box Vacuum Box

List of Programs

COMSOL Multiphysics™ Commercially available general purpose simulation software. This software uses advanced numerical methods for solving various physical models, and is capable of modeling several different physics at once (hence Multiphysics) in addition to single-physics.

LabVIEW Laboratory Virtual Instrument Engineering Workbench: a visual programming language from National Instruments used in system controls.

Molflow+ Computer program allowing for calculating steady-state pressure in complex geometries. Used under conditions of molecular flow, when the mean free path of molecules is larger than the geometry in use. Particles are simulated using Monte-Carlo simulations. Written in ESRF (Grenoble, France) and improved and maintained at CERN.

OnShape™ Browser based CAD modeling software.

Python Open-source and free general purpose programming language.

Yacora on the Web Web application which allows access to collisional radiative models based on the Yacora solver. It currently has general models for plasmas based on the hydrogen atom, hydrogen molecule, and helium atom. It is produced and maintained by IPP Garching (Max-Planck-Institut fur Plasmaphysik).

Acknowledgments

This project was started by D-Pace Inc, and so many thanks to Morgan Dehnel for giving me the opportunity to do this project, and for always providing support, guidance, and much needed optimism when I needed it. Thanks to Dave Potkins and Stephane Melanson for all the invaluable advice given during this project, y'all are the backbone of this project and none of it could have been done without your help. Thanks to Joe Theroux for all your work designing so much of the Penning ion source system and for all the additional technical advice. Thanks to Anand George for all your support at the ISTF and for making the ISTF a less isolating place to work at.

Much of the project was done at Buckley Systems, where there's a huge list of people who helped out. Thanks to Tobin Jones for being the most resourceful encyclopedia in Auckland, which led me to bugging you whenever I had any technical or physics-related question. I appreciate you helping me out without hesitation every time. Same goes to Hamish MacDonald and Chris Philpott, who also helped me with any questions without hesitation. I'd like to thank Paul Williams for also being an invaluable resource and an invaluable friend to a random guy who came in from across the Pacific. Others who have helped me in many ways: Alexey Groutso, Wendy Liu, Steve Brown, Jon Avery, Mark Dyer, Ryan Parker, and frankly so many others that would help out with hands-on work. An entire of list Buckley's employees who've helped me would take over this entire thesis.

I would like to thank my academic supervisor Reiner Kruecken from TRIUMF for his guidance during this project. I, as well as all of D-Pace, appreciate all the help you've given so that I may become an eventual PhD graduate, especially given the enormous amount of responsibilities already on your plate. I would like

to thank the Accelerator Division of TRIUMF, especially Oliver Kester and Aurelia Laxdal, for allowing me access to COMSOL™ which as the reader will see is an essential part of this thesis. I would also like to thank Fernando Maldonado at TRIUMF for being my occasional guru when I needed help with this software.

I would like to thank the supervisory committee Janis McKenna, Jeremy Heyl, and Thomas Mattison for keeping me on track with what I need to do going forward after each of our meetings. Without your inputs I would have been chasing dumb ideas for years that would never have led to a possible PhD thesis.

I'd like to thank Olli Tarvainen for all the discussions we've had, I'm glad you indulged me with a few chats whenever you could to talk about ion source physics. I'd also like to thank Gwenael Fubiani, who I worked with at the very end of my PhD. It was nice to finally have someone I could regularly talk plasma physics with, and even though we met late during my project, the discussions we had were still incredibly valuable. Thank you to Dirk Wunderlich for the email exchanges when I was comparing my CR-model to the Yacora on the Web model. This was very helpful in validating my program.

Thanks to UBC along with D-Pace Inc for financially supporting me throughout this project. In a sense this is the most important thanks I can give, since without them I wouldn't be able to eat or have any hobbies!

And of course, one cannot write acknowledgments without thanking your loved ones. As far as I understand it, we are basically just a product of genetics and our environment, which means that my parents, Carole and Guy, are the primary reason for anything I do. This means of course that the creation of this thesis is in large part thanks to them! And thanks to my siblings Claire, Lea, and Emile. I'm not willing to give y'all any credit for any of this thesis, but since I love you all so much, you make the cut. That's just good ole nepotism for ya.

Dedication

The entire purpose of this thesis is to contribute information to those in the scientific community doing similar work, that way they won't have to go through as many of the obstacles I did. This thesis is dedicated to those in the community who have done the same by diminishing the obstacles I, and others like me, would have had to face without their work.

Chapter 1

Introduction

1.1 Accelerators for Medicine

Accelerators are machines that take charged particles and accelerate them to high energies using electromagnetic fields. There are four primary uses for particle accelerators: discovery science, medicine, industry, and security [3]. Discovery science is using particle accelerators to create interactions that can be measured to provide evidence for or against different theoretical models. Industry uses particle accelerators for semiconductor chip manufacturing, surface hardening, and the general modification of material properties for commercial products. Security needs particle accelerators for cargo inspection and material characterization.

Medicine generally uses particle accelerators for either direct therapy or to produce radioisotopes for medical diagnosis and radiotherapy. Some radioisotopes that are produced will be directly introduced to the body by attaching it to a biological molecule that collects near a tumor [4]. The radioisotope will usually radiate gamma or beta rays, which then destroys the targeted tumor in the body.

A relatively new field is alpha radioimmunotherapy. This uses radioisotopes that emit alpha particles. Due to the higher amount of deposited power by alpha particles in tissues, the effective range of irradiated tissue is much smaller than other radiation types, resulting in localized energy deposition on the targeted tumor.

An example of such a radioisotope under recent study is ^{211}At [5], which is appealing due to its 7.2 hour half-life, which allows time for necessary pre-injection

procedures. An additional benefit is that one of the forms of decay (other than direct alpha decay) includes the emission of 77-92 keV X-rays, which can be used to track the radioisotope inside the body via medical imaging techniques.

1.1.1 α Production

The reaction which produces ^{211}At is $^{209}\text{Bi} + \alpha \rightarrow 2\text{n} + {}^{211}\text{At}$, where the α particle has to be about 28 - 29.5 MeV. This reaction is usually undergone in cyclotrons which accelerate the α particles to these energies, and then bombard them against the bismuth foil. The source of these α-particles are the aptly named *ion source*, which is what generates the ions within an accelerator. The cyclotrons which typically create these particles usually have Electron Resonance Cyclotron (ECR) Ion Sources [6] to do this. These ion sources use strong magnetic fields which confine electrons inside the source. The electrons are accelerated to high energies using microwaves at the electron cyclotron frequency corresponding to the internal magnetic field strength. These energetic electrons then deposit their energy through ionization of a background gas. The combination of higher particle confinement and power deposition leads to the production of high-charge state ions. This allows one to then extract relatively large currents of these high-charged-states, up to $^{16}\text{O}^{7+}$ for example [6].

However, for many medical cyclotrons in use, these large and expensive ECR sources are only used to produce α particles, which is excessive since α particles are only a 2+ state [7]. Consequently, these cyclotron manufacturers are looking for ways to get high current α-particle beams using less expensive and more compact ion sources.

1.2 Penning Ion Source

There is an old type of ion source which is much simpler and lower cost than ECR sources, and has been regularly used for producing high-charge state ions. This is called the Penning ion source, sometimes shortened to PIG (Penning Ion Gauge) source. These sources have been in use since the 1940s [8], and were first used as ion sources in the center of cyclotrons due to the small space and strong magnetic field there. The workings of a Penning ion source are shown in figure 1.1. This is a

simplified example of a PIG source with the cross section along its center. The anode is cylindrical and has two cathodes on either end which are biased about 0.1 - 2 kV below the anode. A charged particle will orbit about magnetic field lines within a radius proportional to the magnetic field strength and inversely proportional to the particle mass. Due to the small mass of the electrons, a strong magnetic field (> 0.1 T) along the anode will prevent an electron from moving towards the anode. In addition, the cathode-anode configuration will create electric fields which push electrons toward the center of the source, therefore also trapping electrons along this axis. These trapped electrons reach energies up to the electric potential between the anode and cathode, and then oscillate between the cathodes until they deposit part of their energy through ionization of the background gas, creating a collection of electrons and ions called a plasma. Those ions near a slit in the anode will then feel the pull of the puller electrode, causing them to be extracted out through the puller slit into an accelerator system.

Due to the high degree of confinement, these ion sources have been used for producing high-charge states of several heavy ions [9–14]. Although it is rarely found in literature, there are some examples of accelerator engineers and scientists who have made PIG sources specifically for the production of α-particles by using helium gas. In these cases, estimated beam currents for α-particles of up to 350 μA[15] have been achieved in standard ion sources, and up to an estimated 1 mA[16] when introducing mechanical movements to artificially create a small plasma column.

There are numerous articles from the 1930s to the early 1970s that discuss the Penning ion sources used in cyclotrons for heavy-particle high-charge state ion production. Much is known about the engineering behind Penning ion sources in these conditions. This includes various types of operations types such as cold cathode, self-heated cathode, filament, and indirectly heated cathodes [8, 10]. This information includes types of materials used, various designs, various gas species used for operation (including metal vapors), and different extraction types. However, these articles generally discuss engineering solutions based on certain constraints for whichever cyclotron they're built for, and rarely study the plasma dynamics within. Researchers that did attempt to make measurements of the internal plasma properties often used general power-balance estimates which are imprecise rather

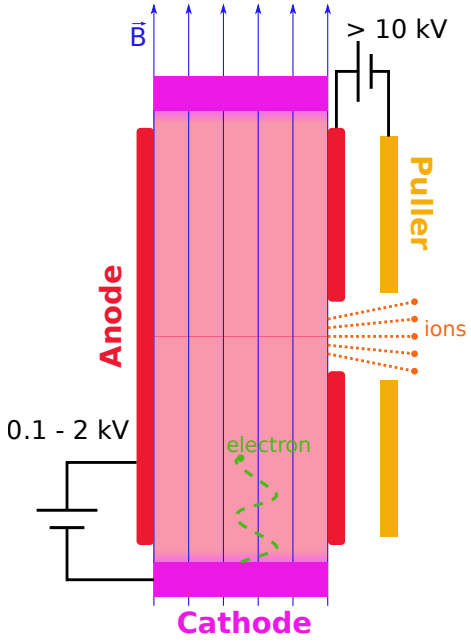

Figure 1.1: Simplified schematic of a Penning ion source. Composed of a cylindrical anode (red), cathode (purple), and puller (dark orange). A uniform magnetic field along the anode (blue arrows) allows confinement of electrons (green) perpendicular to this field. The potential from the cathodes (light purple-red) allows for confinement of electrons along the magnetic field. Ions are then pulled out due to the electric field between the puller and anode.

than modern standards for plasma measurements [17].

In addition, it is even rarer to find any articles on the use of Penning ion sources for α particle production. The few that can be found [15, 16] were designed in cyclotrons with geometric constraints and set magnetic fields. Furthermore, many references within the articles from conferences, internal reports, and PhD theses are not readily accessible online since many of these studies were done before the 1960s. Therefore, unless they were published within a major journal at the time, they cannot be easily accessed. This means that there is significant information about high-charge state producing Penning ion sources that is not widely available.

This includes how to optimize a Penning ion source in terms of various plasma chamber geometries and magnetic field strengths for α particle production. There are also few studies which include measurements of the plasma properties within the ion source. Hence a literature review leaves one with little understanding of how the plasma dynamics within the ion source, which varies according to what parameters it operates at, changes α particle production. This lack of information might prevent researchers from finding better engineering solutions which take advantage of the internal mechanisms within the plasma that increase α production. However, despite these limitations, it has been shown clearly that high charge states can be produced within these ion sources. For example, Ar^{5+} could be produced with up to 27.1% of the total beam current from such an ion source with about 25 mA maximum output [12]. Since the ionization from Ar^{4+} to Ar^{5+} at 74.84 eV is higher than the ionization energy of He^{+}, it is feasible that such a source could be used to generate high currents of α particles. The need for these less-costly ion sources is also quite timely, since the use of α particles for producing ^{211}At and PET (Positron emission tomography) radioisotopes like ^{43}Sc [18] has gained recent popularity.

1.3 Purpose of PIG development

The ability to produce high-charge states make the PIG source a potential candidate to replace ECR sources in α-producing medical cyclotrons, as they can still produce high-intensity beams with simpler engineering and a more compact size. This would severely reduce the cost of α-particle production in these accelerators, and as a result would reduce the cost of producing radioisotopes for cancer therapies. This has consequentially sparked interest in the viability of these sources by a company called D-Pace Inc [19], a particle accelerator engineering company which designs and sells commercial ion sources. They would like to design a commercially available α-producing PIG source which could eventually become a cost-effective replacement for ECR sources within medical accelerators. In order to replace ECR sources, these would have to produce α-particle beams of about 1 mA at 30 keV ion beam energy, be able to last under continual operation for approximately 100 hours, and have a normalized emittance (essentially the angle $\times$

geometrical size of the beam) of 1 mm-rad.

However, as mentioned in the previous section, a review of the scientific literature reveals that studies on PIG ion sources focus much more on engineering. Studies of the internal plasma processes in these plasmas are rare and these processes are therefore not well understood. In addition, these ion sources have often been developed with conditional constraints, for example the value of the magnetic field and geometrical space in a cyclotron. A stand-alone commercial source would be free from such constraints as it would be situated outside the machine. This means that a source could be optimized to create a maximal current of α-particles by varying what would normally be kept constant.

It is for these reasons that it is important to create a PIG source test stand which can have variable input parameters, allowing one to study how the ion source's beam currents change as a function of these parameters. These measurements could then be used to find the optimal design of a PIG source which can maximize the production of α-particles, leading to a design of a PIG source which can compete with the ECR source.

It's also important to know what causes an increase or decrease of α-particle production as these parameters change, which means an understanding of how the plasma itself varies and why these variations effect α-particle production. These insights into the actual physics of the plasma are key components to higher-performance ion source designs in the future. As a result, this test stand should be able to measure key properties of the helium plasma as well via plasma diagnostics. This can then be compared to physical models which describe the plasma dynamics.

This thesis describes the efforts of designing, assembling, and characterizing a PIG source using helium gas for α-particle production as a stepping stone for future commercialization. This thesis will cover the design and assembly of the ion source, the study of the helium plasma physics within the operational parameters of the ion source, the development of a diagnostic for measurements of the primary plasma properties, and observations of the ion beam extraction from the ion source.

The novelty in this thesis thus comes primarily from the measurements of the plasma parameters within the Penning ion source as a function of the various input operational parameters, and relating these to extracted beam currents. In this case, the plasma properties will be diagnosed using optical emission spectroscopy which

are being compared to predictions by a collisional-radiative model developed for this thesis. Based on a review of the pertinent literature, such measurements have not been done in the past, and could provide valuable information as to what causes high production of certain charge states (specifically for α-particle production). This thesis also presents models of the Penning ion source using relatively simple (when compared to state-of-the art Particle-in-Cell codes) drift-diffusion codes in order to determine whether such codes can be used to explain the plasma variations observed by plasma diagnostics. In addition, the test stand design for the Penning ion source will allow us to observe the effects of different magnetic fields on the Penning ion source. Variations of magnetic field and their affects on the plasma and beam output is rarely characterized, since Penning ion sources are generally used within cyclotrons with constant magnetic field. Finally, since this test stand is an original design, the reader will find novel engineering solutions to technical issues within this thesis, which could be beneficial to other ion source physicist-s/engineers with similar issues.

Chapter 2

Theoretical Concepts

2.1 Plasma Defined

Before one can understand the workings of a Penning ion source, one must first understand the nature of matter within this object: a plasma. A plasma is often described as the fourth state of matter. Starting from a solid, an increase in temperature in the system leads to a weakening of inter-molecular bonds turning it into a liquid. A further temperature increase will break the bonds which keeps the liquid together, leading to the formation of a gas. A gas typically has negligible interactions between particles, and therefore the final bond to be broken are the internal atomic bonds between electrons and the nucleus. The process of removing electrons from atoms/molecules is called *ionization*, and is the process by which plasmas are formed. This fourth state of matter is then reached when there is enough energy to keep some significant portion of the atoms/molecules ionized as positively charged ions and negatively charged electrons (or negative ions).

2.2 Atomic Structure

To understand how plasmas are formed, it is useful to conceptualize the structure of an atom. It is assumed that the reader is familiar with the classical description of the atom, in which a nucleus composed of protons and neutrons is surrounded by orbiting electrons. An accurate representation of the atom requires quantum

mechanics, which confines the state of an 'orbiting' electron by four quantum numbers: n (principal quantum number), l (orbital angular momentum number), m_l (orbital magnetic quantum number), and m_s (spin magnetic quantum number) [20]. The later numbers are essentially the projection of the angular momentum and spin along a particular direction. n and l are integers, and the restrictions for all quantum numbers are $l+1 \leq n$, $|m_l| \leq l$, and $m_s = \pm\frac{1}{2}$.

The Pauli exclusion principle says that a state defined by some unique combination of these quantum numbers can only be occupied by a single electron. Stable ground state atoms are usually formed by placing electrons into increasing energy states (starting with the lowest energy state) until the number of electrons is equal to the number of protons in the nucleus. The valence electrons are the least bounded electrons found on the outermost 'shell' (usually highest n and l). An *excitation* of an atom usually corresponds to one of these valence electrons being raised to a higher energy state through energy exchange with a colliding particle. The ionization of an atom corresponds to the valence electron being completely removed (unbounded) from the atom through energy exchange with a colliding particle.

2.2.1 Helium Structure

For helium and other light elements, the different electron configurations are often specified by total orbital quantum number and spin for all the valence electrons. This is to characterize the total coupling between electrons due to spin-orbit interactions. These are given by $L = \sum l_i$ and $S = \sum s_i$. The total orbital quantum number is given by an integer L = 0, 1, 2, 3, 4, 5, etc, which are known as S, P, D, F, G, and H levels respectively. The total angular momentum number is then defined by $J = L + S$. The multiplicity of a term is defined by the possible values of J, which is $2S+1$ for L > S.

The way each term is defined in helium is by the $n^{2S+1}L$ notation. For example, in helium the electron configuration for n = 4, S = 1 and L = 1 is the 4^3P term. This term then can be further specified by sublevel with a total angular momentum. The amount of these sublevels is the multiplicity of the term. So in the case of the 4^3P term, we have L = 1 and S = 1, 0, -1 along a projected axis, so the total angular momentum can be J = 2,1, or 0. If we want to specify the total angular momentum

number, this is in form $n^{2S+1}L_J$. As an additional example, for n = 2, S = 1, L = 1, and J = 2 we specify as the 4^3P_2 term.

There is further splitting of microstates for each J due to the different projection of J onto a particular axis (J_z) which is $2J+1$. So for each term with particular L and S, there are a total of $(2S+1)(2L+1)$ microstates which is the *statistical weight* g. It is generally convenient to group all the terms by numbers n, L, and S since the microstates have negligible differences in energy. As a result, they are considered degenerate states in energy.

2.2.2 Spontaneous Emission

Excited states have some probability per unit time to undergo spontaneous emission, which is the emission of a photon by transitioning to a lower excited or ground state. For LS coupling (such as in helium), there are a few selection rules for allowed dipole radiation when undergoing spontaneous emission. These are when $\Delta S = 0$ and $\Delta L = 0, \pm 1$, with the exception of transitions with $L = 0 \rightarrow L = 0$. Other radiative transitions that do not follow these rules are called 'forbidden'. This is a misnomer as they do exist, but they are simply much less probable than the allowed dipole transitions.

There are some excited states which have only 'forbidden' radiative transitions to lower energy states. These excited states that do not have high probabilities of radiative transitions are called metastable states. In a plasma, these states generally transition to lower energies via collisions. These can be collisions with other particles or with the plasma chamber wall.

The spontaneous transition probability for a radiative transition from state i to k is symbolized by A_{ik} (also known as the Einstein Coefficient) given in units of s^{-1}. This transition produces a photon with energy (and therefore specific frequency and wavelength) corresponding to the difference between the two energy levels. The radiated power for a certain radiative emission (sometimes called a spectral line) is [20]:

$$\varepsilon_{line} = \frac{1}{4\pi} h \nu_{ki} A_{ki} n_k \tag{2.1}$$

where the subscripts k and i refer to the upper and lower state respectively, n_k is the

density of the upper state, and ν_{ki} the frequency of the radiated photon. This gives the radiated power for a particular spectral line per unit volume and solid angle.

2.3 Electron Impact Collisions

The dominant source of collisions in weakly ionized plasmas are electron impact collisions. These are collisions between electrons and the neutral gas particles in the volume of the plasma chamber. These collisions generally involve elastic and inelastic collisions. An elastic collision is when the two particles do not have any change in their internal energies, and therefore the total kinetic energy of the system stays the same. In an inelastic collision, the total kinetic energy of the colliding particles is not conserved, because some of the energy goes into the internal energy of one of the particles. For an electron interacting with a neutral gas particle, this is the result of either excitation or ionization of the neutral particle. An electron can also gain energy from the collision due to a de-excitation of an excited neutral particle, which causes the upper level electron to go to a lower state with the transition energy going to the colliding electron.

2.3.1 Cross Sections and Rate Coefficients

The cross section, usually symbolized as σ, is used to describe the likelihood of a reaction for a particle and is usually a function of the difference in velocity between the two particles. A common way to visualize the cross section is to imagine a volumetric slab filled with neutral particles of number density n_g, which we assume to be stationary with respect to the electrons. Let us also assume there is a flux of electrons with density n_e that enters this slab with some velocity v_e. In this case the amount of electrons that interact ($n_{collision}$) within some length of the slab x along the direction of the electrons is:

$$n_{collision} = \sigma n_e n_g x \tag{2.2}$$

So the amount of interacting electrons is proportional to the density of electrons, the density of gas particles, the distance the electrons traverse the background gas, and the cross section. So the cross section is the area perpendicular

to the electrons velocity which corresponds to an interaction with the background gas. If we differentiate 2.2 with respect to time, we then get the volumetric reaction rate.

$$R_V = n_g n_e < \sigma(v_e) v_e >= n_g n_e K = n_g \nu \tag{2.3}$$

In this equation we also define the rate constant $K =< \sigma(v_e) v_e >$ and the collision frequency ν, which will be important parameters when studying volume processes in plasmas.

2.3.2 Elastic Collisions

In elastic collisions, all energy transfer is through the kinetic energy of the initial particles. The average fraction of kinetic energy transfer from mass m to a particle of mass M is [21, 22]:

$$\gamma = \frac{2mM}{(m+M)^2} \tag{2.4}$$

In the case of electrons on atomic particles, the electron mass is order of magnitudes smaller, resulting in a very small transfer fraction for each elastic interaction between fast electrons and slow neutrals. Plasmas are generally powered by giving energy to the electrons and then having them deposit this energy in a background neutral gas. It's because of this small energy transfer in elastic collisions that the electron temperature will generally be higher than the background gas temperature (and ion temperature) in most laboratory gas discharges. Between heavy particles though, the fraction of kinetic energy lost is much higher, which leads to them reaching an equilibrium temperature among themselves.

2.3.3 Coulomb Collisions

Electrons can also undergo elastic collisions with ions in the plasma via Coulomb collisions, which is scattering due to the Coulomb force between two charged particles. The cross section is normally defined for scattering of the particle by large angle (greater than 90°). Since the Coulomb force is long range, the dominant source of large angle scattering is due to the sum of many small-angle collisions.

The net scattering cross section of an electron on an ion is [22]:

$$\sigma_{ei} = \frac{8}{\pi} b_0^2 ln\Lambda \tag{2.5}$$

where we define Λ and b_0 as:

$$b_0 = \frac{q_1 q_2}{4\pi\varepsilon_0 E_{CM}} \tag{2.6}$$

$$\Lambda = \frac{2\lambda_{De}}{b_0} \tag{2.7}$$

with q_1 and q_2 being the charges of the particles, E_{CM} being the center of mass energy (usually approximated as the electron energy in plasmas due to much higher energy), and λ_{De} the electron debye length (see section 2.5.1).

2.4 Charged Particle Losses

After a plasma has been formed, electrons and ions formed via electron impact ionization can then be lost in two primary ways: ion-electron recombination and charged particle diffusion to the chamber walls.

2.4.1 Electron-Ion Recombination

Electrons and ions will recombine if two conditions are met: they are sufficiently low in velocity, and the population density is high enough so that the average distance between them is small, therefore allowing the particles to get trapped by each other's Coulomb potential [21].

The three-body recombination is described by e + e + $A^+ \rightarrow$ A* + e and is most important in atomic plasmas, where A represents the atom. The second electron in the collision is required for momentum conservation. The asterisk symbolizes an excited state of particle A. Radiative recombination is described by e + $A^+ \rightarrow$ A + photon. The cross section for this is typically smaller than three-body recombination because it requires radiative emission in the time-scale of an electron-ion interaction. This process is dominant over three-body recombination at low electron densities.

2.4.2 Wall Neutralization

Typically, ion sources have conducting metallic walls which allow charged particles to be dumped. Positive ions which reach this wall will be neutralized by the electrons in the conducting wall. Electrons meanwhile will simply be absorbed in the wall upon collision. This is usually the primary source of charged particle loss in low pressure ion sources, due to the fairly high arc currents, and relatively low electron densities.

2.5 Plasma Physics

Plasma Temperature

Temperature is an important property of a plasma, as it is proportional to the mean kinetic energy of the particles, which affects how much energy is available for ionization. A gas at thermal equilibrium will tend towards an isotropic Maxwellian distribution, which refers to a standard Maxwell-Boltzmann distribution, which is described by [23]:

$$f(v) = \left(\frac{m}{2\pi k_B T}\right)^{1/2} e^{-\frac{mv^2}{2k_B T}} \ , \ \int_{-\infty}^{\infty} f(v)dv = 1 \tag{2.8}$$

where v is the particle velocity, m the particle mass, k_B the Boltzmann constant, and T the temperature in Kelvin. In plasma physics, it is typical to cite temperature in eV rather than Kelvin, which corresponds to 1.6×10^{-19} J, or the energy gain of a particle of elementary charge e across a 1 V gap. It is sometimes more useful to use the relation $v = \sqrt{\frac{2E}{m}}$, for non-relativistic particles of kinetic energy E and mass m, to present the distribution as a function of energy:

$$f(E) = 2\sqrt{\frac{E}{\pi}}\left(\frac{1}{T}\right)^{3/2} \exp(\frac{-E}{T}) \tag{2.9}$$

where T is the particle temperature in eV. This is an example of an electron energy distribution function (EEDF), which describes the portion of particles within

some infinitesimally small energy range dE. This requires:

$$\int_0^\infty f(E)dE = 1 \tag{2.10}$$

However, the temperature of a plasma often isn't uniform among all particles. This is especially true within ion sources, as the gas pressure is often so low ($<$ 50 mTorr) that electrons can reach thermal equilibrium among themselves, but not with the heavier neutral gas particles and ions before diffusing to the walls. This is because electrons have negligible mass compared to these heavy particles, which from equation 2.4 results in minimal energy transfer between them.

As a result, different species will have different temperatures between the neutral gas, ions, and electrons. These are T_g, T_i, and T_e respectively. T_e is typically much higher than T_g and T_i as it is the primary absorber of the electrical power used in ion sources.

Even among certain indistinguishable particles, such as electrons, there might even be different temperatures along different axes in a coordinate frame. This can happen due to the existence of magnetic fields. The forces on charged particles perpendicular to the magnetic field may be different than those along it depending on which direction the force goes. This can then produce uneven heating of particles in these directions.

2.5.1 Fluid Model

A common way to model the complex many-body dynamics of a plasma is to simplify the equation of a charged particle within it to a collection of charged particles within some volume, called a fluid element. In order to get the basis of the fluid equation of motion for a charged particle fluid in electromagnetic fields, we start with the single charged particle Lorentz equation and multiply by the local density n of this particle [23]:

$$mn\frac{d\vec{v}}{dt} = nq(\vec{E} + \vec{v} \times \vec{B}) \tag{2.11}$$

where q is the charge of the particle, $\vec{E}$ and $\vec{B}$ the electric and magnetic field. If we change the variable to a fluid element velocity $\vec{u}$ and expand the derivative on the

left-hand side, then we get:

$$mn\left(\frac{\partial \vec{u}}{\partial t} + (\vec{u}\cdot\vec{\nabla})\cdot\vec{u}\right) = qn(\vec{E} + \vec{u}\times\vec{B}) \tag{2.12}$$

This describes how a fluid of charged particles with average velocity $\vec{u}$ moves in applied electromagnetic fields. Within a fluid element, the change in the fluid velocity will also come from the exchange of its particles with other particles in other fluid elements. This is the pressure force, where the pressure of a gas at some point in space is $p = nk_BT$, and the pressure force per unit volume is then $-\nabla\cdot p$ which is added to the right side of eq 2.12. Plasma physicists usually assume a Maxwellian distribution that is isotropic. For non-isotropic velocity distributions with different temperatures along each spatial axis, this pressure term becomes a tensor.

So we have changes in fluid element velocities due to external fields and due to the pressure force. However, in a plasma there are usually several types of particles. So we also need a collisional factor which accounts for the change of particle velocity due to collisions with other particles. These particles are typically background neutral particles in weakly ionized plasmas. In the fluid equation, we are looking at momentum loss, which is proportional to the difference in velocity $(\vec{u} - \vec{u_0})$ where $\vec{u_0}$ is the neutral velocity, and also proportional to ν_{en} which is the electron-neutral collision frequency. In this case we refer to the charged particles as electrons, but for ions the collision frequency would be ν_{in}. Adding this term as well to 2.12 we get:

$$mn\left(\frac{\partial \vec{u}}{\partial t} + (\vec{u}\cdot\vec{\nabla})\cdot\vec{u}\right) = qn(\vec{E} + \vec{u}\times\vec{B}) - \nabla\cdot p + mn\nu_{en}(\vec{u} - \vec{u}_0) \tag{2.13}$$

We have the frequency term $\nu_{en} = n_n\sigma(v)v$, where n_n is the neutral particle density, σ the cross section for momentum loss of the charged particle on a neutral particle (typically dominated by elastic collisions), and v the charged particle velocity. As we assume a Maxwellian velocity distribution, we average the reaction

rate $\sigma(v)v$ over the entire distribution. As a result, one generally uses:

$$\nu_{en} = n_n \langle \sigma v \rangle \tag{2.14}$$

Drift-Diffusion Model

Equation 2.13 is often further simplified in order to avoid the non-linear dependence on $\vec{u}$. First we assume a steady-state where $\frac{\partial \vec{u}}{\partial t} = 0$. We then assume that the fluid is dominated by collisions, so that $\left((\vec{u} \cdot \vec{\nabla}) \cdot \vec{u}\right) << \nu \vec{u}$, consequentially causing the total time derivative $\frac{d\vec{u}}{dt}$ term vanish on the left side of the equation. In the absence of magnetic field, we then get the following equations:

$$\Gamma = n\vec{u} = \pm \mu n \vec{E} - D\nabla n \tag{2.15}$$

The $\pm$ is used for either negative or positively charged particles, as it determines which direction they drift along the electric field. Γ is the particle flux, μ the mobility, and D the diffusion coefficient. The latter two are defined by:

$$\mu = \frac{e}{m\nu} \tag{2.16}$$

$$D = \frac{k_B T}{m\nu} \tag{2.17}$$

These are related by the Einstein relation:

$$\mu = \frac{eD}{k_B T} \tag{2.18}$$

This is called the drift-diffusion model, and is often used to model steady-state plasmas.

Boltzmann relation and the Debye length

For the case of electrons, where we assume equation 2.15 to be 0 due to their low mass and therefore can reach steady states in small time scales, we can then also set $\vec{E} = -\nabla V$ and solve for the Boltzmann relation assuming the minimum potential

is at V = 0 [22, 23]:

$$n_e = n_0 e^{\frac{eV}{k_B T_e}} \tag{2.19}$$

with n_0 the number density where V = 0. This essentially states that the electron density at a certain potential is reduced for higher temperatures due to the increased ability of some electrons to escape the potential well. On the other hand, the electron density will increase with increasing electric potential, thus electrons will collect around any positive potential until their attraction is equal to the opposing pressure force. Notice ion velocities are ignored, as they are much less mobile than electrons due to their heavier mass.

Using this relation and Poisson's electrostatic equation, we can estimate the scale of this electrostatic shielding effect within a plasma as a function of the electron density and temperature. This is called the Debye length [21–23]:

$$\lambda_D = \left(\frac{\varepsilon_0 k_B T}{n e^2} \right)^{1/2} \tag{2.20}$$

where ε_0 is the vacuum permittivity. This is an essential parameter which determines whether plasma physics applies to some spatial region. If we have a space on the order of some scale $L >> \lambda_D$, then any local potentials which come about, usually by some increase/decrease in charged particle concentrations, will be shielded and leave most of the space free of large electric fields. This maintains a fundamental condition of 'quasi-neutrality' in a plasma. This condition is that $n_e \approx n_i$, which is necessary for a steady-state plasma to be contained within some volume.

2.5.2 Plasma Confinement with Magnetic Fields

The use of magnetic fields to contain charge particles within a plasma is used in all fields of plasma physics; including ion sources, thermonuclear fusion, ion thrusters, and light sources. This is because charged particles are confined to a helical path, with radius called the gyroradius, along the magnetic field lines. The gyroradius is:

$$r_g = \frac{m}{q} \frac{v_\perp}{B} \tag{2.21}$$

where $\frac{m}{q}$ is the particle mass to charge ratio, and $v_\perp$ its speed perpendicular to the magnetic field B. Thus the higher the magnetic field strength, the more confined a charged particle is moving perpendicularly to this field.

Using equation 2.13, with the steady state assumption $\frac{du}{dt} = 0$ and getting rid of the $\left((\vec{u}\cdot\vec{\nabla})\cdot\vec{u}\right)$ term, one can solve for the mobility and diffusion coefficients perpendicular to the magnetic field. Along the magnetic field, only equation 2.15 applies. The equation for the drift perpendicular (denoted by symbol $\perp$) to the magnetic field is:

$$\Gamma_\perp = n\vec{u_\perp} = \pm\mu_\perp n\vec{E} - D_\perp \nabla n + n\frac{v_E + v_D}{1+(\nu/\omega_c)^2} \tag{2.22}$$

where $\omega_c = \frac{qB}{m}$ is the cyclotron frequency for the charged particle with charge q, which is the angular frequency that it rotates about the magnetic field lines. v_E and v_D are drift velocities which come from the general $\vec{F}\times\vec{B}$ drift velocities, where $\vec{F}$ relates to either the force from the electrical field or from the pressure force. These will be neglected in this thesis, as it does not lead to a net drift to the chamber walls in a Penning ion source. The perpendicular diffusion coefficient and mobility are:

$$\mu_\perp = \frac{\mu}{1+(\omega_c/\nu)^2} \tag{2.23}$$

$$D_\perp = \frac{D}{1+(\omega_c/\nu)^2} \tag{2.24}$$

We see from equations 2.24 and 2.23 that when $\omega_c >> \nu$, the mobility and diffusion coefficient become proportional to $\frac{1}{B^2}$, which severely retards the movement of charged particles perpendicular to the magnetic field. This is the reason why strong magnetic fields are preferred for charged particle containment.

2.6 DC Discharges

The Penning ion source is an example of a DC discharge, which is essentially a steady-state plasma sustained by a cathode (negative voltage terminal) and an anode (positive voltage terminal) at a constant arc voltage and arc current. The arc voltage and arc current is simply those parameters defined across the cathode and

anode.

2.6.1 Collisionless Sheath

A plasma is usually contained within a chamber with metal walls which acts as a loss mechanism for charged particles. We've seen from the notion of the debye length that potentials in a plasma tend to be shielded, keeping the bulk plasma quasi-neutral. This effect is what causes a sharp drop in electric potential towards the chamber walls, called the *plasma sheath*.

The reason for this is as follows: let us assume a quasi-neutral plasma $n_i \approx n_e$ within a metal chamber, with no magnetic fields. Due to their low mass, electrons near the wall will escape much faster than the ions. This leaves behind a concentration of positive charge and therefore an electric field within the plasma pointing towards the wall. This field retards the electrons in the direction of the wall while increasing the ion drift towards the wall, until a steady balance between the two is reached.

An example of a sheath profile of a helium plasma near the wall is shown in figure 2.1. The sheath is within a few debye lengths λ_{De}, with the potential drop being due to a decreasing $\frac{n_e}{n_i}$ ratio in the sheath. In order for this to happen, the ions at the sheath edge require a minimum speed towards the sheath called the Bohm velocity [22]:

$$u_B \geq \left(\frac{eT_e}{M}\right) \tag{2.25}$$

where M is the ion mass. This allows the ions to replenish the ion-rich sheath quickly enough to not be space-charge neutralized by the thermal electrons. This means that a small electric field is needed within the plasma called the presheath, in order to accelerate the ions so they can fit this criterion.

In DC discharges with relatively large arc voltages, most of the voltage drop tends to be across the cathode sheath. Within this high voltage sheath, the arc current contribution from the ions is much higher than that of the electrons, due to the higher ion density needed to keep the high voltage sheath. Because the sheath is dominated by the ions, the current density can be represented by the Child-

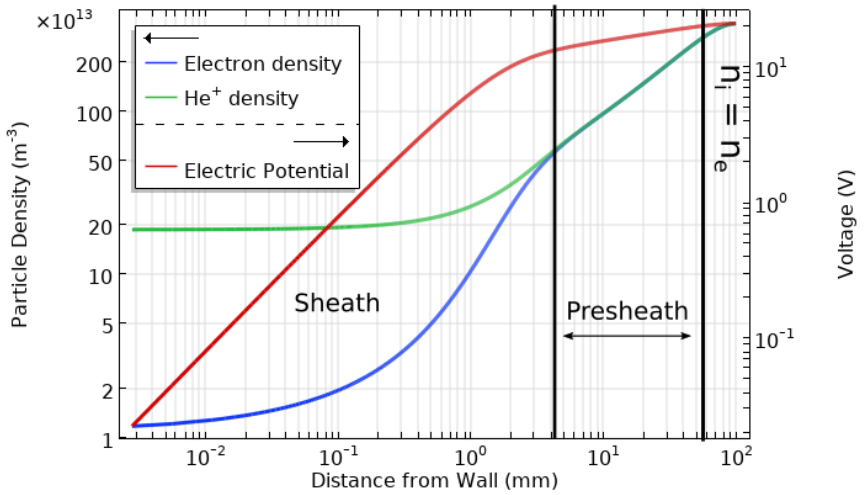

Figure 2.1: Spatial sheath profile example as a function of electron/ion density and electric potential.

Langmuir Law [22]:

$$J = \frac{4}{9}\varepsilon_0 \left(\frac{2e}{M}\right)^{1/2} \frac{V_s^{3/2}}{s^2} \tag{2.26}$$

where V_s is the voltage across the sheath, and s the sheath distance.

2.6.2 Electron Cathode Emission

Most of the arc voltage is across a small region on the cathode surface called a cathode sheath. The plasma is then sustained with high energy electrons originating from the cathode and accelerating across this sheath into the plasma. These electrons undergo several elastic and inelastic collisions with neutral particles, causing them to lose energy and scatter. Some of these inelastic collisions will be ionization collisions, which replace electrons/ions lost to the walls.

The most common source of electrons at the cathode is from *secondary emission* due to ion neutralization upon hitting the metal surface. As the ion gets close to the cathode, an electron within it can tunnel into the potential well caused by the ion and neutralize it. The extra energy from the reaction goes to another electron

within the metal. If this energy is enough to overcome the *work function* of the metal, which is the potential barrier confining the electrons within the metal, the electron can then escape from the metal. The probability of secondary emission from an ion is usually about 0.1 - 0.4 [24].

This sort of gas discharge is often called a glow discharge, which is a fairly low pressure (0.01 - 1 Torr), high voltage discharge commonly used in PIG sources. These discharges have most of the electric potential drop across the sheath, with quasi-neutral plasma within the bulk of the discharge's volume. At large enough currents, usually on the order of about 0.1 - 1 A, the ion bombardment on the cathode will be intense enough for the discharge to transition to a 'hot cathode' state. This is when ion bombardment heats the cathode to temperatures appropriate for thermionic emission. Thermionic emission is when a few electrons within the metal gain enough energy (due to the large bulk temperature of the metal) to overcome the potential barrier set by the material's work function. A discharge which relies on thermionic emission is often called an arc discharge. The current density of thermionic electrons on a metal surface at a temperature T with work function W_f is given by [21]:

$$J_e = \frac{4\pi me}{(2\pi\hbar)^3} T^2 \exp(\frac{-W_f}{k_B T}) \tag{2.27}$$

Figure 2.2 shows the arc voltage and current modes for general DC discharges. We see that the normal glow discharge is fairly constant, but then goes into an abnormal glow discharge. This is a positive differential resistance mode, which means that current and voltage are directly correlated. Once the discharge transitions into an arc discharge, an increase in current results in a decrease in voltage. This is called a negative differential resistance mode, where the resistance of the arc starts to drop quickly as the conductivity of the arc starts to increase. An arc discharge is usually ignited directly with a heated cathode at temperatures hot enough to generate large electron currents from its surface. However, arc discharges can also be ignited self-consistently by heating from the plasma ions bombarding it, which is called a self-heated cathode discharge.

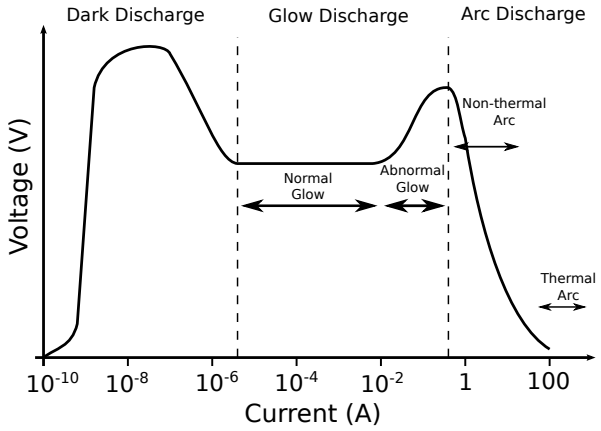

Figure 2.2: Example transitions between various states of DC discharges. The main three regimes are the dark discharge at low currents, where there is very little light emission, the glow discharge regime where light is emitted, and arc discharge where cathodes start to run hot and thermionic emission leads to large arc currents.

Chapter 3

Ion Source System Design

3.1 Magnet Design

One of the parameters that should change the properties of the plasma in an ion source significantly is the magnetic field strength, as this affects the confinement of the charged particles. However, a magnetic field complicates extraction of ions due to the curvature it imposes on the ions through the Lorentz force. This means that variations of magnetic field will create variations in the curvature of the ions, making it difficult to have the ions guided to one place for diagnostics such as current measurements.

The solution to this is to have a system as shown in figure 3.1, which shows a cross section of the ion source overlaid on a magnet pole. The magnet pole will be a c-magnet, with the ion source between the spacing of the poles. The magnet can then be used as the confinement field for the plasma, while simultaneously splitting the extracted ion trajectories based on mass to charge ratio following from their different gyroradii in the magnetic field (equation 2.21). In this case we assume the ions to be split will be mostly He^+ and α particles for a helium plasma. It is also assumed that the voltage between the ion source anode and the puller is 15 kV, which gives 30 keV α-particles, a typical beam energy for coupling to medical cyclotrons. The current from these ion beams can be measured by a Faraday cup (F-Cup for short) which can be moved along the axis perpendicular to the initial extraction of the beam. The F-Cup is essentially a copper block with a grounded

shield with a slit in front of it. Any charged particles that make it through the grounded shield slit is then measured as a current on the copper block. Thus even for different magnetic field strengths the ion beams can always be measured after doing a 180° arc trajectory. The remainder of the beam gets dumped on the beam dump behind this movable F-Cup.

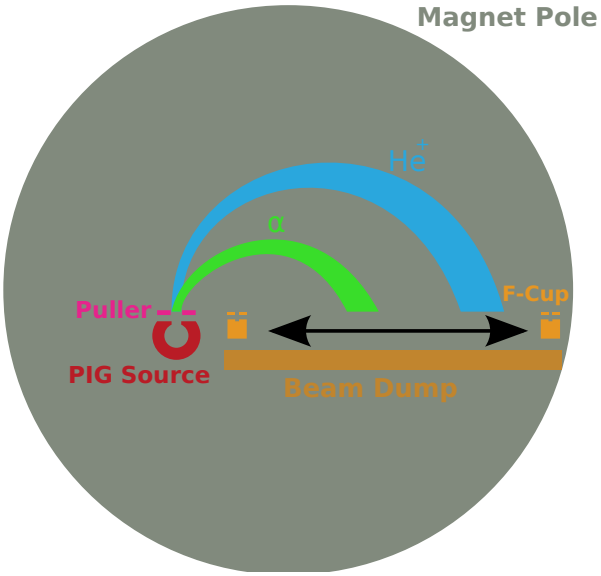

Figure 3.1: Simplified schematic of ion source beam diagnostic. The two particles (He^+ and α) rotate 180° within the magnet pole area where there is a strong magnetic field. A movable Faraday cup (labeled F-Cup) can then move along this axis and read out ion currents for various applied magnetic fields

The disadvantage of such a setup is that one needs a very large magnet pole area in order to measure currents in a large range of magnetic fields due to the proportionality of the gyroradii with the field (assuming constant extraction voltage between the puller and source). However, size and cost restrictions do not allow for such large field ranges, so a compromise must be made. An additional constraint is that the larger the gap between the poles, the more the magnetic field will leak outside the pole gap and bow rather than being only in the direction of the pole gap distance. This means that one has to also compromise between the magnet pole

gap and the actual size of the ion source. Furthermore, a magnet will be at ground potential along with the vacuum box, and so the ion source will be at 15 kV with respect to the poles, requiring an even bigger gap for high voltage (HV) insulation. This is detrimental especially for the confinement field inside the ion source, since electrons follow the field lines, and thus bowed magnetic fields mean part of the electron direction will be towards the anode, which could increase diffusion of the plasma electrons to the anode. For this reason, the ion source has to be placed in a region of uniform magnetic field with minimal bowing.

Most PIG sources in cyclotrons are quite long (up to 100 mm anode length), due to the large size of cyclotron magnets. However, space and cost restrictions have shortened the gap to 78 mm, allowing for a roughly 50 mm anode length. The overall area of the pole needs to be large to compensate for large gyroradii of the ions at lower magnetic fields. For a helium ion at a magnetic field of 0.4 T at 15 kV, the gyroradius is about 90 mm. The distance from the ion source extraction to where the ion current is read by the F-Cup is twice that, so about 180 mm. A maximum pole diameter of 270 mm was allowed for the design, and so to keep the ion rotation within the pole gap for this lower value of magnetic field, we need to have the ion source off-center, as shown in figure 3.1.

3.1.1 Magnet Simulations

The issue with having the ion source placed off-center is that the magnetic field lines bow the further you get from the center. Therefore, for the magnet, we need to make sure the field is still mostly confining in the ion source perpendicular to the pole-to-pole distance. The simplified magnet design is show in figure 3.2, with the grey being low carbon steel and the large block coils a simplified representation of several coil turns.

The magnet is simulated with the magnetic fields module in COMSOL Multiphysics™[25]. COMSOL™ is a program that solves many sorts of partial differential equations within many realms of physics and engineering. The module solves the magnetic field for some static case using stationary state Maxwell's equations for magnetic

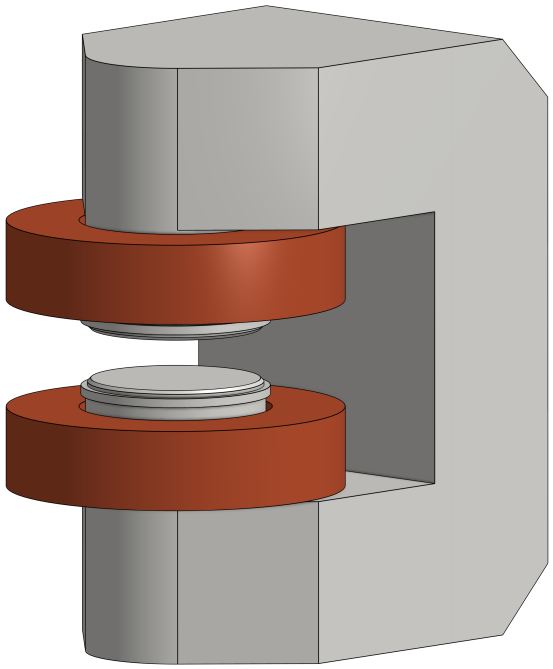

Figure 3.2: Simulation model of magnet. Pole gap is 78 mm, pole tip diameter is 270 mm. Material is low carbon steel 1010. Coils shown as solid block coil.

fields in a 3D mesh:

$$\nabla \times \vec{H} = \vec{J}_f \nabla \cdot \vec{B} = 0 \tag{3.1}$$

where $\vec{J}_f$ is the free charge current density. For further simplification and to reduce computation time, we can reduce the problem by taking advantage of the inherent symmetries of the magnet: the symmetry plane along the center of the pole gap, and the symmetry plane cut across the center of the C-magnet. It is important also to have a very fine mesh within the pole gap where we want fairly accurate results, along with a course mesh outside the magnet to take into account all the leakage field (field lines outside the magnet yoke or pole gap).

In order to keep the electrons confined along the field lines, the field lines should be along the pole-to-pole axis, which we'll call the $\hat{z}$ axis. To estimate how uniform the field lines should be, one can take the equation for diffusion in a magnetic field. In the tensor form of equation 2.24, one finds that the diffusion along the $\hat{r}$ axis within the ion source in the absence of electric field is proportional to [25]:

$$D_r \propto \frac{\left(\frac{1}{\mu_e^2} + B_r^2\right)}{\left(\frac{1}{\mu_e^2} + |\vec{B}|\right)} \tag{3.2}$$

where μ_e is the electron mobility, $|\vec{B}|$ is the magnetic field strength, and B_r is the magnetic field in the radial direction from the center of the PIG source. A way to estimate the severity of the bowed field is to take the ratio of the diffusion D_r including the B_r component of the magnetic field to the diffusion where $B_r = 0$. By evaluating this ratio for the ion source domain at various distances from the pole center, we can see how severely the bowing of the field effects electron diffusion for various ion source placements.

This is shown in figure 3.3, which shows the ratio of the volume-averaged diffusion coefficients with and without the simulated B_r component as a function of radial distance from the center. The volume in this case is the expected plasma volume of the PIG source, which is a cylinder of radius 4 mm and height 50 mm centered in the pole gap. The location of the center of this volume is the radius variable in mm, which is the distance from the magnet pole center. μ_e is taken to be about 1000 $\frac{m^2}{Vs}$ which is typical for the discharge pressures typically seen in low pressure helium discharges [26]. We see that the diffusion coefficient ratio goes up with increasing radius because of the increased components of field perpendicular to the pole gap. However, it is also seen that the ratio increases more dramatically at higher fields. This is because the magnetic field flux starts to saturate within the poles of the magnet, which causes the fields to leak out perpendicular to the pole gap as it becomes more difficult for the field to go through the magnet yolk.

It is clear that it is much more desirable to have the ion source closer to the center of the pole. However, this would limit experiments to very large fields, which limits the range of testable magnetic fields as lower field strengths would cause the

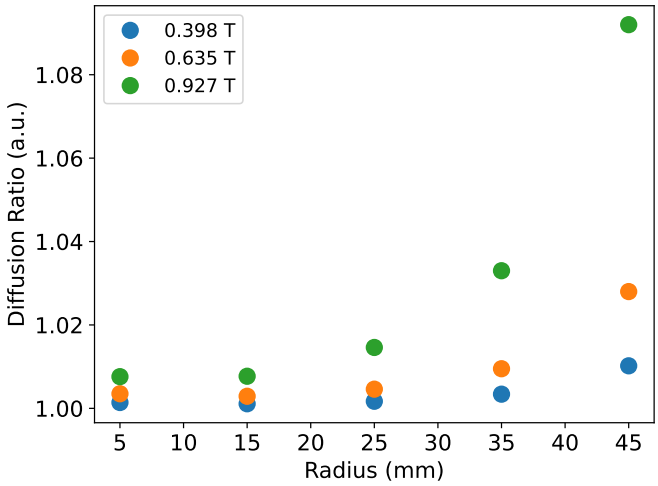

Figure 3.3: Volume-averaged radial diffusion coefficient ratio for electrons as a function of distance of ion source from center of magnet pole. The ratio is of the radial diffusion coefficient including the simulated radial field B_r to the coefficient without this component.

ions to travel outside the pole area. In addition, higher fields over-saturate in the magnet yoke, which means significantly more current on the coils are required to increase the magnetic fields. As a compromise, it was determined to put the ion source at a position within the pole area away from the center. If we consider the 2-D plane along the center of the pole gap, with $\hat{y}$ in the direction of particle extraction and $\hat{x}$ perpendicular to this axis, then the ion source is moved to a location of (-40, -20) mm, which restricts the diffusion coefficient increase to less than 10% its value without bowing. In figure 3.4, an example of the estimated particle tracing for extraction of 30 mA (black lines) of He^+ and 3 mA of α (white lines) at 0.4 T peak magnetic field (colormap of $|B|$) extracted at 15 kV is shown. Here we see that at this position, the particles are still able to do a 180° turn just within the area of uniform magnetic field strength.

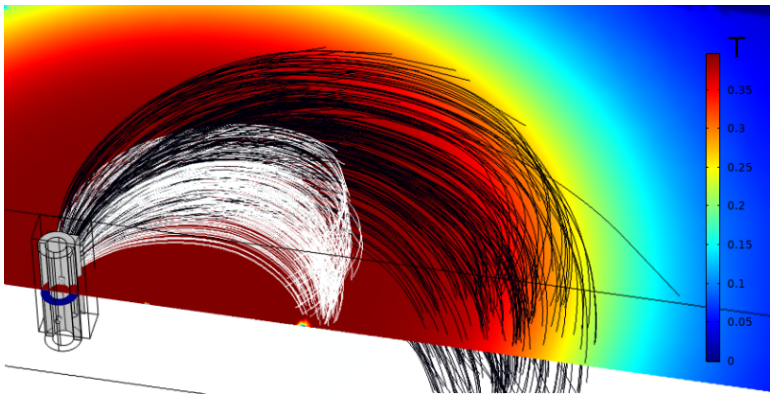

Figure 3.4: Color map is the magnitude of magnetic field along the center plane of the pole gap with a peak close to 0.4 T. Overlaid is an example of 30 mA (black lines) of He^+ and 3 mA of α (white lines) extracted at 15 kV. Space-charge effects due to the ions space charge deposition is included.

3.2 Vacuum Box

A vacuum box (V-Box) was designed from Aluminum 6061 and made so that the magnet pole is attached as part of the V-Box. This means the pole ends are directly in the vacuum, therefore keeping the gap distance to the required 78 mm. A cross section of the vacuum box along the middle of the pole gap plane is shown in figure 3.5. Here one sees the beam dump and faraday cup diagnostics shown, as well as the Penning ion source (design discussed later) within the magnet pole. The turbo pump shown is a HiPace™ 700 manufactured by Pfieffer Vacuum. This was chosen due to its size which allows it to be more easily used given the space constraints and size of the V-Box. A wide-range-gauge vacuum gauge will be attached to the end of the vacuum nipple as shown, in order to be far enough away from the pole gap so the fringe magnetic fields don't affect the measurements.

In order to estimate the pressure inside the Penning source, which cannot be measured directly, one can use the basic molecular equations for the escape of gas

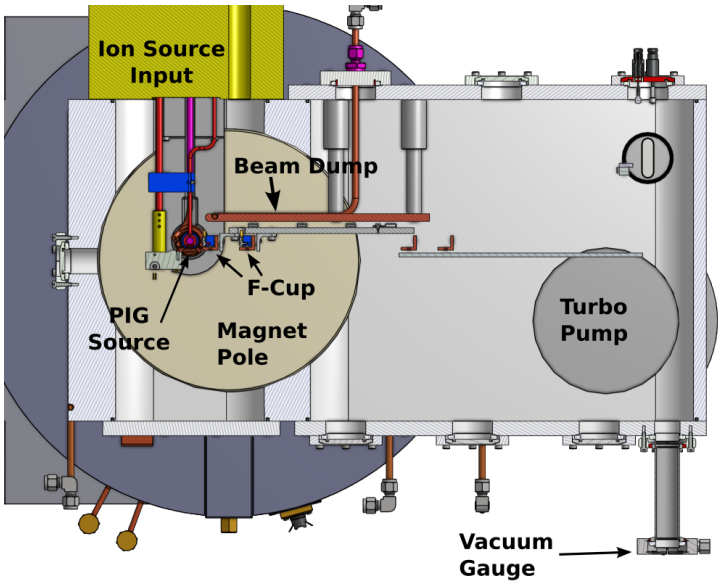

Figure 3.5: Cross section of Penning system with V-Box, magnet, ion source, and Faraday cup (F-Cup) shown. Faraday cups can move back and forth, and have a water cooled beam dump behind it. The ion source is inserted through a rectangular flange on the side. The location of the HiPace™ 700 turbo pump is also shown.

through an orifice. This is given by [27]:

$$\Delta p = \frac{Q}{C} = \frac{Q}{A\sqrt{kT_g/2\pi M}} \tag{3.3}$$

where Δp is the pressure across the orifice, Q the throughput of the gas through the orifice (which is also called the gas flow), C the conductance of the orifice, with A the orifice area. In the case of a Penning ion source, the orifice area is the slit of the ion source since this is where gas escapes to the vacuum box, which we nominally make a 1.5 mm $\times$ 10 mm rectangle. However, a more accurate way to determine the pressure inside is to use MolFlow+ [28], which is a Monte-Carlo code that traces elastic collisions of particles on walls to determine the pressure within a system. In this code, you introduce a gas flow from some point and for some gas (the mass flow of gas inside the ion source), and an output area on the

vacuum box with some pumping speed set by the turbo pump (655 l/s for helium). This assumes no collisions between gas particles, which is the regime of molecular flow. The reality is that at the flow rates expected (up to 40 sccm), the flow starts to get into transitional flow, which is fairly complex and cannot be easily approximated. As we are still in the low collision end of transitional flow with very large differences in pressure across the slit, molecular flow equations are a reasonable assumption.

A simplified CAD model of the V-Box and ion source was made to be imported into the MolFlow+ program. In experiments, helium gas will be introduced along a gas line with a mass flow controller in series, which measures a gas flow in sccm (standard cubic centimeters per minute), which goes from $0 \rightarrow 40$ sccm for helium gas. This gas assumed to be at T_{room} = 293.15 K goes through the gas line into the ion source and comes out through the slit into the vacuum chamber. The average number density within the ion source is solved for as a function of input gas flow in sccm, which follows a linear trend. However, the neutral density may change within the source due to changes of gas temperature in the plasma. To account for this, we can use equation 3.3 but with the assumption that the conductance estimated from Molflow+ is still proportional to only the square of the gas temperature in the source, and that the flow of room temperature particles going into the ion source volume is the same as the flow escaping from the orifice at whatever the gas temperature becomes in the source:

$$n_g = n_{room}(q_{pV}) \left(\frac{T_{room}}{T_g} \right)^{3/2} \tag{3.4}$$

where n_g is the gas density inside the source at temperature T_g, and n_{room} is the calculated gas density in the source from the Molflow+ simulations at room temperature T_{room} = 293.15 K. By fitting n_{room} as a function of Q from Moflow+, we get:

$$n_g = \left(1.247 \times 10^{20} q_{pV} - 2.026 \times 10^{18}\right) \left(\frac{T_{room}}{T_g} \right)^{3/2} \tag{3.5}$$

3.3 Igniting and Sustaining a Plasma

It is expected that higher arc currents will generate larger ion beam currents due to an increased amount of plasma electrons for ionization and therefore a higher ion density. This is what is typically seen in literature for high-charged state Penning ion sources as well [8, 10, 16]. In the literature mentioned before, most Penning ion sources used for high-charge states found were either self-heated cathodes, filament arc cathodes, or heated cathodes. For this project, self-heated cathodes were chosen as the primary mechanism due to the greater simplicity of design, longer lifetimes, and to save the usable space within the magnet pole gap.

A simplified schematic of the electronics used for the plasma is shown in figure 3.6. The entire anode of the PIG source is elevated up to 15 kV with respect to local ground. There is also a plasma power supply (plasma PS) which is a Glassman EV series which can operate up to 750 V and 4 A. This is the main driver of the plasma arc in the ion source. However, for a self-heated cathode, a plasma must first be ignited, and the cathode heated enough by ion bombardment of the plasma to sustain thermionic emission. To do this, a 100 μF capacitor is charged up to 5 kV using the CCPS (capacitor charging power supply, CCPF-500 from Lumina Power) while the plasma ignition switch is open. After charging, the switch is closed, and the capacitor is discharged across the PIG source thus igniting the plasma. If there is enough energy and a high enough pressure, the large amount of energy stored in the capacitor allows the plasma to reach a low voltage, high current state, after which the plasma PS takes over. To protect these power supplies from discharging into each other, a pair of high voltage rectifiers is used to block back-current into these power supplies. A 200 ohm resistor is used to prevent arcing from the capacitor discharge. The 13 mH inductor is used to stabilize the arc by preventing high-frequency oscillations.

3.4 First Ion Source Design

A PIG ion source was designed to be placed as shown in figure 3.5. Figure 3.7 shows a vertical cross section of the ion source, with the various components labeled. The anode was made of graphite to be cooled via radiative emission, which is separated by the cathode with Shapal Hi-M Soft™, an electrical insulator with

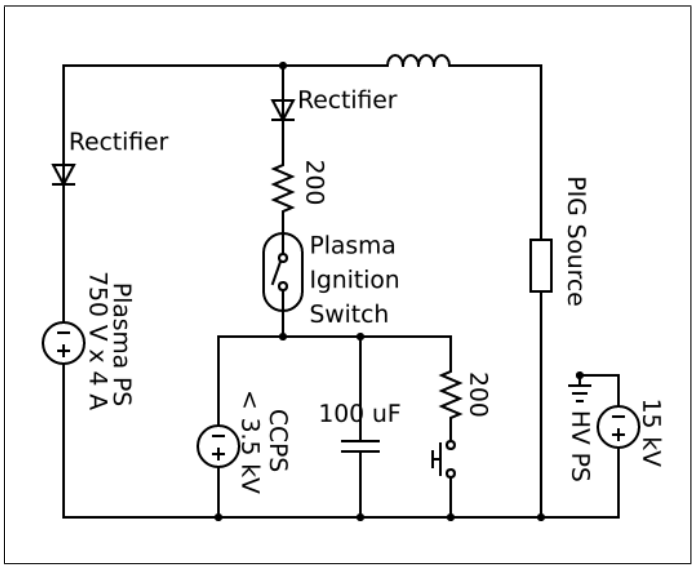

Figure 3.6: Schematic for electronics used in PIG ion source ignition.

relatively high thermal conductivity. The cathode is made of tantalum as it has low sputtering relative to other metals and a high melting point which allows it to get to thermionic emission temperatures. It also has a low work function of 4.2 eV which also eases the transition to thermionic emission. Shapal™ insulators separate the HV (high voltage) components from the grounded magnet pole on the top and bottom.

Work was put into simulating, designing, and manufacturing this ion source. In addition, the experimental setup also included modifications to the ISTF with setup of the stand, setup of the PLC controls, and setup of all electrical, vacuum, and plumbing connections. An example of the setup is shown in figure 3.8. However, this ion source did ultimately fail under high voltage.

Figure 3.9 shows an example of a discharge along the insulators separating the anode and cathode voltages which was typical when trying to ignite a plasma at 15 kV. This would happen after several bright sparks. Many modifications were done in order to decrease this sparking such as precision cleaning of the parts, shortening of puller electrode, and replacing of HV parts with insulators. However, ultimately there was always consistent sparking and the ion source could not be operated

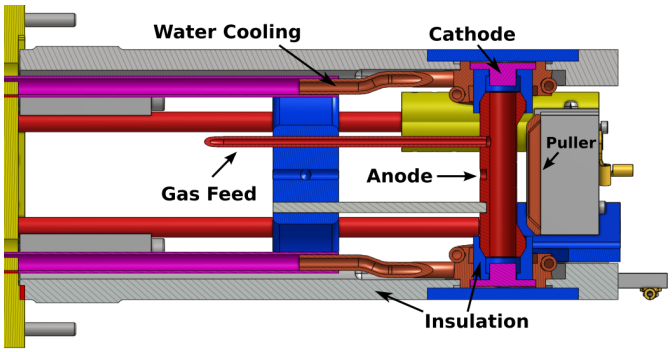

Figure 3.7: First PIG ion source design, with different parts labeled.

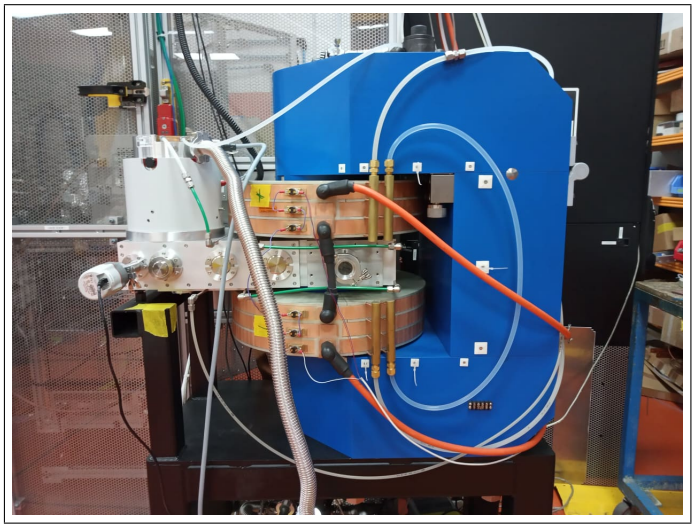

Figure 3.8: Example picture of the overall setup, with the magnet, vacuum box, turbo pump, water cooling lines, and stand shown.

correctly. In addition, one may notice that other insulators are used for movement of the puller, which comes from rods from the HV side. This also led to various issues with sparking.

There are likely two reasons for this, and it has to do somewhat un-intuitively with the insulation. Insulation can actually make HV operation worse, due to the existence of triple points, which is where the electric field at the meeting place

Figure 3.9: Glowing discharge along insulators shows primary area of HV breakdown.

of an insulator and electrode will be stronger than expected due to the reduction of electric field within the dielectric. An example is shown in figure 3.10, which shows a axially symmetric model of two thin electrodes with 15 kV on top and 0 V on the bottom separated by 4 mm. The grey portion is an electrical insulator with relative permittivity of 6 between the electrodes. Without the insulator we'd get a uniform electric field of 3.75 kV/mm. We see however that the electric field becomes much higher in the space where the insulator meets the electrode, which is because the insulator reduces the field within it, making the field larger in the gap. This can cause field emission of electrons from the electrode, which collect on the insulator generating sparks along it, which turns the outside into a conductive track for other sparking events.

Another issue with the insulator is that any electrons which are created near the puller, either due to ion bombardment or ionization of background helium gas, will go along the field line to collect on the insulator, which will also lead to charge collection and eventual sparking. So it is clear that insulators should be avoided wherever possible in order to decrease the strong fields and consequential breakdown of these insulators. In addition, it has been found experimentally by some ion source users that sparking within vacuum between electrodes can be beneficial, as it can lead to the destruction of whatever surface contaminants on the electrode is initiating the sparks. This is known as *conditioning* of the electrodes.

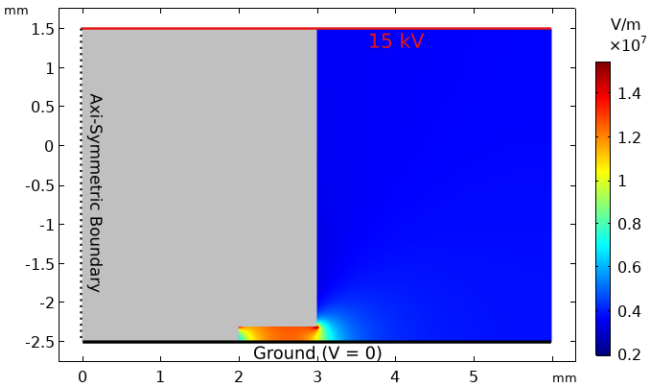

Figure 3.10: Simulation of two axi-symmetric 6 mm radius electrodes separated by 4 mm. Lower boundary is ground, upper boundary is at 15 kV. Grey is an electrical insulator of relative permittivity of 6.

3.5 Second Ion Source design

A second ion source was designed to fix the issues with the previous version. The first requirement was to make a design that avoids the use of electrical insulators as much as possible to avoid potential triple points and charged particle collection at extraction. The geometrical restriction is that it must go in as one piece at the same flange on the V-Box as the old ion source (see figure 3.5), as time restrictions does not allow for another re-design of the rest of the system. A CAD model view of the ion source inside the V-Box is shown in figure 3.11. An additional view showing the other side with the bracket and cooling tubes is in figure 3.12.

3.5.1 Electrostatics

To prevent potential sparking, it is important to limit the electric fields. As a conservative estimate, it is recommended to keep electric fields less than 3 kV/mm [29], which is the approximate breakdown field in atmosphere. The electric field is simulated with the AC/DC module of COMSOL Multiphysics™, which solves Poisson's equation for electrostatics:

$$\nabla \cdot \vec{E} = \frac{\rho}{\varepsilon} \tag{3.6}$$

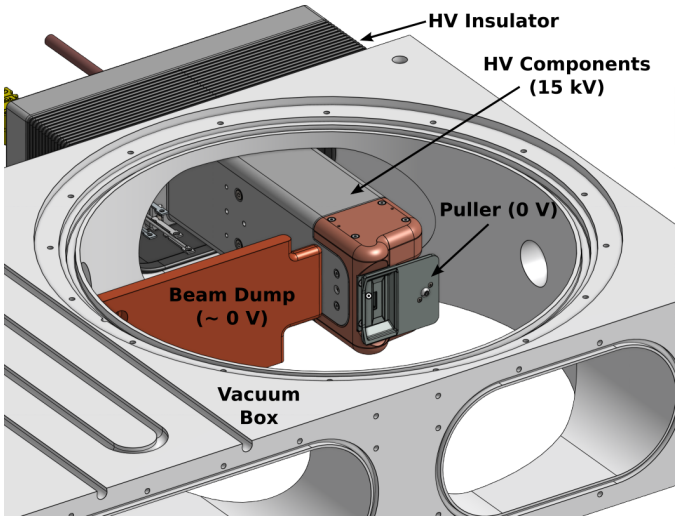

Figure 3.11: Ion Source CAD design shown in V-Box. The ion source is floating at up to 15 kV with respect to the grounded puller, V-Box, and Beam Dump around it.

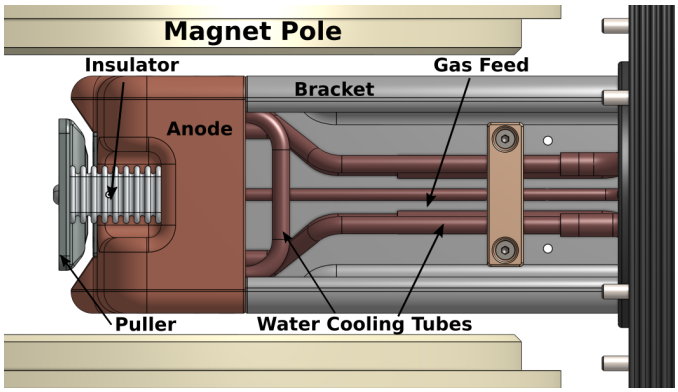

Figure 3.12: Ion Source CAD design shown with hollow bracket and water cooling copper tubes used to cool the anode and cathode. Also shown is the insulator which separates the large copper anode and the grounded puller. Relative position to magnet poles also shown.

where ρ is the total volume charge density, and ε is the permittivity of the medium. The largest obstacle is the vertical spacing between the magnet poles, as in order

to have 3 kV/mm fields, the minimum theoretical spacing required between the 15 kV components and grounded magnet is 5 mm (for infinitely flat electrodes). This leaves a maximum of 68 mm of the 78 mm spacing within the pole gap to fit the ion source. In addition, the beam dump and vacuum feedthrough also provides a space limitation perpendicular to the pole gap.

Given the constraints of the system, 3 kV/mm could not be achieved since the ion source has to curve up with respect to the grounded V-Box. An example of a 2-D slice of a fully 3D electrostatic simulation solved for the 15 kV components with respect to a surrounding grounded boundary is shown in figure 3.13. Here we see that the field at the corners is slightly higher than 3 kV/mm limit (close to 3.1 kV/mm). This is at 6 mm clearance between the HV components and the bottom/top of the V-Box. However, in order to further decrease the field, one would need to decrease this clearance, which impacts the space needed for the cathodes and plasma chamber. The plasma chamber especially we want to keep as long as possible, since it's already shorter than most high-charge state producing PIG sources found in literature, and a longer plasma column is necessary to increase the trapping efficiency of electrons emitted from the cathodes due to a greater distance traversed in the background gas.

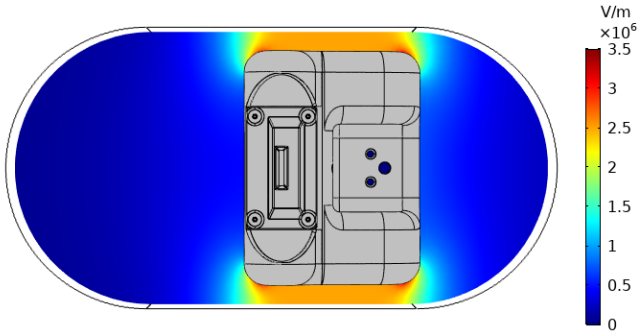

Figure 3.13: 2-D slice showing electric field strength in V/m. 15 kV components are in grey, the surrounding wall is representative of the grounded V-Box. The corners surpass the limit of 3 MV/m and peaks at about 3.1 MV/m.

To make up for this, the ion source and its exposed HV components have been made with as large a radius of curvature as possible in order to decrease the curvature of the electric equipotential lines. This then decreases the electric field strength since $\vec{E} = -\nabla V$. However the curvature cannot be too large, as this extends the HV components perpendicular to the pole gap, which then brings the HV components closer to the beam dump and the inner walls of the feedthrough. For this reason, it was considered a reasonable risk to have the corners be over the 3 kV/mm limit as it is already a conservative estimate.

There will be areas where insulators are necessary though, in which case, it is necessary to avoid triple points and electron collection. For the insulator between the puller and anode (see figure 3.12), it was first necessary to push the distance between points of contact on both electrodes as much as possible. Hence why the insulator is somewhat embedded into the anode. It is also pushed to the side to be away from the large fields found at the extraction point of the puller and anode. It is also typical for these insulators to be ribbed to increase the surface area in case there is any conductive path created along its surface. However, this feature is also implemented for another reason, as shown in figure 3.14. The ribbed feature also adds plenty of vacuum space between the HV electrodes where the field is stronger compared to inside the insulator. This also means that if there is a triple point at the ends due to a small amount of space between the insulator and electrode contact, the field will be reduced because a stronger field within the grooves will compensate for this. This is why the grooves were also used on the HV insulator, which was also simulated to make sure the field strength was much less than 3 kV/mm.

3.5.2 Ion Extraction

COMSOL Multiphysics™ has a module called the Charged Particle Tracing module which can be solved with a bi-directional time-dependent solver. This works by first solving the electrostatics for some 2-3 dimensional geometry. Afterwards, a set of charged particles with some initial conditions (charge, mass, velocity, location) are released and their path within the simulation space is solved using basic time integration of the force equation due to the forces from the electric fields.

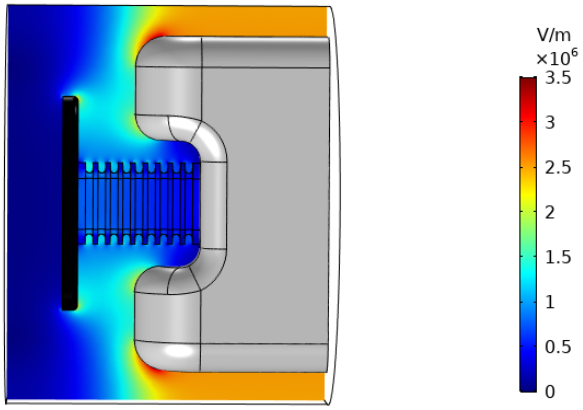

Figure 3.14: Magnitude of electric field along 2-D slice of insulator, with anode in grey (15 kV) and puller in black (ground). The electric field magnitude is less than 3 kV/mm, and the grooves along the insulator help prevent field from getting too strong at the triple point regions.

These charged particles are often called *macroparticles*, which represent a cluster of several charged particles to decrease computation of the many trillions of particles that are actually produced. The dependence on a constant magnetic field can also be added. After allowing the particles to move for some set amount of time, the final space charge deposition of the particles (the integrated sum of charge which goes through a mesh volume) is solved for, which is then used as an additional source of electric fields in the electrostatic solver. This cycle then repeats for a set amount of iterations, which allows for the space charge of the particle beam to be taken into account.

For the extraction of ions from the source, it is important to have most extracted particles go through the puller so that they can be measured by the Faraday cup without worrying about whether a significant amount of He^+ or α have hit the puller, since we cannot distinguish between them on the puller. However, pullers come in various shapes, and we want to determine what is the optimal shape for extraction of these particles to go through the puller slit. The basic ways a puller can be changed with respect to some constant anode slit (which will be nominally 1.5 mm $\times$ 10 mm) is the puller to anode distance, the offset of the two slits centers,

the outer chamfer angle of the puller ends, the puller slit width and height, the inner chamfer angle for both the anode and puller, and the distance between the anode slit edge and the inner chamfer. These will nominally be 3 mm, 0 mm, 2 mm, 2.5 mm $\times$ 11 mm, 30°, and 1 mm respectively. A visual example of these can be seen in figure 3.15.

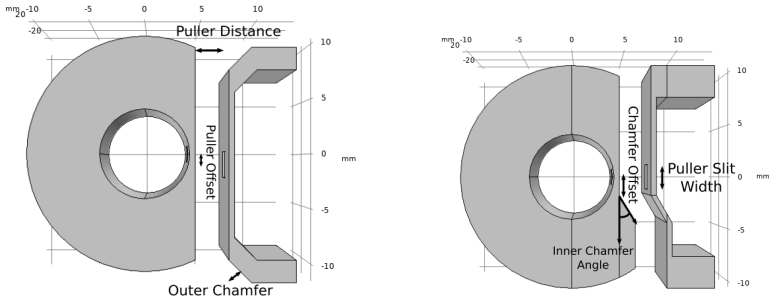

(a) Basic model **(b)** Anode and Puller Chamfer Model

Figure 3.15: CAD models used for studying extraction of helium ions from PIG source using Charged Particle Tracing with space charge effects in COMSOL™. Model (a) allows for variations of outer chamfer angle (expressed as distance from the corner), puller slit offset from the anode slit, and the distance between the puller and anode. Model (b) introduces an angled chamfer to offset the magnetic fields, in addition to the offset of the chamfer from the anode slit edge, and the puller slit dimensions.

For both models, an array of He^+ and α particles are introduced uniformly on the slit's projected surface about 0.1 mm from the outside of the anode slit. So this plane is between the inner plasma column and outside extraction area of the slit. In order to represent a worst case scenario of maximum beam divergence due to the space charge of a high current beam, an estimated beam current of 20 mA is used for He^+ (1000 macro-particles) and 2 mA for α particles (300 macro-particles). These are estimated from beam currents of heavy charged particles from PIG sources in literature. The anode is at 15 kV and the puller and a rectangular boundary around it, representing the vacuum box, is at ground. The vacuum box is made only a bit larger than the space outside the puller simply to establish a ground potential after the particles go past the puller slit. A larger ground box is avoided to

prevent even longer simulation times due to a larger mesh volume required. In order to force all particles to be extracted, the boundaries at anode potential force the ions to be bounced off, so all inlet particles have to be dumped on a grounded wall, maximizing the space charge potential. The temperature of the particles are set to a large value of about 5000 K, higher than expected in these ion sources which should represent a worse case scenario for temperature-dependent divergence. A total of 10 iterations were used in order to get to a convergent solution. The purpose is to design a puller that allows most particles to be extracted without bombarding the puller in the worst case scenario.

Figure 3.16 shows the resultant currents of He^+ and α particles on the puller for the COMSOL™ model shown in figure 3.15a. We see in figure 3.16a that having an offset between the anode and puller slit (in the direction of magnetic Lorentz force) can compensate for the curvature of He^+ particles due to the magnetic field especially at higher fields of 1.1 T. However, we see that the amount of particles hitting the puller does not change significantly for either particle, likely because of the strong space charge deposition from the beam. Figure 3.16c shows that a decreasing distance will increase the amount of particles that go through the puller slit for both particles simply because the larger acceleration from the electric field then offsets the magnetic force. However, it is not recommended to place the puller too close though, as the electric fields will be strong enough to ignite constant sparking between the electrodes which will prevent proper operation of the source. From figure 3.16b, we see that the outer chamfer angle does not strongly affect the particles, meaning that bending of the electric potential here does not significantly affect the bending close to the extraction slits.

We see a weak dependence when changing the slit height on the puller (figure 3.16d) since the electric field will simply be stronger toward the slit edges along its length. This will lead to slightly more divergence for the slow He^+ particles perpendicular to the magnetic field causing more to hit the puller edge, but this is delayed for the α particles likely due to their stronger acceleration and the effect of the He^+ space charge deposition. However, increasing the slit width (figure 3.16e) clearly decreases puller bombardment in both cases. However, the vertical (along the slit height) divergence of the beam does increase within the simulation, likely because the vertical electric field components increase near the slit. This is not

desirable since the Faraday cups slits are only about 60 mm tall, so this should also be limited.

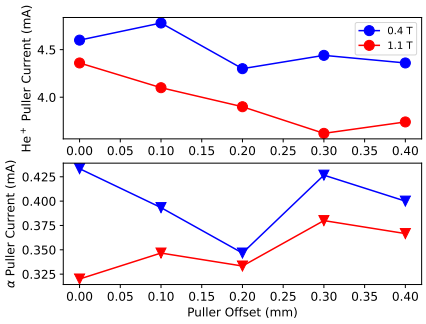

(a) Currents vs Puller Offset

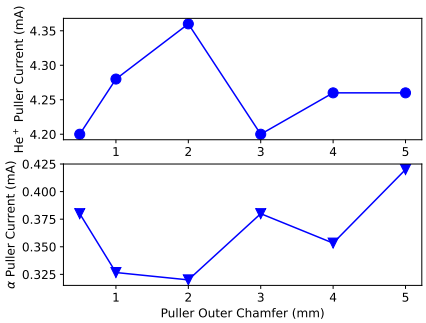

(b) Currents vs Puller outer chamfer (1.1 T)

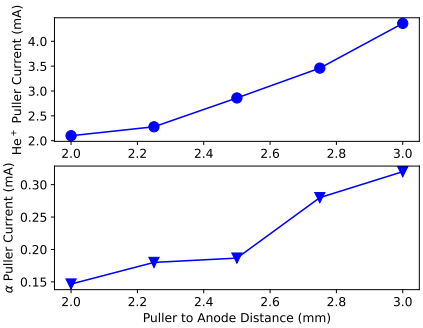

(c) Currents vs Puller distance (1.1 T)

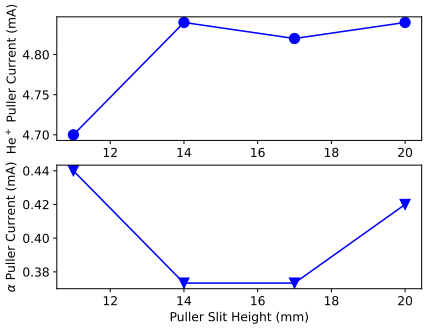

(d) Currents vs Puller slit height (0.4 T)

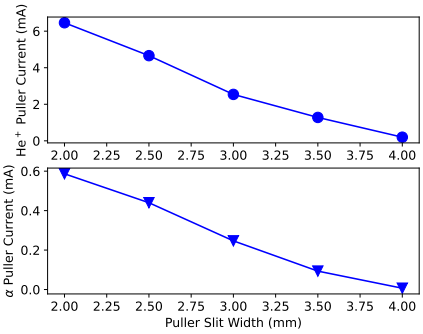

(e) Currents vs Puller slit width (0.4 T)

Figure 3.16: Sweep of parameters of puller offet (a), puller outer chamfer (b), puller distance from anode (c), puller slit height (d), and puller slit width (e) with the resultant current for each particle on the puller. These are based on the model shown in figure 3.15a

A possible way to offset the curvature of the magnetic field is to introduce an angled chamfer on one side of the anode and puller slits to create an electric field that counters the force from the magnetic field. Figure 3.17a shows how the angle of this chamfer does offset the magnetic field as less particles hit the puller at 1.1 T. It is clear that the weaker magnetic field is easier to offset with an electric field, hence why the puller currents are smaller at weaker fields. However, it does seem that at weaker fields, the lower charge state is actually overly effected by the fields, causing a larger divergence of the beam which hits the puller. Figure 3.17b shows that the increasing offset of the anode chamfer from the anode slit weakens the component of the electric field which can offset the magnetic force near extraction, which causes more particles to hit the puller regardless of magnetic field strength.

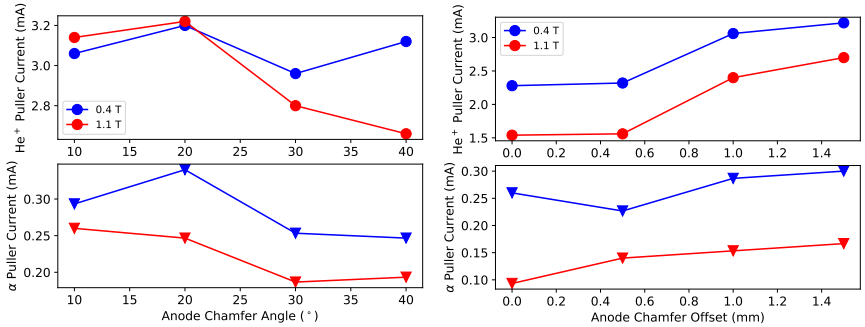

(a) Currents vs Chamfer Angle **(b)** Currents vs Chamfer Offset

Figure 3.17: Sweep of parameters of a) Anode chamfer angle and b) Anode chamfer offset with the resultant current for each particle on the puller. These are based on the model shown in figure 3.15a

From these simulations, a design was settled on which would include an angled chamfer of 30° offset about 0.5 mm from the anode slit. The slits on the anode and puller are offset by about 0.23 mm, with the distance between them about 2.3 mm. These combinations are chosen so that the puller and anode combination can work at a range of magnetic fields while minimizing the amount of particle bombardment on the puller. A test model of this configuration was simulated similarly to previous studies, and it was found that no particles hit the puller for magnetic fields up to about 0.8 T at 15 kV extraction.

A cross section of the final puller and anode slit designs is shown in figure

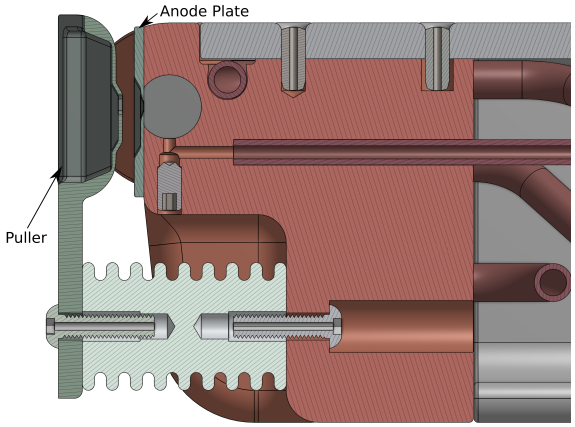

Figure 3.18: Cross Section of ion source which shows the puller and anode plate. Both puller and anode plate have symmetric slants so that the electric field can offset the magnetic field curvature. The anode and puller slits are also slightly offset.

3.18. The anode slits are on a metal plate which is bolted onto the anode chamber. The puller is bolted to an electrical insulator which is also bolted to the anode on its other side. The puller is immovable to avoid issues with the movable puller controlled from the HV side in the previous version. The primary reason for the anode being on a bolted slit plate is so that future experiments can have different anode slit geometries, including a geometry used for a movable puller. This movable puller would come in from the free flange on the other side of the vacuum chamber to keep it well grounded.

3.5.3 Electron Trapping

First experiments found that the new ion source could sustain up to 15 kV without beam for all magnetic fields and inlet gas flows up to even 40 sccm, which corresponds to a helium background pressure of about 5×10^{-4} Torr. This is a massive improvement over the last model which couldn't sustain these voltages. However, when igniting a plasma for beam extraction past about 6 kV extraction voltage, severe discharges were continuously formed at the back HV insulator, creating severe

scorch marks and cracking of this insulator. Consequently, the HV power supply was unable to hold extraction potential therefore rending the ion source inoperable. Charged particle tracing simulations show this is not due to low energy ions bouncing along bracket wall to the insulator since they'd get pushed vertically to the grounded magnet poles rather easily. However, electrons are not completely tied to the electric field lines, as they will undergo what is called an E×B drift, which is what happens when a charged particle is in a perpendicular electric and magnetic field. They will then have a drift velocity defined by [23]:

$$v_E = \frac{\vec{E} \times \vec{B}}{\vec{B}^2} \tag{3.7}$$

where v_E is the drift velocity due to this drift. This happens because of the change of the charged particle's gyroradius when in different parts of the electric field, which causes the particle to move perpendicular to the two fields. Within the experimental setup, this essentially allows electrons to move across very high electric fields perpendicular to the magnetic field without being dumped on any electrodes because of their tiny gyroradii. This drift is represented in the center of the vacuum box as red arrows in figure 3.19 (from COMSOL™ electrostatic simulations), where the grey boundaries and transparent walls are at ground, and green is at 15 kV which represents the ion source components. All arrows go directly to the back insulator on the side, which is exactly where the scorch marks are seen. So it would seem that the electrons that are generated, likely through either ion bombardment of the puller or ionization of the background helium, then get transported to the insulator through the E×B drift. These electrons collect on it until the charge density becomes large enough to ignite sparking along the insulator.

Combating this completely requires a complete change of the orientation of the ground and high voltage electrodes, though time and cost prevents another complete overhaul of design. However, a novel technique for trapping these electrons was made by designing a set of electrodes which connect to the beam dump (connected to ground through a 510 Ω resistor) and the HV bracket. This is shown in figure 3.20. The electrodes were designed over a few iterations to find what best reduced the fields using electrostatic simulations. In the end, like the ion source design, fields could not be reduced to less than 3 kV/mm everywhere due to limited

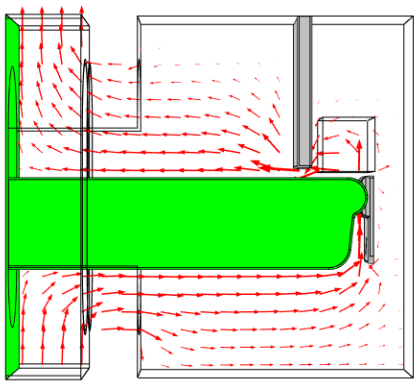

Figure 3.19: E×B drift direction and logarithm of magnitude along the center of the magnet pole gap. Green is a representation of the anode potential at 15 kV, and grey is the ground potential. Vacuum walls are also at ground, but are made transparent for visibility.

space. The electrodes work as shown in figure 3.20b, where the E×B drift forces the electrons to either get trapped on the flat part of the wing electrode in the center, or it continues to follow the E×B drift between the two electrodes until it arrives within the 'wings' of the wing electrode. In this area, a component of the electric field points along the magnetic field, allowing the electrons to be dumped on the inner wings before drifting to the insulators. The beam dump extender electrode is kept larger in height than the HV ion source components to make sure that there is a component of the electric fields that push the electrons towards the center plane of the V-Box. Otherwise electrons would be able to go up and around the beam dump extender.

In addition, some electrons may come from divergent ions which go through the 2 mm space between the beam dump and magnet poles, which then emit electrons via secondary emission after hitting the poles. A simple aluminum piece was made to shield this spacing to prevent this. After design and manufacture of the electron trap electrodes, they were placed inside and the ion source could then go up to 15 kV with beam extraction. There were still very light scorch marks on the insulator likely due to some electrons that can escape the trap, but the ion source is now fully operable. Figure 3.21b shows scorch marks on the wing electrode which

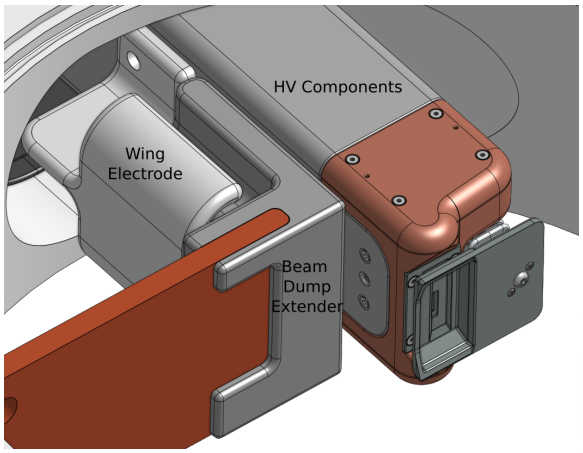

(a) Outer View

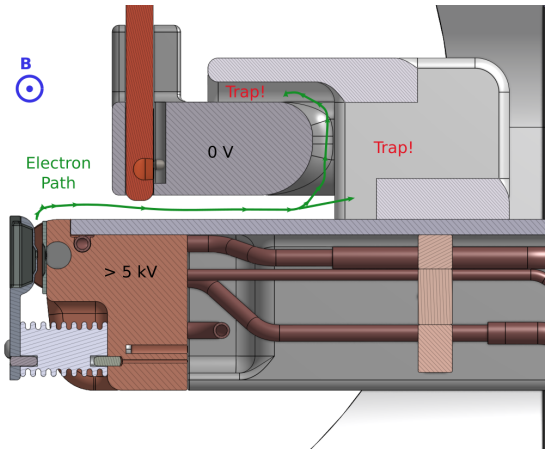

(b) Cross section view

Figure 3.20: Outer and cross sectional view of the added electrodes used as an electron trap. Figure (a) shows the outer view with the two electrodes with respect to the ion source, and (b) shows how the trap mechanism works with a cross sectional view.

are the electron dumping spots predicted by simulations, which are shown in figure 3.21a. This is a simulation of the electron drift for electrons which originate near the puller. The colored dots show the final dumping spots of each electron within the domain and their final kinetic energies, whilst the lines are their paths. This is evidence that the electron trap works exactly as intended and is the reason why the

ion source could now be operated. It should be noted that other simulations which change the origin of the electrons, such as on the puller or beam dump surface, show the electrons still go towards the trap.

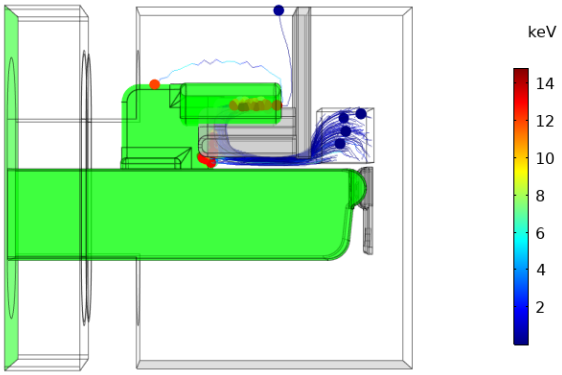

(a) Simulation of Electron Trap

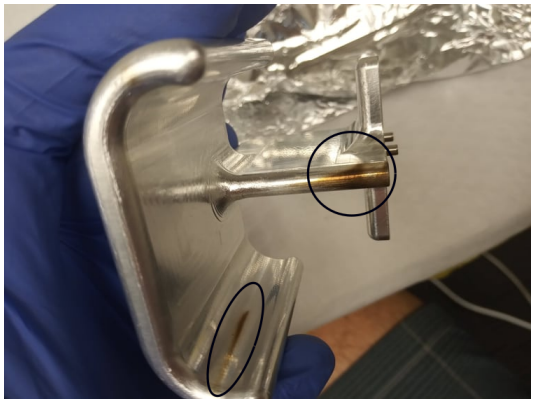

(b) Marks on Wing Electrode

Figure 3.21: Figure (a) shows a charged particle tracing simulation of the electrons born near the puller over time when 15 kV (green) is applied to the ion source and everything else is grounded (grey and transparent). Color bar shows the electron energy in keV. 99/100 electrons are dumped on the wing electrode. Figure (b) shows a picture of the wing electrode after use, which shows scorch marks exactly where electrons are predicted to be dumped.

3.5.4 Cathode Heating

For a self-heated cathode, the cathode must get hot enough from ion bombardment to emit thermionic electrons. However, it is also important to not let other components get too hot, which can cause mechanical warping, cracking, and additional electron emission that can generate parasitic sparks.

So in order to get high currents, one needs a metal with a low work function that can reach the high temperatures required for thermionic emission. Refractory metals like tungsten, molybdenum, and tantalum are often used since they fit these requirements. Tantalum was chosen since it generally gives the best compromise between a high melting point, a low work function, and low sputtering rate [10]. Sputtering is important to consider since the ion bombardment will cause the metal to be sputtered which then coats the surrounding walls and insulators, possibly leading to a short between the anode and cathode. It can also lead to a change in the plasma chemistry or even a reduction in the plasma geometry if the sputtering is severe enough to create a few tantalum layers on the walls. This was noticed directly on the first ion source iteration.

A CAD view of the final design is shown in figure 3.22. The tantalum cathode has a thin neck to prevent too much conductive heat transfer to the cooling block, therefore keeping the cathode hot. The face of the cathode facing the anode column is 10 mm in diameter, larger than the 8 mm diameter of the anode column. An additional MACOR™ insulator is placed between the cathode and cooling block for additional thermal conductivity. Electrical and mechanical contact is made by screws holding the cathode down on the copper cooling block. This block is at cathode potential and is cooled by de-ionized water through copper tubes fed through from the outside of the vacuum. The anode block is made of copper and is also cooled by de-ionized water in the same way. The cooled copper block is electrically separated by two stacked Shapal™ insulators from the anode block. This insulator is cut and stacked in two pieces so that it covers the spacing between the anode and cathode potentials. This makes most of the gas within the plasma column escape through the anode slit.

Two changes in this design were made after initial tests sustaining an arc discharge. The first is that despite most of the plasma bombardment being on the

cathode surface facing the anode column, tantalum was still able to coat the insulators which reduced the effective electrical resistance between the anode to cathode. Hence why rough cuts were made to the insulator (see figure 3.22) which makes the cathode block act as a shield for these sputtered atoms. On the side of the cooling block closer to the cathode (without the curve), it turned out a far cut would not work, so a piece of stainless steel was placed into a socket to act as a sputter shield for the electrical insulator on this side.

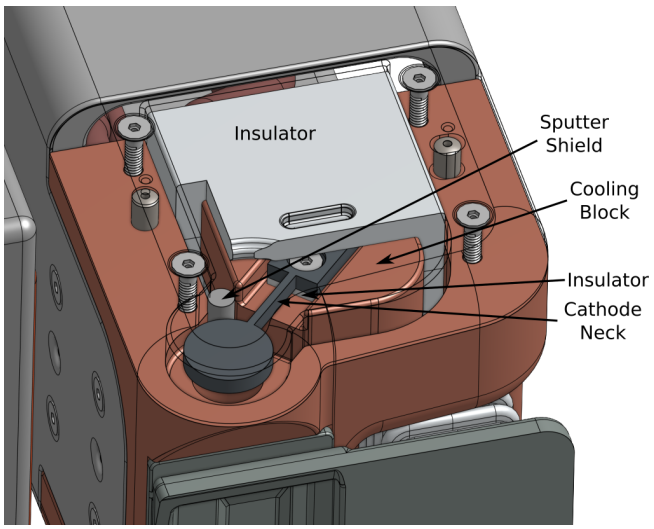

Figure 3.22: CAD view of cathode design. Cathode is made of tantalum, and screwed to a cooled copper block with screws. A thin thermal insulator piece is between the copper block and tantalum for extra insulation. This cooling block is separated from the anode housing by an electrical insulator. This insulator is cut-out to prevent sputtered tantalum from coating it. A sputter shield is placed on one side.

The other change was the addition of the MACOR™ piece used for extra insulation. The design was simulated using the Heat Transfer Module in COMSOL™ which can solve for conductive, convective, and radiative heat transfer given the materials in the simulation domain. It is not known what the power on the cathode will be, so it is unknown what cathode neck thickness is needed to keep a certain temperature. However, one can simulate how the surface temperature, and there-

fore the expected thermionic current, changes for different cathode thicknesses given a certain power deposition.

An estimated maximum power of 1 kW is assumed for the total PIG source based on what has been observed with other self-heated PIG sources using helium [16]. It is assumed that part of the power goes to the cathode surface facing the anode column and another portion on the inner surface of the anode column. It is unknown what the power proportion is expected to be, though due to the high voltage sheath near the cathode which is the predominant method of ion escape (therefore large ion energies bombarding the cathode), it is estimated that the portion of ion current (and therefore power) on the cathode could be up to 50%. The heat transfer equations are solved in the steady state for several cathode neck thicknesses and different proportion of total power (1 kW) going to the cathode. The heat transfer coefficients for the water cooled parts assume water velocity of 5 m/s and temperature of 30°C. The thermal conductivities and heat capacities for the various parts are taken directly from the COMSOL™ library of materials. Radiative heat transfer from the hot cathode head and neck is considered with an emissivity of 0.3. The resultant average anode column temperature and integrated thermionic current on the cathode head (solving equation 2.27) is shown in figure 3.23 as a function of the portioned power on them. Even at 100 W cathode power (900 W on the Anode column), we see that the anode column temperature is maxed at about 87°C which is well below the glowing temperature for copper. It seems therefore that the cooling is sufficient for the anode block. For cathode moderate (300 W) to high cathode power, one can get a total thermionic emission > 1 A which is what is typically within the thermionic range for arc discharges. However, if the power distribution ends up being smaller, then the PIG source will be unable to get to a thermionic state.

It was observed experimentally that the Penning ion source could indeed get ignited to a thermionic hot cathode mode for neck thicknesses of even 4 mm if the gas flow is high enough (about 20 sccm). The ion source can still operate because there are enough gas particles to ionize and generate the large currents necessary to ignite the plasma. However, since most ion sources with helium operate closer to 5 sccm [15], it was necessary to thin the cathode to about 0.9 mm thickness. This allows the cathode to stay hot even at lower gas temperatures, where there

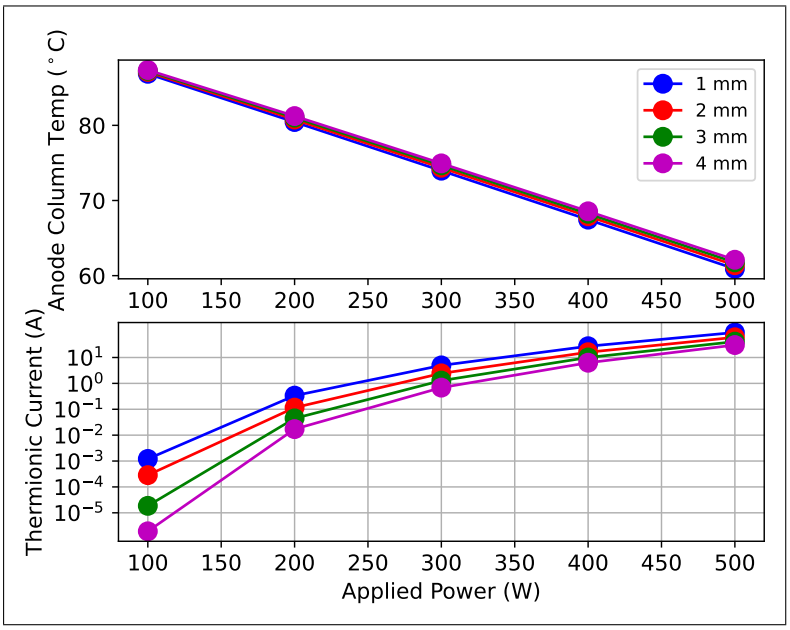

Figure 3.23: For a set simulated power of 1 kW total, the average anode column temperature and total thermionic cathode current is shown as a function of the portion of power on the cathode. This is shown for a few different cathode neck thicknesses.

are smaller ion currents heating the cathode due to less gas to ionize in the bulk plasma.

3.5.5 Materials

Materials were chosen to be vacuum compatible, which means they have low outgassing, and non-magnetic to retain uniformity of the magnetic field from the C-magnet. The anode, cathode cooling block, and cooling tubes were made of copper due to its high thermal conductivity and electrical conductivity. The bracket and HV flange was made of aluminum due to low cost, electrical conductivity, and mechanical stability. The anode plate (with the extraction slit) and puller were made of molybdenum due to its high melting point (can take higher power loads from beam), mid-range thermal conductivity and good electrical conductivity. The

electrical insulators were made of Shapal™ Hi-M soft, an aluminum nitride based machinable ceramic which is also a medium-range thermal conductor. This means that it will help spread the cooling between the different electrodes. The HV insulator was made of PTFE as it's a low-outgassing plastic.

Chapter 4

Plasma Diagnostics

4.1 Langmuir Probe

One of the most popular methods for the determination of plasma parameters is the Langmuir probe. This is simply a metal probe inserted into the plasma, which is biased to some potential V_B with respect to the grounded plasma chamber. V_B is swept through a range of voltages in order to get the current drawn on probe. This I vs V_B curve is then used to extract the electron density, plasma potential, and electron temperature. In order to avoid large perturbations of the plasma, the dimension of the probe should be much smaller than the dimensions of the chamber.

The plasma at the probe location has some plasma potential V_p with respect to the chamber walls. When $V_B = V_p$, the lack of potential difference means the probe is getting current mostly from the high speed electrons. As V_B is increased, the probe will start to draw more electrons until an electron saturation current is reached. When $V_B < V_p$, electrons will start to get repelled until V_B reaches the floating potential V_f. This is when the voltage is low enough to repel most of the mobile electrons and attract the less mobile ions so that the two drawn currents are equal, resulting in a net current of 0 A on the probe. At $V_B < V_f$, more electrons are repelled until we get to the ion saturation current where only ions are attracted.

Let us consider a probe with some area A which is large enough so that the plasma sheath thickness about the probe does not significantly influence the area.

When V_B is sufficiently small, the ion saturation current than becomes:

$$I_{sat} = en_s u_B A \tag{4.1}$$

where n_s is the ion density at the sheath edge, and u_B is the Bohm velocity (2.25). Now as V_B gets larger (but $V_B < V_p$), we start to have more electron collection on the probe area. The flux on the wall is proportional to the electron density n_e, the root mean-square of the electron velocity $\bar{v_e}$, and the probe surface area A. The electron density is assumed to follow the Boltzmann relation (equation 2.19), which adds an exponential term relating the probe's sheath potential and the electron temperature. In addition, there is also the ion saturation current, so in total the current on the probe is [22]:

$$I = I_{sat} + \frac{1}{4} A n_e \bar{v_e} = I_{sat} + eAn_e \sqrt{\frac{eT_e}{2\pi m_e}} e^{\frac{V_B - V_p}{T_e}} \tag{4.2}$$

Figure 4.1 shows an example of a bias voltage (V_B) versus current (I) plot along with a fit from equation 4.2. Also shown is the location of the floating potential (V_f) and plasma potential (V_p). The plasma potential is approximated by finding where the derivative of the exponential rise of probe current with respect to V_B potential is at maximum.

4.1.1 Non-Maxwellian Distributions

In many ion sources, large electric fields accelerate electrons to high energies, and these electrons then lose energy through collisions within their mean free path length. This is the case in Penning ion sources, where electrons are typically accelerated across the cathode sheath and essentially become a beam of electrons penetrating into the plasma. Due to the relatively low pressures and high voltages of these ion sources, an electron might not lose most of their energy before other high-energy electrons are introduced to the plasma body. This creates a higher energy 'tail' to a normally Maxwellian distribution. These hot electrons mostly lose energy due to inelastic collisions with the background neutral particles, as Coulomb collisions which lead to Maxwellian distributions among the electrons only dominate at low electron energies.

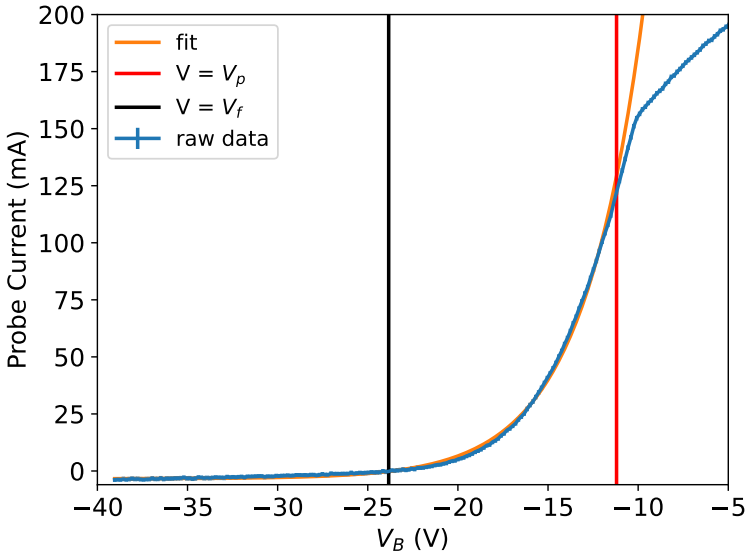

Figure 4.1: Example Langmuir probe curve with a fit for the Maxwellian EEDF case (eq. 4.1). Also shown are the location of V_p, which is found by finding the maximum of the first derivative, and V_f where I = 0 respectively.

This leads to what is often referred to as 'two-temperature' distributions, which separates the EEDF into a portion of hot and cold electrons. These are also often anisotropic, as shown in section 5.3.3. In theory of course, there are an almost infinite amount of EEDFs that are possible, and solving for the EEDF for a particular discharge requires solving a set of kinetic equations for the electrons which solves for the distribution as a function of position and velocity space. This can get very complicated and computationally intensive, and so usually rough approximations of what the EEDF might look like are used.

Two primary examples used by plasma physicists to represent hot electrons are the bi-Maxwellian [30, 31] and flat [32, 33] distribution. The bi-Maxwellian distribution can be represented by:

$$f(E) = A_e\sqrt{E}\beta e^{-E/T_e} + A_h\sqrt{E}(1-\beta)e^{-E/T_h} \tag{4.3}$$

where A is a normalization constant for each Maxwellian so that its integral over energy is 1, T_e the electron temperature for the colder electrons, T_h the temperature for the hot electrons, and $\beta \leq 1$ the portion of electrons in the colder Maxwellian distribution. The flat distribution is essentially just a uniform distribution from electron energy $0 \rightarrow V_{arc}$ where V_{arc} is the arc voltage of the ion source [34]. Thus the equation for this EEDF is:

$$f(E) = \beta f_{max}(E) + (1-\beta) f_{flat}(E) \tag{4.4}$$

$$f_{flat}(E) = \frac{1}{V_{arc}} \text{ for } E < V_{arc} \tag{4.5}$$

In order to use these non-Maxwellian EEDFs with the Langmuir probe, one has to find the average velocity of the electrons in the distribution which are capable of overcoming the voltage barrier provided by the probe. By mulitplying this by the surface area of the probe, one then finds [22]:

$$I_e = \frac{2\pi e^3}{m^2} A \int_{V_p - V_B}^{\infty} E \left[\left(1 - \frac{V_p - V_B}{E} \right) \right] f(E) dE \tag{4.6}$$

and so the current on the probe becomes $I_{sat} + I_e$. For either a flat or bi-Maxwellian EEDF, the current on the probe is then the current for a Maxwellian EEDF probe (equation 4.2) in addition to the derived current for the additional EEDF from equation 4.6. The derived current for a flat distribution is:

$$I_{flat} = \frac{n_e A e^{3/2}}{2^{3/2}\sqrt{m_e}} \left(\frac{2}{3}\sqrt{V_{arc}} - 2(V_p - V_B) V_{arc}^{-1/2} + \frac{4}{3}(V_p - V_B)^{3/2} V_{arc}^{-1} \right) \tag{4.7}$$

and thus the equation that is fit for the Maxwellian + flat distribution for a Langmuir probe measurement is:

$$I = I_{sat} + \beta e A n_e \sqrt{\frac{eT_e}{2\pi m_e}} e^{\frac{V_B - V_p}{T_e}} + (1-\beta) I_{flat} \tag{4.8}$$

which therefore solves for n_e, T_e, and β.

4.2 Optical Emission Spectroscopy

Optical Emission Spectroscopy (OES) is a widely used tool in plasma diagnostics primarily because it is non-invasive, unlike the Langmuir probe. It is based on using the radiative properties of the atoms, molecules, and ions inside the plasma to give information about the plasma's properties. It's also relatively easy to obtain a useful spectrum as many atoms/molecules have radiative transitions in the visible light range, which is a spectrum that is very commonly measured with commercially available detectors. Another advantage over other techniques is that it's generally not affected by the magnetic and electric fields within a plasma (to some limit). The disadvantage though is a greater difficulty in data analysis since one has to interpret the plasma parameters from an indirect measurement.

Due to the wide availability of measurement tools in the visible range, most OES diagnostics will use this part of the electromagnetic spectrum, and that is what will be done in this thesis. However, it should be noted that spectroscopy can also be done in the UV and infrared spectrum as well.

4.2.1 Optical Emission

When an excited state undergoes radiative transition, it releases a photon with wavelength:

$$\lambda_{ki} = \frac{hc}{E_k - E_i} \tag{4.9}$$

where E_k and E_i are the energy levels of the upper and lower excited states. The emitted intensity of the light from some density of excited states n_k along some path way ds is [35]:

$$I_{ki} = \frac{1}{4\pi} \int n_k A_{ki} h\nu_{ki} ds \tag{4.10}$$

The detector used to measure this intensity is normally a spectrometer, which is capable of recording input intensity as a function of wavelength. Spectral radiation is not typically at the exact wavelength corresponding to the transition energy between states, as there will always be some sort of broadening mechanism. The dominant source of broadening in laboratory plasmas is usually Doppler broad-

ening [36, 37], which is the broadening of the resonant wavelength λ_0 due to the thermal velocity of the excited particle with respect to the observer:

$$\Delta\lambda = 2\sqrt{ln2}\lambda_0\sqrt{\frac{2kT_g}{Mc^2}} \tag{4.11}$$

This means that the total intensity of the line has to be integrated over the broadened wavelength about the spectral line, which is usually Gaussian for a Doppler shifted line.

What information can be acquired from a spectrum depends on the type of spectroscopic calibration that has been done. One can have either a relative or absolutely calibrated system. In an absolutely calibrated system, one can directly convert the measured signal from the spectrometer to the intensity (W/m^2 sr) of the light shining onto the CCD array within the spectrometer. However, this can be rather complicated as one then needs to calculate all the losses in intensity due to the various mediums and geometries light must pass through to get from the plasma to the spectrometer. The advantage though is that a measurement of intensity with an absolutely calibrated spectrometer leads to a direct measurement of the population density since intensity is proportional to the excited state population density (equation 4.10).

Relative calibrations are usually simpler as one only needs to calibrate the optical system using a source with known spectral shape over the range of usable wavelengths. This takes away the direct measurement of intensity and therefore population density. However, one can find the population density ratios by the ratio of intensities, following from equation 4.10:

$$\frac{I_{ki}}{I_{pq}} = \frac{n_k A_{ki} h\nu_{ki}}{n_p A_{pq} h\nu_{pq}} \tag{4.12}$$

for some upper states n_k and n_p which transition to n_i and n_q respectively. So if one has a model that can solve for plasma parameters as a function of these population density ratios (and therefore intensity ratios), then the spectrum can be used to estimate the plasma parameters.

4.3 Spectroscopy 0-D Models

In order to use the intensity ratios for a particular plasma, one needs a model which can give the ratios of population densities of the emitting excited states. The types of models which are used are described below.

4.3.1 Corona and Equilibrium Models

The simplest case for 0-D modeling of population densities of particle states in some volume is using the Boltzmann distribution, where the probability of being in each state is proportional to $\exp(-\frac{\varepsilon}{T_e})$. This approximation is valid when all particles are in thermal equilibrium. However, this is not the case for many low-pressure laboratory plasmas, where the electron temperatures are much higher than the heavy particle temperatures.

A common model used for non-equilibrium plasmas typical of laboratory plasmas ($T_e > T_i \geq T_g$) is the corona model. This is often used when the electron density is low enough so that electron impact de-excitation has much lower rates than spontaneous emission. An additional condition for the corona model is when the plasma is primarily ionizing, which means the rate of recombination of ions and electrons is small with respect to the ionization rate. The final condition is generally a low degree of ionization, so that most upward transitions are from the ground state due to the much larger population compared to excited states. This model is often used for low temperature plasmas as they generally fit this condition.

However, in the case of Penning ion sources, the power density ($\frac{W}{cm^3}$) is usually high, which results in much higher electron densities (up to 10^{19} m^{-3} [10]) relative to typical corona conditions. This starts to get a bit outside the jurisdiction of a corona model, and a more general model should be used which encompasses the important chemistry within the plasma.

4.3.2 Collisional-Radiative Model

A general method for getting the population densities of a plasma is to have a system of equations for each important transition process between all particles of interest. Each excited state population density n_k has a rate of change described by:

$$\frac{dn_k}{dt} = \sum_{i<k} n_i n_e K_{ik}^{exc} - n_k \left[n_e \left(\sum_{i<k} K_{ki}^{de} + \sum_{i>k} K_{ki}^{exc} + K_k^{ion} \right) + \sum_{i<k} A_{ki} \right] + n_k \nu_w + n_i \sum_{i>k} \left(n_e K_{ik}^{de} + A_{ik} \right) \quad (4.13)$$

where index i represents other particle states. K_{ik}^{exc} is the rate constant for excitation from n_i to n_k, K_{ki}^{de} is the rate constant for de-excitation from n_k to n_i, K_k^{ion} is the rate constant for ionization from n_k to the singly ionized state, and ν_w is the neutral diffusion rate for particles hitting the wall. This is the basis of a Collisional-Radiative (CR) model, which solves for the populations of various particles by including various interactions between the particles in 0-D. Equation 4.13 contains those interactions important for the plasmas mentioned in this thesis, though CR models can also include various other interactions such as radiation field interactions, ion-electron recombination, non-electron impact ionizations, etc.

One should notice that the assumption of negligible ion recombination made within the corona discharge is continued here, since for laboratory discharges with $T_e > 2$ eV and $n_e < 10^{20}$ m^{-3}, the recombination rate is orders of magnitude less than the ionization rate. In addition, the high current density of Penning ion sources means most charged particles are lost on the chamber walls rather than through recombination.

The interactions for each species are therefore electron impact excitation and de-excitation, ionization, spontaneous emission, and diffusion to the walls. The diffusion to the walls is important for metastable states, since they will generally hit the wall and revert to the ground state before undergoing spontaneous emission. Notice another common assumption is used where the most important reactions are due to electron impacts, rather than energy exchange with other atomic species, which is due to the much higher electron temperature found in ion sources.

The reaction rate for each electron impact reaction, as defined by equation 2.3, is the average of the cross section and electron speed for the particular reaction. In order to get this average, one must integrate over all the possible speeds of the electrons within the plasma. This is where the EEDF comes in, since one can then

integrate $\sigma(E)v_e(E)$ over the entire energy range of the electrons to get the rate coefficient:

$$K = \int_0^\infty \sigma(E)\sqrt{\frac{2E}{m}} f(E) dE \tag{4.14}$$

where E is the electron energy and $v_e = \sqrt{\frac{2E}{m}}$ as electrons are non-relativistic. The cross sections for these interactions have to be found on databases which usually have values given by either experimental results or theoretical models. For such a model, it is important to have cross sections with some accuracy, though it can be common to have cross sections with relative uncertainties greater than 100%. Spontaneous transition probabilities tend to be more readily available on online databases due to a large collection of experimental results, though theoretical values are still sometimes used.

The diffusion of neutrals is important mostly for the metastable states, as it is the main driver of transitions to the ground state. A simplified way to estimate this is described by Möller [38]. The diffusion of a particle in a chamber full of similar particles is:

$$D_n = \frac{3\sqrt{\pi}}{8} \frac{1}{n_g \sigma_n} \sqrt{\frac{k_B T_g}{M}} \tag{4.15}$$

where σ_n is the inter-collisional cross section for the neutral particle, and M the particle mass. The confinement time in a plasma chamber is:

$$\tau_D = \frac{L_D^2}{D_n} \tag{4.16}$$

where L_D is the mean diffusion length given for a cylindrical geometry as:

$$L_D = \left(\frac{8}{R^2} + \frac{12}{L^2} \right)^{-1/2} \tag{4.17}$$

with R the radius of the chamber and L the length. There is also the potential for a particle go to the wall without collision, in which its confinement time is:

$$\tau_f = \frac{L_f}{v_{th}} \tag{4.18}$$

where $L_f = \frac{2V}{A}$ (V = volume and A = surface area) is the average free fall length to the wall, and $v_{th} = \sqrt{\frac{8k_BT_g}{\pi M}}$ the thermal velocity of the particles. The wall collision rate is then approximated by:

$$\nu_w = (\tau_D + \tau_f)^{-1} \tag{4.19}$$

4.4 Helium CR Code

There are a few examples of helium CR models being used for low pressure laboratory plasmas [39–44] and for outer regions of fusion plasmas [45–48]. Most of these are based on one or two codes produced by labs in Japan and Europe. There is a CR model for helium that is open to use by researchers around the world called Yacora on the Web [49].

4.4.1 Yacora on the Web

Yacora on the Web is developed by a team of physicists at the Max Planck Institute for Plasma Physics at Garching (otherwise known as IPP). They provide collisional radiative models for H, H_2, and He models for use by scientists around the world. The model of interest here is the He model. This code uses the same equations and interactions described in the previous section for helium with all LS excited states up to n = 4. The diagram for the helium states used is shown in figure 4.2. The states are generally divided up by their multiplicity, which are the singlet states for multiplicity 1 and triplet for 3. The reason for this division is due to the rules for dipole transition ($\Delta S = 0$), which means the strongest radiative transitions will be within either the singlet or triplet states.

However, preliminary studies using this code showed ratios that implied electron temperatures and densities about an order of magnitude higher than expected for the plasmas studied in this thesis. This could be because the code doesn't include radiation trapping, which has been shown to be important in many studies of helium plasmas [39, 40, 42–44, 47, 48]. Another reason could be due to the common assumption of a Maxwellian EEDF, whereas in low pressure ion sources higher energy electrons might have a significant impact on the excited population

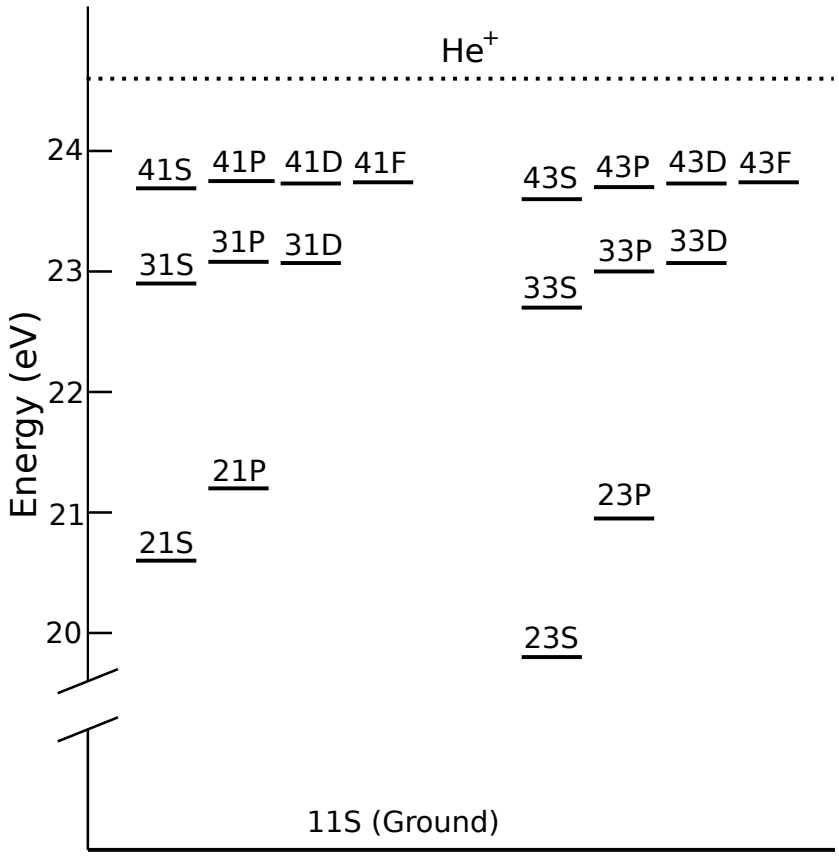

Figure 4.2: Helium energy levels for LS designated states used in Yacora on the Web and the CR-model within this thesis.

levels. Other less likely reasons could be due to the inclusion of only allowed dipole transitions and the neglect of LS states with $n > 4$. All these reasons lead to the author creating their own CR model applied to helium plasmas.

4.4.2 Core Model

The model was built in Python [50] due to its ease of use, the enormous amount of online resources available for it, the author's own familiarity with it, and the most important reason of all for a graduate student: it's free. The primary drawback compared to some other languages is it's slower computational speed, as it's an

interpreted language. The best way to minimize this disadvantage is to use specialized packages like numpy and SciPy [51], which use functions implemented in C code for increased speed on array multiplications.

The basis of the model is the rate equation given by equation 4.13. Solving for the populations n_k for n = 0 $\rightarrow$ 4 means one solves for the rate of change for 19 helium population levels. As this equation is linear, it can be represented by a system of linear equations:

$$\frac{d\mathbf{n}}{dt} = \mathbf{R}\mathbf{n} \tag{4.20}$$

where $\mathbf{R}$ is the rate matrix which is a combination of all the interactions which lead to transitions between particle states, and $\mathbf{n}$ is the column vector representing the population density of each state in order of increasing energy. So in an array starting at index 0, n_0 is the ground state (1^1S), n_1 is the 2^3S state, and so on. The states and their properties are shown in table 4.1. We assume that the plasma we are observing is at a quasi-steady state condition so that the population levels are constant in time $\frac{d\mathbf{n}}{dt} = 0$.

The rate matrix is composed of several rate matrices representing each transition. So $\mathbf{R} = \mathbf{R}_{exc} + \mathbf{R}_{de} + \mathbf{R}_{trans} + \mathbf{R}_w$ which represent respectively the electron impact excitation (including ionization), electron impact de-excitation, spontaneous emission, and wall diffusion rates for each particle species. Reactions that are neglected in the CR model include: ion-electron recombination, collisions between atoms, and complex atom-on-surface interactions. The electron impact rates for some transitions from n_i to n_k is given by:

$$R_{ik} = n_e K_{ik} = n_e \int_0^\infty \sigma_{ik}(E) \sqrt{\frac{2E}{m}} f(E) dE \tag{4.21}$$

In order to get the electron impact rates, one needs the electron density n_e and the EEDF $f(E)$. An example of the general matrix for a set of excited states which goes up to index k is shown in equation 4.22 for row element i and column element j. The lower diagonal represents rates which lead to an increase in population density due to excitations from lower energy states. The upper diagonal is 0 as higher energy level states do not excite to a lower states, and the diagonal is the loss rate of a state due to excitations of that state to higher energy levels.

Index	Term	Energy Level (eV)	g
0	1^1S	0	1
1	2^3S	19.820	3
2	2^1S	20.616	1
3	2^3P	20.964	9
4	2^1P	21.218	3
5	3^3S	22.718	3
6	3^1S	22.920	1
7	3^3P	23.007	9
8	3^3D	23.074	15
9	3^1D	23.074	5
10	3^1P	23.087	3
11	4^3S	23.594	3
12	4^1S	23.674	1
13	4^3P	23.708	9
14	4^3D	23.736	15
15	4^1D	23.736	5
16	4^3F	23.737	21
17	4^1F	23.737	7
18	4^1P	23.742	3

Table 4.1: Index of each term in population column vector, along with its LS term, energy level (only up to three decimal places), and statistical weight g

$$\mathbf{R}_{exc} = \begin{pmatrix} -\sum_{m=1}^{k} R_{0m} & 0 & . & . & . & . & . & 0 \\ R_{01} & -\sum_{m=2}^{k} R_{1m} & 0 & . & . & . & . & 0 \\ R_{02} & R_{12} & -\sum_{m=3}^{k} R_{2m} & 0 & . & . & . & 0 \\ . & . & & . & & & & \\ . & . & & & . & & & \\ . & . & & & & . & & \\ . & . & & & & & . & \\ R_{ji} & R_{ji} & & & & & & -\sum_{m=j+1}^{k} R_{im} \end{pmatrix} \tag{4.22}$$

Another commonly made assumption for plasmas is that of quasi-neutrality, where the electron density is roughly equal to the total ion density. For an ion source plasma, in order to retain this quasi-neutrality at a set n_e, every ion introduced to the volume due to ionization of one of the helium states must be neutralized somehow. This is interpreted as the ions lost to the wall, which are immediately neutralized to a ground state helium atom. As a result, the ionization loss terms in the excitation matrix are introduced in the summation of terms along the matrix diagonal, which results in a gain of ground state atoms in the first row of $\mathbf{R}_{exc}$. For laboratory plasmas, we expect the amount of He^{+} to be much greater than that of α-particles (also known as He^{2+}). For this reason, the population of α-particles is ignored. Though this population is of interest, its introduction would introduce the need for estimated diffusion losses for the ions, which is not well known due to the lack of information of anomalous diffusion losses.

The opposite reaction to excitation is the de-excitation collision. This is when an atom/molecule releases energy to a colliding electron, which allows it to transition to a lower energy state. The cross-section for transition with change of energy ΔE is found using the principle of detailed balance in a steady-state plasma [24]:

$$\sigma_{de}(E) = \frac{g_i}{g_k}\frac{E+\Delta E}{E}\sigma_{ex}(E+\Delta E) \tag{4.23}$$

The same procedure is used for filling $\mathbf{R}_{de}$ as $\mathbf{R}_{exc}$, except with the upper diagonal being filled and the lower diagonal set to 0 due to it being the inverse reaction.

Getting accurate cross sections is one of the most important parts of making these 0-D spectroscopy models. Luckily, there is a convenient paper which gives fit equations for electron impact excitation and ionization of the LS helium states up to n = 4 authored by Yuri Ralchenko et al [52]. These are based on available experimental cross sections and results from theoretical calculations. According to the paper, the general estimated accuracy for transitions from the ground state are 10-30% for $\Delta S = 0$ transitions but $\geq 30\%$ for $\Delta S \neq 0$. For other transitions between excited states, the conservative estimate is about 50%.

The $\mathbf{R}_{trans}$ matrix is also filled out in a similar way, by having the sum of all spontaneous emission probabilities for an upper excited state as the loss term in the diagonal, and the emission probabilities for the gain terms of the lower excited states in the upper diagonal.

Finally, $\mathbf{R}_w$ is done similarly to the ionization addition to $\mathbf{R}_{exc}$, where the diagonal represents the loss rates of each particle, which then becomes a positive rate to the ground state in the first row.

The last step then is to multiply equation 4.20 by the inverse of $\mathbf{R}$ to solve for $\mathbf{n}$. However, one may realize that the sum of all rows for $\mathbf{R}$ is 0. This means that several solutions exist (including the trivial $\mathbf{n} = 0$), and an additional constraint needs to be applied. In this case, it's assumed that the sum of all helium particles is equal to to the neutral gas density calculated in the ion source subtracted by the ion density. With the additional assumption that the ion density is equal to the electron density, this leaves us with the equation:

$$n_n - n_e = \sum_k n_k \tag{4.24}$$

where n_k is each neutral helium atom solved for within the CR Model. This equation can replace one of the population rates of equation 4.13 (or one of the rows of matrix $\mathbf{R}$) in order to obtain a unique solution when solving for $\mathbf{n}$. This is solved for an entire set of $1 < T_e < 20$ and $10^{16} < n_e < 10^{19}$ which is the estimated range for laboratory plasmas at the pressures we're observing. For each set of [T_e, n_e], one can then solve for the expected intensity ratios.

In order to solve for the set of plasma parameters [T_e, n_e], we find which set of parameters minimize the error function [31, 44, 48, 53]:

$$err = \sqrt{\sum_i \left(\frac{\kappa_i^{exp} - \kappa_i^{CR}}{\kappa_i^{exp}} \right)^2} \tag{4.25}$$

where κ_i^{exp} is a ratio of line intensities found experimentally, and κ_i^{CR} is the theoretical ratio of line intensities found from the CR model.

In order to further optimize the code for speed, the minimum of err is solved for using a sparse grid (about 50 elements) of possible plasma parameters [T_e, n_e] with a large range of expected values. This minimization solves for the new optimized point (p) in parameter space, which is then used to form a new grid of 50 elements. This new grid has mean spacing Δp with a range of $p - 5\Delta p < p < p + 5\Delta p$ for each parameter. This process is repeated until $\frac{\Delta p}{p} < 0.0001$ for each plasma parameter.

4.4.3 Absorption and Radiation Trapping

The opposite reaction to spontaneous emission is radiative absorption, in which the lower state absorbs a photon at the required frequency to transition to the upper state. In a plasma, it is generally assumed that the source of these absorbed photons are from spontaneous emission of the upper excited states to the lower excited state. If all the spectral lines were irradiated at their exact frequencies (which match the transition energy between states), then the lower states around it would re-absorb it immediately. However, due to the thermal velocities of the neutral particles, the spectral lines will undergo a Doppler shift, which will broaden the line so that it is not emitted at the exact frequency required for re-absorption. This can be described by the absorption coefficient at the line center [31, 36, 41, 54]:

$$k_0 = n_i \frac{g_k}{g_i} \frac{\lambda^3}{8\pi} A_{ki} \sqrt{\frac{M}{2\pi T_g k_B}} \tag{4.26}$$

with M the particle mass, T_g the gas temperature, g_k and g_i the statistical weights for the upper and lower state respectively, and λ the wavelength of the spectral line. The optical depth is defined as $\tau = k_0 l_{rad}$, with l_{rad} being the characteristic

radiation length in the plasma. This defines how much absorption is happening for a certain spectral line in the plasma. For $\tau >> 1$ we have an optically thick plasma where a significant portion of radiative emissions are re-absorbed, and for $\tau << 1$ we have an optically thin plasma where all spectral radiation escapes the plasma volume.

In optically thick plasmas, the spontaneous transition probability will effectively be reduced because some of the escaped radiation will be absorbed by the lower state. The portion of radiation that escapes the plasma volume is represented by an optical escape factor (OEF) symbolized by Θ_{ki}. This results in a reduced transition probability:

$$A'_{ki} = \Theta_{ki} A_{ki} < A_{ki} \tag{4.27}$$

Finding the OEF can be quite difficult as one needs to integrate the Beer-Lambert's law for all emitted particles over the entire volume. Not only does this require additional computation, but one technically needs to know the density profile for all states which take part in light emission and absorption within the plasma.

Often for the sake of simplicity, physicists make a basic assumption of the neutral density profile and the location within a plasma volume that the primary source of light is coming from. One particular OEF (for Doppler broadened radiation) used for cylindrical plasma chambers and assuming the spatial distribution of the helium neutral particles is parabolic with population density which goes to 0 at the edge of the cylinder is [41, 42, 45]:

$$\Theta_{ki}(\tau) = \frac{1.92 - \frac{1.3}{1+\tau^{6/5}}}{(\tau + 0.62)(\pi ln(1.375+\tau))^{1/2}} \tag{4.28}$$

This equation is widely used within the field of plasma spectroscopy as many experiments observe plasmas from an optical port looking radially into a cylindrical body. While this is certainly the case for the Penning ion source, we'll find in this thesis a case where we must observe the light from a cylindrical plasma along its longitudinal axis. In this case, another popular form of the OEF factor is [55]:

$$\Theta_{ki}(\tau) = \frac{2}{\sqrt{\pi}} \int_0^\infty dx \int_0^1 dt \exp\left(-x^2 - \frac{\tau}{t}\exp(-x^2)\right) \tag{4.29}$$

which is the OEF factor from the center of a plasma between two parallel planes of distance L, and τ is the optical depth at $l_{rad} = \text{L}/2$. This is similar to the most common OEF factor which comes from the emission within the center of a spherical plasma [55]:

$$\Theta_{ki}(\tau) = \frac{2}{\sqrt{\pi}} \int_0^\infty dx \exp\left(-x^2 - \tau \exp(-x^2)\right) \tag{4.30}$$

where l_{rad} corresponds to the radius of the sphere.

Radiation Trapping and EEDF variations

Introducing radiation trapping in $\mathbf{R}_{trans}$ is done by multiplying each transition by its OEF. Generally, the assumption is that the ground state is the dominant population, so it is estimated that $n_g \approx n_n$ where n_n is the sum of all helium particles regardless of state. This allows for an easier calculation of equation 4.26 which then becomes independent of the individual populations and therefore doesn't introduce non-linear terms into the equation. However, if metastable state populations get significant, one can then introduce an iteration scheme. In this case, one can then solve for the case with just the ground state, use the result to solve for the OEF for each line with a ground or metastable lower state, and then repeat until convergence.

Figure 4.3 shows a simplified flow chart which represents the steps for estimating the plasma parameters from measured intensity ratios using the NSCR model when assuming a Maxwellian EEDF. We see that the OEF calculation is an intermediary step in constructing the spontaneous emission rates, which is part of the total rate matrix. We also see how iterations are introduced to the OEF if we add absorption from metastable states.

Non-Maxwellian EEDF variations, such as the bi-Maxwellian and flat distribution, can also be computed. These introduce parameters β and/or T_h, increasing the computation time significantly assuming good resolution in the electron energy axis for numerical integration of each rate constant. Consequently, a fit for each rate constant K_{ik} as a function of either T_e for Maxwellian distributions or V_{arc} for the flat distribution is computed before the primary computations. This allows for much faster retrieval of each K_{ik} needed to form the rate matrices for electron im-

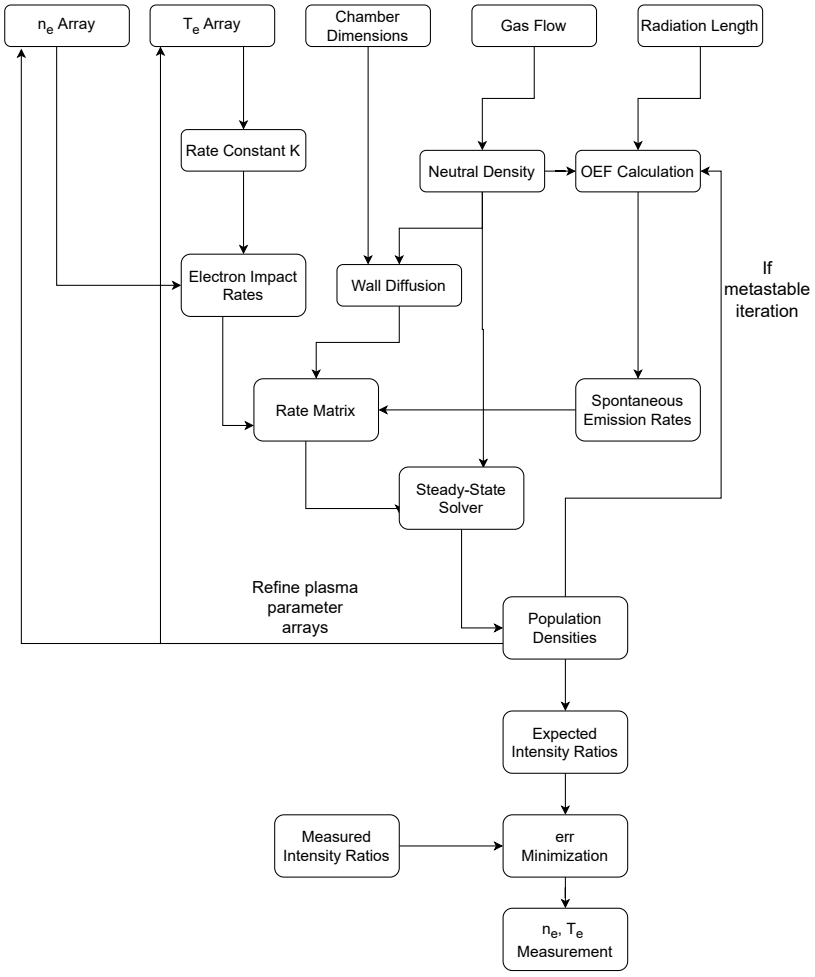

Figure 4.3: Simplified flow chart for calculating the plasma parameters from an OES measurement when assuming a Maxwellian EEDF.

pact reactions. In addition, this allows for a better resolution in parameter space due to the reduced computational speed.

4.4.4 Yacora Comparison

To determine at first the validity of the model, one must compare to a model that is already established within the scientific community. In this case, Yacora on

the Web is a natural choice as the self-made CR model is already based on the model itself. Yacora on the Web is generally solved by keeping the ground state population n_g constant as the final constraint rather than the total sum as done in this thesis (equation 4.24). For the sake of comparison, the CR model is varied to use the same constraint in this particular case. However it should be mentioned that there is little difference between the results for either constraint. The EEDF is Maxwellian and no radiation trapping is included just as in Yacora on the Web. For both, the population levels of the excited states are solved using combinations of $n_g = [10^{20} \rightarrow 10^{21}]$ m^{-3}, $n_e = [10^{16} \rightarrow 10^{18}]$ m^{-3}, and $T_e = [1 \rightarrow 20]$ eV. Each set has size of 25 with the numbers equally spaced in their logarithmic values for the number densities, and linearly for T_e. We assume a constant gas temperature of $T_g = 1000$ K to test the upper limits of gas temperature. For simplicity of labeling, the CR model from this thesis will be referred to as the NSCR (Nicolas Savard Collisional Radiative) model. The author is aware of his lack of creativity.

From most papers on the subject found in scientific journals, many who use CR models with helium [40, 43–48] will measure two line intensity ratios to find the electron's Maxwellian temperature and density: 728.14 nm over 706.54 nm (I_{728}/I_{706}) normally used due to greater dependence on T_e and 667.82 nm over 728.14 nm (I_{667}/I_{728}) used due to greater dependence on n_e. Figure 4.4 shows I_{728}/I_{706} for both models at $n_g = 3\times10^{20}$ m^{-3}. We see that the ratios as a function of n_e and T_e are very similar and the trends are the same. The percent difference for both ratios between the NSCR and Yacora model, with the Yacora model as the primary reference, are shown in figure 4.5. We see that the percent difference is overall within 10% within the primary region expected for laboratory plasmas. If we take the absolute difference as a variable ($\frac{|I_{NSCR}-I_{yacora}|}{I_{yacora}}$), then the average and deviation for this variable for the calculated values of n_e and T_e is 5.7% and 2.9% respectively for I_{728}/I_{706}, with 2.5% and 1.5% respectively for I_{667}/I_{728}. Considering the possible differences in the models due to floating point numbers, differences in cross sections for electron impact collisions and radiative probabilities for similar radiative lines, the inclusion of forbidden transitions, and the integration methods over the Maxwellian distribution, these differences do not represent a significant difference in parameter determination for OES diagnostics. Thus the NSCR model matches well with the Yacora model.

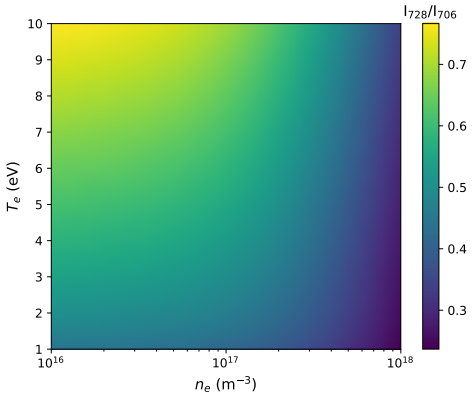

(a) NSCR

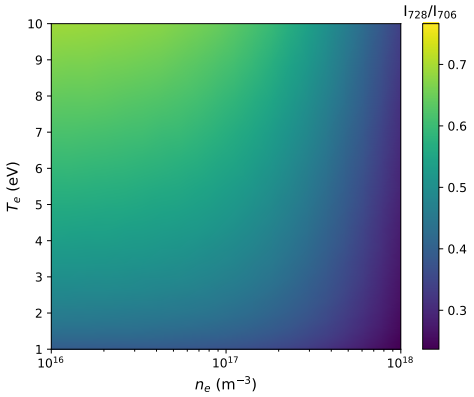

(b) Yacora on the Web

Figure 4.4: Ratio of intensities of 728 nm and 706 nm line for the (a) NSCR model and (b) Yacora on the Web.

4.4.5 Effects of Radiation Trapping

Radiation trapping has a significant effect on the output line intensity ratios due to the increase in the n^1P excited state populations from photon absorption of the ground state. Figure 4.6 shows the effect of radiation trapping for the primary line intensity ratios at typical values of n_e and T_e within the Penning ion source. This is done using the dimensions of the Penning ion source chamber (4 mm radius and 50 mm length), with the radius used as the radiation length for calculating the OEF (equation 4.28) when applying radiation trapping. The neutral gas density is taken

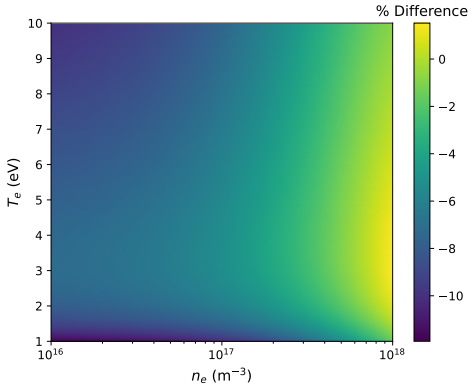

(a) I_{728}/I_{706}

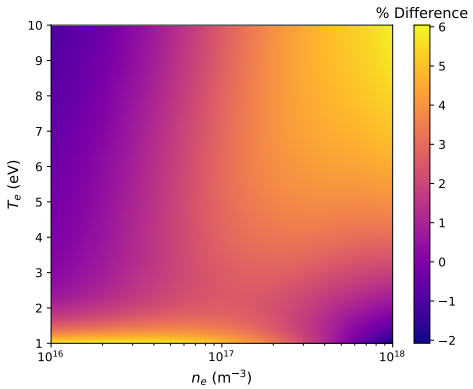

(b) I_{667}/I_{728}

Figure 4.5: Percent difference between the NSCR and Yacora model for the common intensity ratios: (a) I_{728}/I_{706} and (b) $_{667}/I_{728}$.

at 20 sccm, or 2.41×10^{21} m^{-3}.

We see from figure 4.6a that the I_{728}/I_{706} ratio is strongly dependent on T_e except when surpassing electron densities of about 10^{18} m^{-3}. Figure 4.6b shows that the I_{667}/I_{728} ratio is primarily dependent on electron density, with minor gradients along T_e. The inclusion of radiation trapping however (figure 4.6c and 4.6d) generates a significant increase in these ratios, especially in the I_{667}/I_{728} ratio where the factor increases by a factor 2 or more. This translates to a significant difference when using the NSCR for measurements of n_e and T_e with and without radiation trapping. The reader should note that this is for a small chamber with only a 4 mm

radiation length. Thus when using this model on ion sources with higher neutral densities or with larger radiation length scales, the radiation trapping leads to a further increase in the expected intensity ratios. This leads to significant disagreement with other plasma diagnostics when radiation trapping is not included, as shown in section 4.5.3.

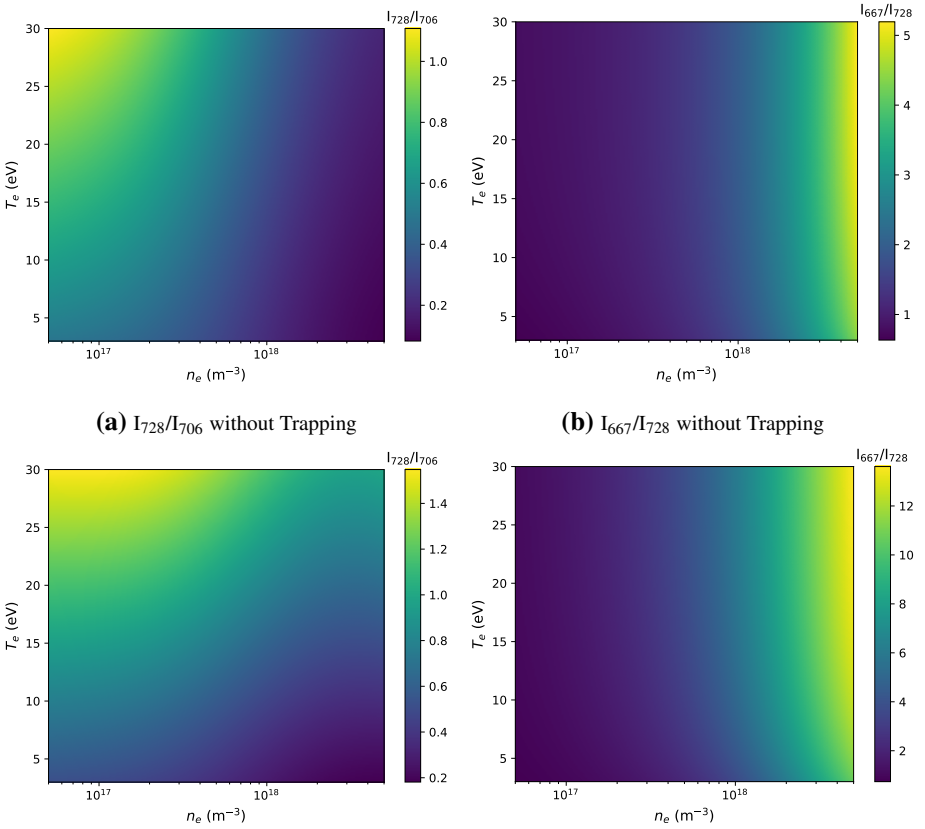

(a) I_{728}/I_{706} without Trapping

(b) I_{667}/I_{728} without Trapping

(c) I_{728}/I_{706} with Trapping

(d) I_{667}/I_{728} with Trapping

Figure 4.6: I_{728}/I_{706} and I_{667}/I_{728} ratios with (a,b) and without (c,d) radiation trapping for gas flow of 20 sccm ($n_n = 2.41 \times 10^{21}$ m^{-3}) into the Penning ion source

4.4.6 Comparison with n=10 States

In Yacora on the Web, there is a limit in the number of excited states implemented into the code due to a lack of accurate cross sections for electron-impact collisions on excited states higher than n = 4. However, it is useful to know the sensitivity of such a CR code to the amount of excited states implemented, as step-wise excitations may end up being important in helium under certain conditions.

In order to make a code which includes higher excited states, some approximations are given for excitations to higher levels from $n_i < 4$ and $n_f > 4$ in Ralchenko's paper [52], and rough approximations can be used for allowed transitions between higher states with given threshold energies and oscillator strengths [56]. Using this information, important transitions can be added up to n = 10, chosen because this is the limit of states given in the NIST database. In addition, similar to what is done by Fujimoto [42], the $L > 3$ states for $n > 4$ are grouped together as degenerate states. This increases the number of states solved for from 18 to 67, which of course increases the computation time significantly as the rate matrix for each set of [n_e, T_e] goes from size 18×18 to 67×67.

The NSCR model for states up to n=10 is solved for a Maxwellian EEDF and compared to the nominal model up to n=4. Radiation trapping from the ground state is included for typical Penning parameters with anode radius of 4 mm, a length of 50 mm, and the radiation length scale the same as the anode radius. For both, the population levels for the excited states is solved for combinations of n_g = $[6 \times 10^{20}, 6 \times 10^{21}]$ m^{-3} (estimated range in the Penning source), n_e = $[10^{16}, 10^{19}]$ m^{-3}, and T_e = [1, 25] eV. The absolute values of the percent difference for intensity ratios I_{728}/I_{706} and I_{667}/I_{728} at $n_g = 6 \times 10^{20}$ m^{-3} are shown in figure 4.7. We see in figure 4.7a that the I_{728}/I_{706} ratio has a significant difference between models at higher electron densities past 3×10^{18} m^{-3}, whereas the I_{667}/I_{728} ratio (figure 4.7b) is within 5 % which is an acceptable range thoughout. This implies that ratios with greater gradients along n_e like I_{667}/I_{728} are comparable for both models at greater electron densities, whereas T_e gradients leads to much greater changes. It should be noted that this difference between the models at higher n_e becomes worse at lower pressures, hence why the case of $n_g = 6 \times 10^{20}$ m^{-3} (the lower bound of n_g) is shown.

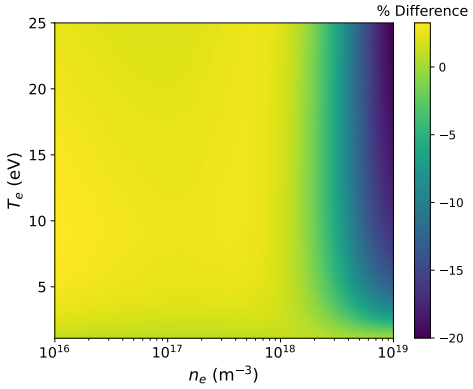

(a) I_{728}/I_{706}

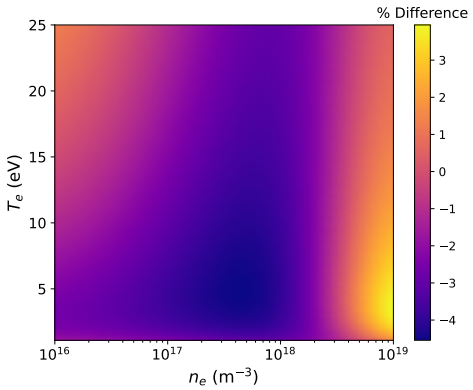

(b) I_{667}/I_{728}

Figure 4.7: Percent difference between the NSCR(n=4) and NSCR(n=10) model for the common intensity ratios: (a) I_{728}/I_{706} and (b) $_{667}/I_{728}$.

To better see this pressure dependence, figure 4.8 is what you would get if you took figure 4.7a and averaged the percent difference along the T_e axis for several different n_g values. We see that the differences between the n=4 and n=10 models after $n_e = 1 \times 10^{18}$ m^{-3} become more significant, and the rate this difference increases (in terms of absolute value) along n_e is dependent on the background gas density n_g. This is likely due to step-wise excitations, since a decrease in n_g means the plasma becomes more highly ionized at a constant n_e. Consequentially, the electron impact excitations from the ground state to the upper excited states becomes relatively less significant compared to the excitations between the different

upper excited states. Thus the n=4 case is still considered a good approximation at lower ionization fractions, which is typically the case for ion sources, but may need to be considered when operating at higher power densities within the PIG source.

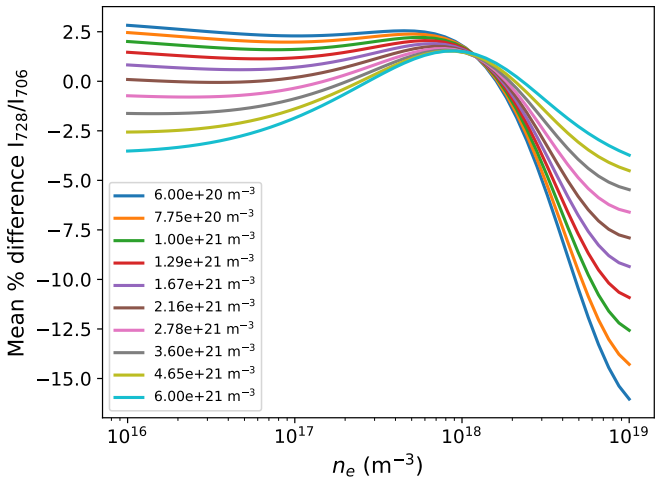

Figure 4.8: Mean percent difference between the NSCR n=4 and n=10 model along the T_e axis as a function of n_e for various n_g values. n_g values shown as different colored lines.

4.4.7 Effect of Non-Maxwellian Behavior

Many ion sources rely on high-energy electron emissions from cathodes in order to sustain a plasma. For low pressure plasmas where these electrons have large mean free paths, there might be a non-negligible contribution of these electrons to the overall EEDF within the bulk plasma, making it non-Maxwellian. It is important to note how such electrons might affect the measured line intensity ratios, as the NSCR (and most other collisional-radiative codes) assumes a Maxwellian distribution.

Equations 4.3 and 4.5 can be implemented into the NSCR model. This of course increases computation time due to the existence of extra variables. As done for the the Maxwellian EEDF, the rate coefficients for the flat component of the EEDF is solved through integration of the EEDF multiplied by the energy-

dependent cross section and electron speed. In order to decrease computation time, these rates are solved before the primary CR-model solver for a large array of V_{arc}, and then fitted to a polynomial function so that we can get the rate coefficients as a function of the V_{arc}. This means that when actually solving for the rate coefficients needed to complete the rate matrix for various V_{arc}, we can use the fit to get the rate coefficient instead of numerically integrating over a high resolution array of electron energies for each V_{arc}. Like in the case of the Maxwellian EEDF, the fit is found to be much better if we fit for the log of the rate coefficients as a function of the log of V_{arc}.

Figure 4.9 shows example plots of how much the I_{728}/I_{706} and I_{667}/I_{728} ratios increase due to the addition of higher energy electron components. In this case, we take it so that only 0.01% of the electrons are in the higher energy EEDF (so β = 0.999) to show how significant the effect can be even for small portions of high energy electrons. For the case of the flat EEDF, the upper threshold of electron energy is at V_{arc} = 500 V which is within the range of many laboratory plasmas. For the bi-Maxwellian EEDF, the hot electron temperature is set to 30 (eV), so the mean electron energy is still below most arc voltages at 100s of volts.

Figure 4.9a shows the multiplicative increase of the I_{728}/I_{706} ratio for the bi-Maxwellian case when compared to just a pure Maxwellian. In other words, the ratio of I_{728}/I_{706} with β = 0.999 and T_h = 30 eV compared to that with β = 1. We see that the I_{728}/I_{706} ratio, which has a stronger dependence on T_e, increases drastically for lower temperatures of the bulk electrons. This is because the high energy electrons create more excitations that offset the lack of excitations of the bulk electrons in this region. However, at much higher T_e the multiplicative factor tends towards 1. This is because the excitation from the bulk electrons becomes more dominant as a larger portion of the higher energy tail are greater than the excitation threshold energies. This combined with the large population of electrons in the lower temperature Maxwellian generates higher excitation rates than the higher temperature Maxwellian. This happens for the flat distribution (figure 4.9c) as well, but with the multiplicative factor going to much higher values because of the higher mean electron energy in the flat distribution.

Figure 4.9b and 4.9d shows similar plots but for the I_{667}/I_{728} ratio, which has a stronger dependence on n_e. The multiplicative factors are much lower in this case,

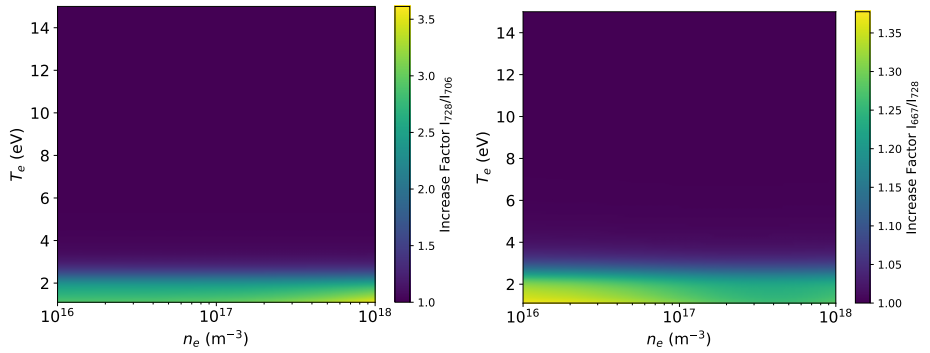

(a) I_{728}/I_{706} Bi-Max

(b) I_{667}/I_{728} Bi-Max

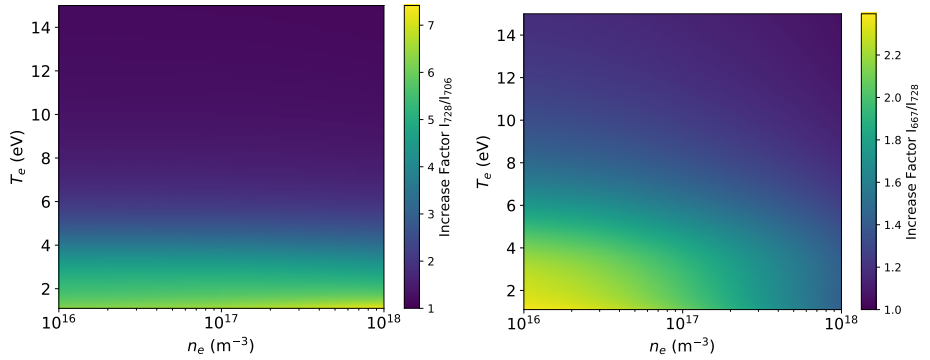

(c) I_{728}/I_{706} Flat

(d) I_{667}/I_{728} Flat

Figure 4.9: Multiplicative factor that the I_{728}/I_{706} and I_{667}/I_{728} ratios are increased by (when compared to pure Maxwellian EEDF) for a (a,b) bi-Maxwellian EEDF and (c,d) Flat plus Maxwellian EEDF. This is for a $\beta = 0.999$ for both, with $V_{arc} = 500$ V for the flat EEDF and $T_h = 30$ eV for the bi-Maxwellian EEDF

and we see that the factor remains fairly constant for specific T_e, and is thus not strongly dependent on n_e. Just like for the I_{728}/I_{706} ratio, the hotter electrons have a stronger effect when the colder electrons are at lower temperatures (< 3 eV).

The strong dependence of these ratios on the EEDF (T_e, β and V_{arc} or T_h) is not surprising, as n_e is simply a scalar value whilst the EEDF is actually a continuous function in the electron energy dimension which spans a range of 0 to V_{arc}. This means that temperature will be the more difficult parameter to estimate with the OES, which we'll find to be the case further in this chapter. It is also impor-

tant to note that as the I_{728}/I_{706} ratio has a positive correlation with T_e, these non-Maxwellian EEDF additions which increase the line intensity ratio for lower T_e means there will be multiple ways to generate a particular value of the ratio for different combinations of β and T_e. This means that the minimization procedure used to get the plasma parameters from experimental measurements will not work for non-Maxwellian EEDFs. Though not shown here, attempting to use these EEDFs experimentally with the OES diagnostic did indeed lead to multiple minimums of *err*.

4.5 Volume Cusp Ion Source Comparison

Before using the NSCR model to diagnose the Penning plasma, it is important to first verify that it is comparable to other diagnostics. The Langmuir probe (section 4.1) cannot be used on the Penning ion source due to the relatively large size of the probe compared to the ion source volume, and because the high power density within the Penning ion source would lead to over-saturation of the probe current. However, D-Pace Inc. has a TRIUMF-licensed Volume Cusp ion source used for production of H^- ions. It is a filament driven source, which means a joule-heated filament produces thermionic electron emission whilst at negative potential relative to the plasma chamber walls. Figure 4.10a shows the volume cusp field at the center of the ion source (along its length), which is observed throughout most of the plasma chamber. The field lines in the azimuthal direction (with respect to the cylindrical axis) retard electron diffusion to the walls. The strong field lines perpendicular to the chamber wall will also repel electrons via the *magnetic mirror* effect [23]. This is where some electrons with velocities perpendicular to a magnetic field are reflected if moving from weak to strong field strengths. The increased magnetic field will cause an increase in the particles rotational kinetic energy due to conservation of its magnetic moment, and thus the particle is reflected to conserve its total energy. These two mechanisms provide the electron (and partial ion) confinement. In addition there is a dipole magnetic field (called the filter field) near the aperture (figure 4.10b) used to retard electron movement toward extraction, while still allowing the heavier H^- ions to move through. The other end where the filaments are located also have a cusp field scheme (figure

4.10b) which prevents electrons from the filament being dumped directly onto the back-plate. Figure 4.10c shows the length-wise cross section. The filament is the electron emitter, and a specialized back-plate is used which allows a Langmuir probe to be placed through with a compression fitting. The Langmuir probe was constructed from a foot long alumina tube with 1/8" outer diameter (OD). Inside is another thinner alumina tube with an inner diameter (ID) just large enough to fit a 0.48±0.02 mm diameter tungsten wire. This pokes out by about 4.4±0.02 mm from the edge of the outer alumina tube. The inner alumina tube is recessed within the outer tube by about 1 mm, in order to shield sputtered tantalum from the ion source coating the inner tube and possibly changing the conductive area exposed to the plasma. The tungsten wire is attached to a Matsusada DJOP60-1 variable power supply which can supply -60 to 60 V and 0 to 1 A used for measuring the current response of the probe to an applied voltage within the plasma. The aperture at the end of the ion source, which is normally used for beam extraction, is where the light from the plasma escapes to be used in OES measurements.

4.5.1 Langmuir Probe Measurements

Langmuir probe measurements were taken by manually moving the Langmuir probe to different positions along the ion source, and then turning it on and taking measurements at different control parameters. The controllable parameters for this ion source are the arc voltage (V_{arc}), arc current (I_{arc}), and input gas flow (Q). The arc current is set by a PID (Proportional-integral-derivative) control loop which finds the right filament current to set a constant arc current. The helium gas flow into the source is regulated with a Brooks Instruments GF40 series mass flow controller. To measure the profile of the electron density and temperature along the axis of the ion source, the Langmuir probe is placed in some position within the ion source, and the bias probe is varied from about -50 V to 0 V, though this range can change depending on the value of the local plasma potential. The resultant current from the power supply is measured on an NI USB-6001 DAQ [57]. This measurement is repeated five times for each position. After every measurement, the plasma must be turned off and the probe moved to its next position, before operating the plasma again and making sure that the arc current is steady to repeat the Langmuir

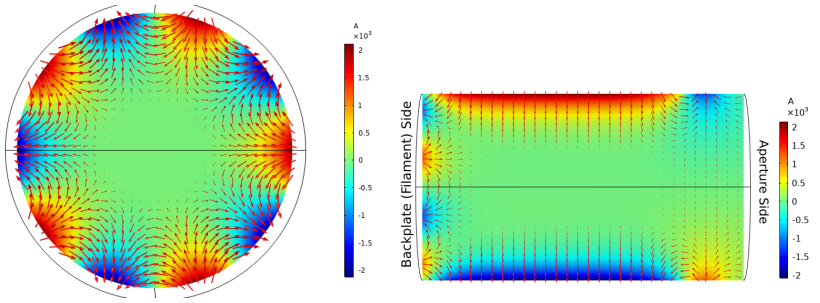

(a) Magnetic field and vector potential cross section

(b) Length-wise cross section of magnetic field and vector potential

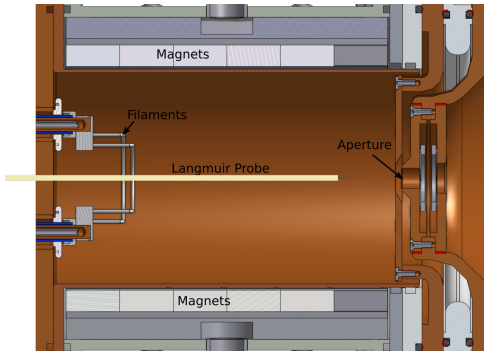

(c) Length-wise cross section

Figure 4.10: Cross sections of TRIUMF-licensed Volume Cusp ion source. Center cross section in (a) shows the logarithm of the magnetic field lines as red arrows, and the magnetic vector potential as a colormap. Similar plot shown in (b) for a length-wise cross section which shows regions of dipole and cusp fields at either end. A similar length-wise cross section in (c) shows the primary components of the Langmuir probe setup.

probe scans.

The errors for each Lanmguir probe measurement (shown in various plots) are estimated as follows. A non-linear least squares fit to the equation for the probe current as a function of bias voltage (equation 4.2) is done using the SciPy curve fitting algorithm optimize.curve_fit [58]. This includes the errors for each current measurement which is estimated to be 1 mA. The error in each parameter is derived from the square root of the diagonal of the covariance matrix. In addition, the fit is also done with the measured probe area increased by the error in its area. The

solution for each plasma parameter in this case is subtracted by the nominal solution to estimate the error from the uncertainty in the probe's area. The total error for a measurement is estimated by adding the two errors in quadrature. Each probe measurement is done at least five times, and thus the final error is the average of the error for each measurement (in quadrature) in addition to the standard deviation of the parameter from the set of measurements.

Figure 4.11 shows the results of this experiment at V_{arc} = 120 V, I_{arc} = 1.5 A, and Q = 20 sccm. The electron density and temperature falls at the magnetic filter field which retards electrons with velocity component going towards the aperture. This is because electrons follow the magnetic field to where it intersects with the chamber walls. This takes away the electrons from this region thus reducing the electron density, and prevents high energy electrons from going towards the aperture thereby reducing the temperature. This fall is less drastic near the filament since this is the source of the primary electrons from the cathode sheath. However, the electron density still falls since most electrons come from multiple ionizations, which require many mean free paths of an electron, and thus a farther distance from the filament will increase electron density assuming the electron temperature stays high. It should be mentioned that even with the layers of ceramic surrounding the thin probe, it was seen that using the Langmuir probe does affect the plasma, sometimes resulting in temporary changes of arc current by about 5%.

Figure 4.12 shows the same plots but with the Langmuir probe fitting for the electron EEDF of a Maxwellian in addition to a flat EEDF. The flat portion of the EEDF goes up to V_{arc} + V_p rather than V_{arc} like in equation 4.8, since the maximum energy an electron can have is the electric potential difference between the filament and the local plasma potential. Figure 4.12a shows the same sort of profile of the main electron parameters T_e and n_e, but with both reduced. Figure 4.12b plots the β parameter, which shows that as we get closer to the the filament, a greater percentage of the electrons are in the hot electron flat EEDF, which is what we would expect since the filament is the source of these electrons, thus there should be more high energy electrons nearby which haven't lost most of their energy. Near the aperture, the magnetic field and drastic drop in plasma parameters creates greater noise to signal ratio at low bias voltage (at ion saturation current region), leading to large errors.

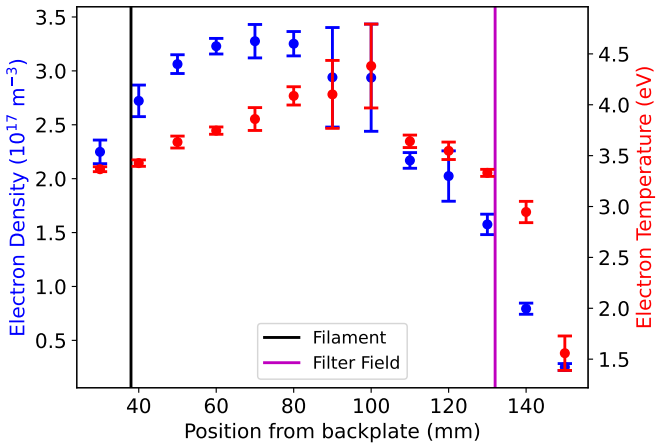

Figure 4.11: Electron density and temperature as a function of position from TRIUMF filament ion source back plate as measured by the Langmuir probe. Also shown is the general location of the filaments and the dipole magnetic filter field

The langmuir probe gives the expected profiles and results based on fundamental plasma dynamics within the ion source. Keeping in mind that 80 mm is halfway along the source, this is likely the source of peak light intensity due to peak electron density and temperature, thus the plane parallel OEF approximation from equation 4.29 will be nominally used for OES measurements of this ion source.

4.5.2 OES system

The simplified setup of the OES diagnostic is shown in figure 4.13. A collimator is attached to a holder plate in the vacuum box on an actuator. The actuator is manually moved until maximum light intensity is reached, which is assumed to be when the collimator is coaxially centered about the aperture. The collected light is then sent through a vacuum compatible fiber optic, an optical feedthrough, another optical fiber, a neutral density (ND) filter (thorlabs NDUV30B), then through another optical fiber to the spectrometer (OceanOptics HR2000+) which measures the light intensity as a function of wavelength. The spectrometer has an estimated 0.5 nm resolution in wavelength. This system has to first be *relatively* calibrated

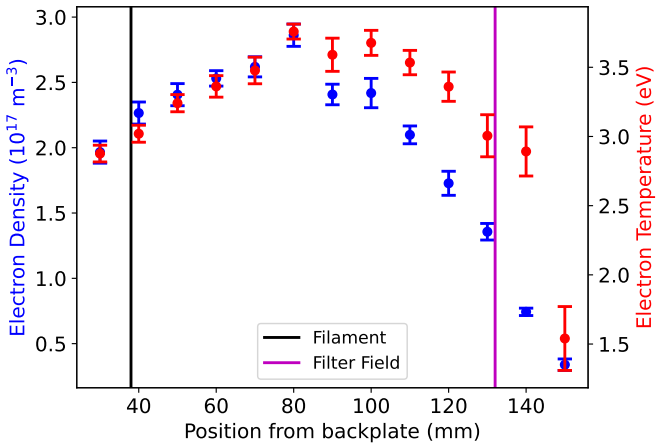

(a) n_e and T_e

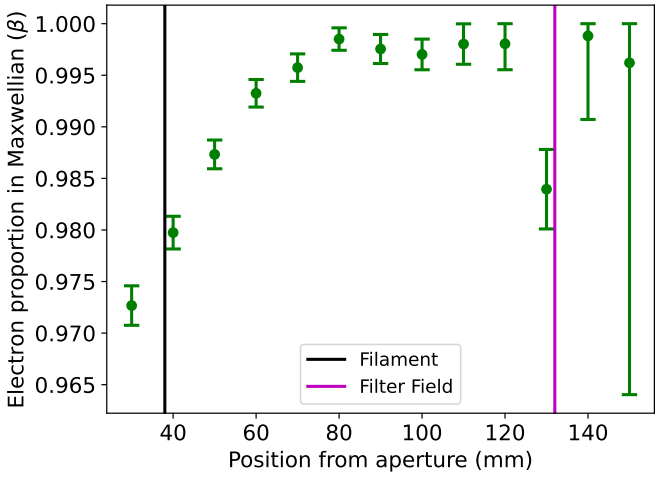

(b) β

Figure 4.12: a) Electron density and temperature and b) β for a Maxwellian + flat EEDF as measured by the Langmuir probe. Also show is the general location of the filaments and the dipole magnetic filter field.

using an Ocean Insight HL-3P-CAL light source with a cosine corrector, which outputs a known intensity as a function of wavelength. After calibration of the optical system, one can then measure the intensity ratios of between measured peaks from spontaneous emission.

Figure 4.14 shows an example measurement (after calibration) with this optical

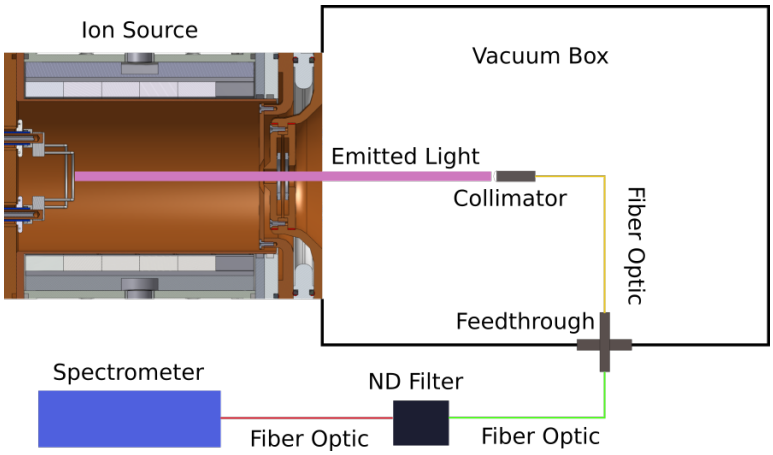

Figure 4.13: Simplified schematic of OES diagnostic setup for the TRIUMF ion source. The collimator is located about 300 mm from the center of the ion source aperture. A vacuum compatible visible-infrared range fiber goes to a vacuum feedthrough and to another UV-infrared fiber, through a ND filter (thorlabs NDUV30B), through a UV-Visible fiber, and then to the HR2000+ OceanOptics spectrometer.

system of the TRIUMF ion source running helium at 120 V, 2 A, and 18 sccm. The common intensity peaks are labeled with their state transitions and wavelength. We see that there is a background spectrum, which comes from the emitted light of the hot tantalum cathode. In order to get the intensity ratios, the peaks are first located and removed (including the fall-off due to peak broadening) using a specialized peak finding algorithm in the SciPy package. The background is then fitted to a polynomial function, and this polynomial is subtracted from the original data to get only the peaks. These peaks are then integrated along their broadened wavelengths, and this final value used as the relative intensity of the line.

As mentioned in section 4.4.4, the intensity ratios of I_{728}/I_{706} and I_{667}/I_{728} are often measured for helium CR-model based diagnostics with the assumption of Maxwellian temperature distributions for the electrons. We will also see how using additional ratios that are less commonly used will affect the diagnostic. The additional ratios are (with wavelength subscript being rounded to the nearest singles digit in nm) I_{501}/I_{728}, I_{447}/I_{706}, and I_{492}/I_{728}.

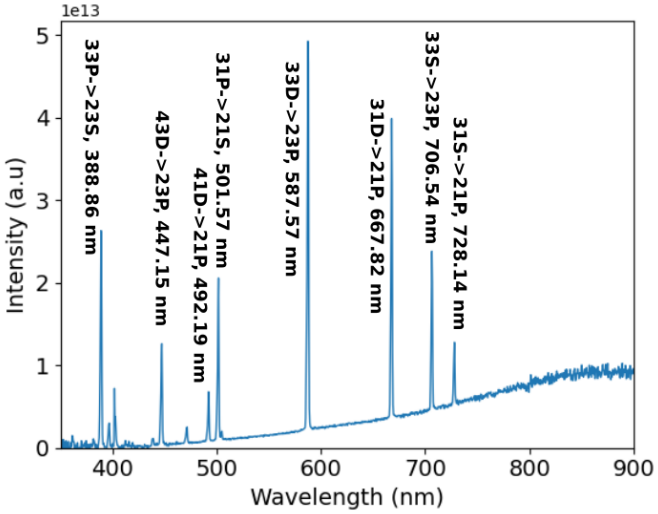

Figure 4.14: Example spectrum measurements (after relative calibration applied) from TRIUMF ion source with helium at 120 V, 2 A, and 18 sccm. Common peaks labeled with their state transition and the wavelength.

4.5.3 Langmuir and OES Comparison for Helium

To get the Langmuir probe measurements at several operational parameters, the Langmuir probe is placed at the center of the discharge, or 80 mm from the backplate, which also corresponds to the peak electron energy density. The population density of neutral helium within the volume as a function of gas flow (at room temperature) was estimated by replacing the backplate of the ion source by a backplate with a fitting that could fit a pirani gauge (Edwards APG100-XM). The pressure measurements compared well with estimated pressure based on MOLFLOW+ simulations. The neutral density as a function of gas flow can then be implemented into the NSCR code, with the assumption that the gas temperature does not significantly differ from room temperature under operation. The neutral helium gas density within the ion source as a function of gas flow is shown in figure 4.15. This shows the measured neutral density (assuming room temperature of 300 K) within the TRIUMF-licensed ion source as a function of the input helium gas flow. The

input parameters that are varied are the gas flow, V_{arc}, and I_{arc}. There are limitations on arc current since past a certain current (about 5 A) the current to the probe will overload the Matsusada power supply. In addition, the ion source does not run stably using helium at voltages lower than 100 V, currents less than 1 A, and gas flows less than 5 sccm. V_{arc} is maximized at 200 V as it's the highest voltage reached by the Sorensen SGA 200-50 power supply used for this purpose. Measurements are made varying each parameter while keeping the other two parameters constant. The input parameters are made to vary as much as possible in order to maximize the changes in local plasma parameters.

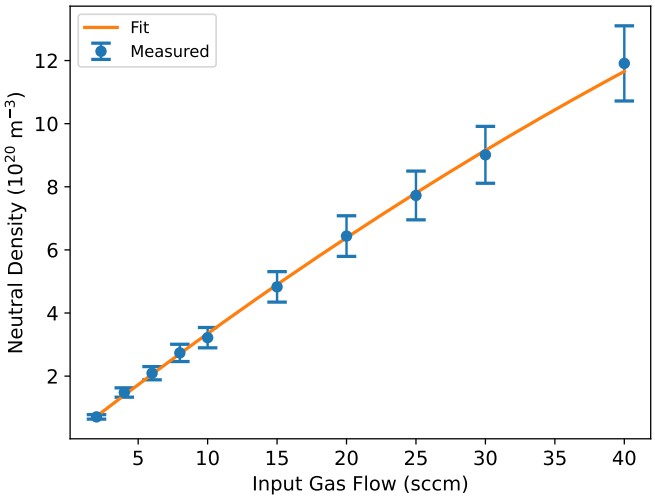

Figure 4.15: Measured and fit neutral gas density vs gas flow in TRIUMF-licensed volume cusp ion source

One of the biggest issues with using the OES on the Volume Cusp ion source is that the line of sight of the radiated emission lines, which is generally taken as radially from the center of a cylinder where one expects the peak density for most plasma experiments, is instead taken from outside the aperture as shown in figure 4.13. In this thesis, a simple estimate will be that the radiation length of light is from the center of the discharge (80 mm from the backplate) and the ground state density is uniform in the plasma. This allows us to use the plane parallel approximation from equation 4.29.

The errors for each plasma parameter as measured by the OES is as follows. Each OES measurement is repeated 10 times and is done with the Langmuir probe placed all the way in the back to avoid perturbations of the plasma due to the probe. The light source used to calibrate the optical system has errors on measured intensities of about 3%. However, we are measuring intensity ratios, and the light source's output spectrum is stable ($<$1% variation) compared to the statistical variations from different measurements. For this reason, the NSCR code is run for each measurement independently to get the parameters of n_e and T_e, and then the mean and standard deviation for each parameter is calculated from the set of individual measurements. However, the error on the pressure reading of the pirani gauge is about 5%, and so the NSCR also solves for each neutral density $\pm$5% for each individual measurement. Thus the total error for each n_e and T_e is estimated as the standard deviation of 30 measurements, with the nominal values simply being the mean. There is no way to estimate the gas temperature, which we assume to be at 300 K. All other errors are systematic errors due to assumptions made within the model.

Figure 4.16 shows why making a CR-model from scratch is important. The electron density and temperature measurements are shown from the Langmuir probe as a function of gas flow (V_{arc} = 120 V and I_{arc} = 1.8 A) compared to measurements with the OES diagnostic. In this case though, the NSCR model does not include radiation trapping, and so the results are similar to what would be extracted from a CR-model implemented by Yacora on the Web. We see that the electron density is orders of magnitude higher than that measured by the Langmuir probe, and the electron temperature is capped at the maximum T_e of 50 eV which was allowed on the grid. Though accuracy is generally difficult to achieve with OES measurements, orders of magnitude differences are extreme.

Figure 4.17 shows the results for electron density and temperature measurements with the Langmuir probe and OES whilst varying the input parameters (with other parameters constant). In this case, the OES includes radiation trapping due to absorption from the ground state using equation 4.29. The variations are done in gas flow (V_{arc} = 120 V and I_{arc} = 1.7 A), arc current (Q = 18 sccm and V_{arc} = 120 V), and arc voltage (Q = 20 sccm and I_{arc} = 1.5 A). The Langmuir probe measurement is taken at 60, 80, and 100 mm to see if the trends of plasma param-

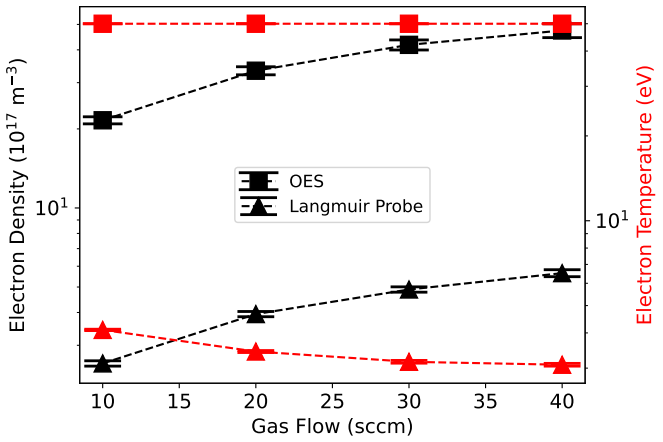

Figure 4.16: OES measurements without radiation trapping included, and Langmuir probe measurements. Electron temperature shown in red, electron density in black. OES measurements are square markers, Langmuir probe measurements are triangle markers.

eters change at different locations. The addition of radiation trapping drastically improves the comparison between the Langmuir probe and OES measurements, thus showing that radiation trapping is a necessary component of the NSCR model. However, the Langmuir and OES measurements are still a few error bars from each other, with the primary reason likely being that the Langmuir probe is a localized measurement whereas the OES measurement is measuring all the light from the solid angle it looks into. This also might be due to the lack of information within the model. This includes the information within the OEF which is only a rough approximation. However, other effects include the assumption of a Maxwellian EEDF commonly used within plasmas. It should be noted that such differences are common even for more advanced implementations of CR-models for helium in other plasma experiments, which also see large factors of 2 or more differences between Langmuir probe and OES measurements [44, 45].

What is important though is the ability to see whether trends in plasma parameters can be replicated, since that is ultimately the primary question of interest: how does changing the input parameters of the ion source effect the internal plasma properties? In this case we see that for all parameter variations regardless of diag-

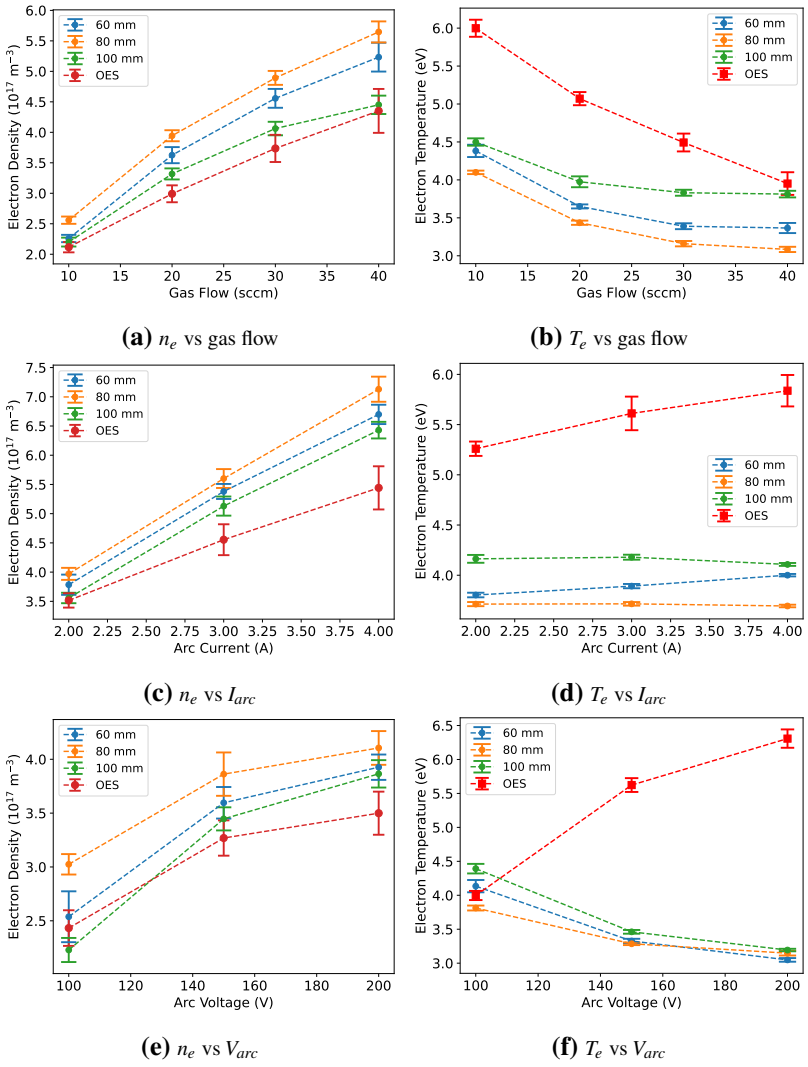

(a) n_e vs gas flow

(b) T_e vs gas flow

(c) n_e vs I_{arc}

(d) T_e vs I_{arc}

(e) n_e vs V_{arc}

(f) T_e vs V_{arc}

Figure 4.17: Variations of (b,d,f) electron temperature and (a, c, e) electron density as a function of (a,b) gas flow, (c,d) arc current and (e,f) arc voltage. Shown are measurements of the Langmuir probe for a Maxwellian EEDF at 60, 80, and 100 mm from the backplate, along with the OES measurements with the NSCR using the 'plane parallel' OEF.

nostic method, electron density is positively correlated with increases in each parameter. For gas flow (figure 4.17a), this is because each electron emitted from the

filament and accelerated across the sheath has more background particles to ionize, thus leading to an increased electron density. For arc current (figure 4.17c), increasing arc current means increasing the filament electron emission, which means more electrons within the ion source and more ionizations. Finally an increase in arc voltage (figure 4.17e) means each emitted electron will be able to ionize more background particles, thus leading to increased electron density. Thus the OES measurement matches trends observed with the Langmuir probe for electron density.

In the case of electron temperature, we start to see deviations between the Langmuir probe and OES measurements. When varying gas flow (figure 4.17b), both diagnostics show a decrease of electron temperature. This is because each electron undergoes more energy-losing interactions with the increased population density of neutral helium atoms, causing a larger loss of energy per electron as gas flow is increased. However in the case of variations of arc current (figure 4.17d), the Langmuir probe temperature measurement stays rather steady with a very slight decrease at 80 and 100 mm from the backplate. However, at 60 mm (getting closer to the filament), the temperature increases, likely due to the greater abundance of higher-energy electrons emitted from the cathode sheath on the filament. Since the OES is looking at the total light emitted along the entire axis, this is likely why the OES measurement instead sees an overall increase in electron temperature with arc current.

A complete disagreement between the two diagnostics in electron temperature is when varying the arc voltage (figure 4.17f). The Langmuir probe for all measured locations has a decrease of electron temperature with increasing arc voltage. This is rather unintuitive, as one would assume an increase of primary electron energy from the cathode sheath due to the increase in arc voltage would lead to a greater electron temperature. To get a better understanding of what's happening, the probe measurements are fitted to a Maxwellian plus flat EEDF (equation 4.8). In this case, the highest threshold for the flat EEDF portion will actually be $V_{arc} + V_p$. The same plots using this new fitting procedure are shown in figure 4.18. Overall the electron density is lowered, which matches better with the OES measurements for each input parameter variation. It also lowers the electron temperature though, which furthers the difference between the OES and Langmuir

temperature measurements for this parameter. Overall the trends do not change significantly.

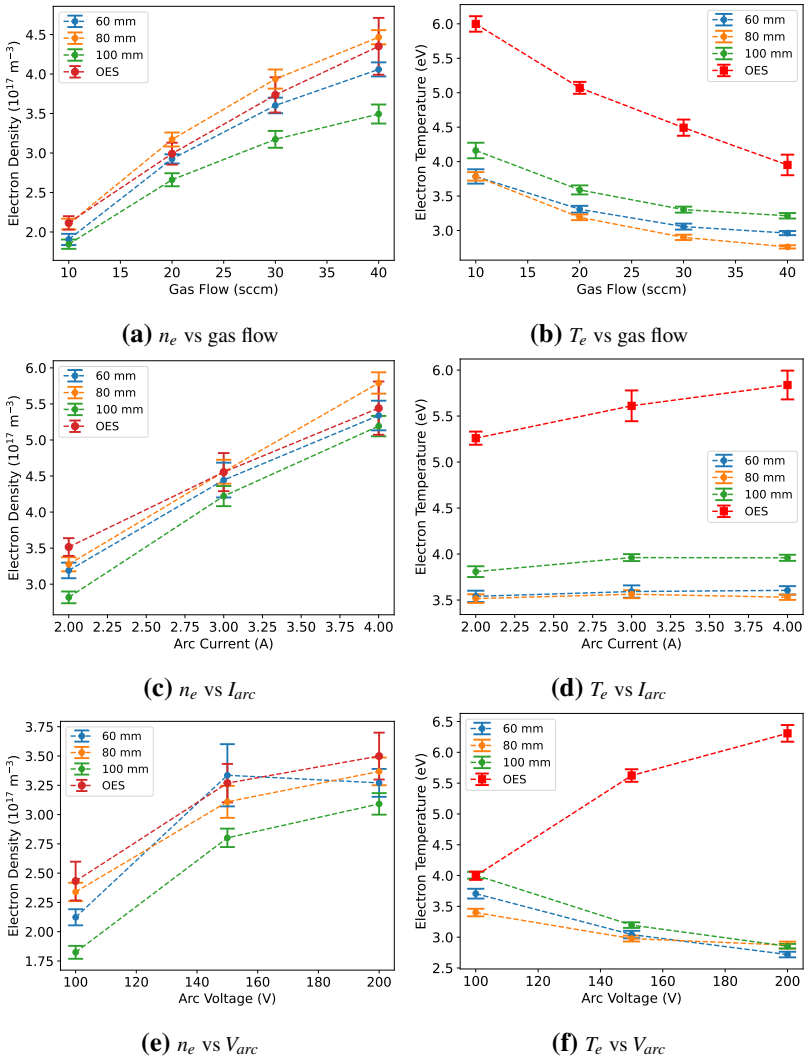

(a) n_e vs gas flow

(b) T_e vs gas flow

(c) n_e vs I_{arc}

(d) T_e vs I_{arc}

(e) n_e vs V_{arc}

(f) T_e vs V_{arc}

Figure 4.18: Variations of (b,d,f) electron temperature and (a, c, e) electron density as a function of (a,b) gas flow, (c,d) arc current and (e,f) arc voltage. Shown are measurements of the Langmuir probe for a Maxwellian plus flat EEDF at 60, 80, and 100 mm from the backplate, along with the OES measurements with the NSCR using the 'plane parallel' OEF.

However, the discrepancies in electron temperature can be explained by looking at figure 4.19, which shows the variations of β, or the proportion of electron density within the colder Maxwellian EEDF, from equation 4.8 as a function of gas flow, arc current, and arc voltage. Figure 4.19a shows that increasing the gas flow increases the amount of electrons in the colder bulk electrons. This is expected, since the higher amount of gas particles increases the amount of energy losing collisions for each primary electron, thus increasing the amount of colder electrons in the plasma. This is what leads to a decreasing temperature. For variations in arc current (figure 4.19b), an increase of arc current leads to a smaller β, which is due to the increased amount of high-energy electrons emitted from the filament. Variations in arc voltage (figure 4.19c) also show the same trend, likely due to the increased mean free path at higher electron energies thus decreasing the probability of interaction, resulting in greater amount of these high-energy electrons in the background. This is also the reason why β is smaller at lower position values closer to the filament in all cases, since these high energy electrons have not had sufficient collisions to lose all their energy and become part of the colder Maxwellian bulk electrons.

One will notice that an increase of β is directly correlated with a decrease of electron temperature in the OES case for all parameter variations. This suggests that due to the line of sight of the light measurement reaching all the way to the back of the ion source (where high energy electrons are expected), a strong component of the high-energy non-Maxwellian EEDF is affecting the line-intensity ratios emitted within the plasma. The NSCR *err* minimum which best matches this case is a higher-energy Maxwellian EEDF, likely because the larger high-energy tail, which is the main driver of helium excitations from the ground state, is closer to the high energy tail of the real distribution even if the actual bulk electrons are of a lower temperature. Unfortunately, attempting to solve for the NSCR using a Maxwellian plus flat EEDF leads to several local minimums when minimizing $err(T_e, n_e, \beta)$, even when using additional ratios in an attempt to increase the constraints in the minimization calculation. This minimization procedure will often output the minimum T_e in the grid with varying β values, though will sometimes also output T_e close to the Maxwellian case with β close to 1. Thus the OES diagnostics currently cannot be used to solve for non-Maxwellian distributions.

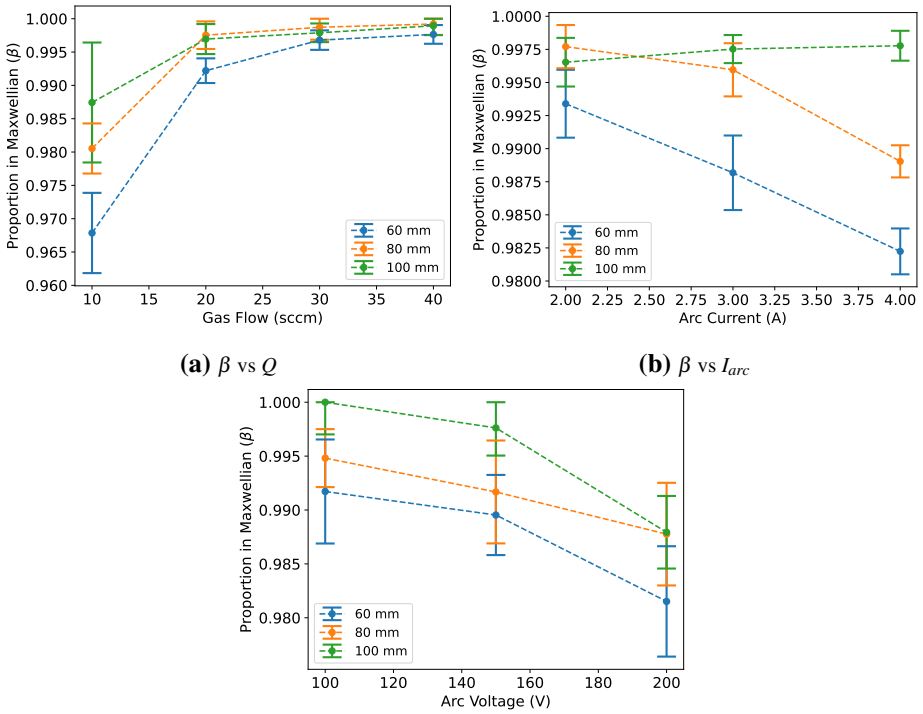

(a) β vs Q

(b) β vs I_{arc}

(c) β vs V_{arc}

Figure 4.19: Variations of β (proportion of electrons in colder Maxwellian EEDF) as function of (a) gas flow, (b) arc current, and (c) arc voltage as measured by the Langmuir probe at positions of 60, 80, and 100 mm from the backplate.

It should be noted that the Langmuir probe fitting procedure can also be done with a bi-Maxwellian, however the additional variable of T_h has an error from the fit of about 200%. This is essentially over-fitting due to the poor signal-to-noise ratio at the low V_B range, where each point has an error of about 1 mA but the measurements are at a few mA. In addition, only a small section of the high-energy electron EEDF can be sampled since the plasma potential is between -20 and -10 volts, which leaves only about 40 V less than V_p for sampling. This is also why the relative error in β for the flat EEDF is quite large, though they are still small enough to show a clear trend when varying input parameters. To increase accuracy, we would need a power supply that can go down to the arc voltage and which is

accurate within the mA range. It is clear why many plasma physicists simplify the EEDF to a Maxwellian distribution, as finding the true EEDF experimentally is a complex task.

A Maxwellian EEDF is not the only simplifying assumption, as the choice of OEF is also an important piece of the NSCR code. To check the dependency of the trends on the OEF, different geometrical simplifications used to solve the OEF were used to see if they significantly change the measured trends in electron temperature and density. An example of the OES measurements as a function of gas flow variations along with measurements from the Langmuir probe at 80 mm is shown in figure 4.20. The OEFs included are for the plane parallel, spherical (equation 4.30), and radial cylinder (equation 4.28) geometries. For each case the radiation length l_{rad} is chosen to be L/2 which corresponds to the center of the discharge. We see that for both electron density and temperature, the trends are unchanged relative to the nominal plane parallel case. This is also true for variations in arc current and arc voltage. Thus the estimate of the OEF is not expected to change the trends in the OES measurements.

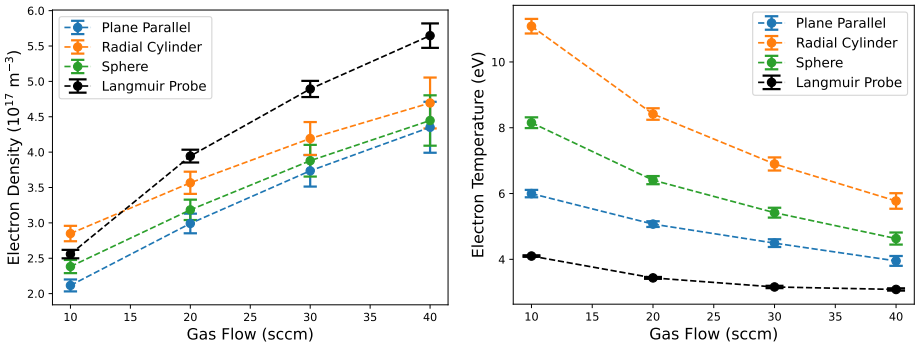

(a) Electron Density **(b)** Electron Temperature

Figure 4.20: OES measurements using various OEFs within the NSCR code. Measurements are for a) electron density and b) electron temperature. Langmuir probe measurements at 80 mm also shown.

Finally we should check to see if the addition of other less common ratios sometimes used by those in the field (I_{501}/I_{728}, I_{447}/I_{706}, and I_{492}/I_{728} ratios) will impact these trends. We can also add absorption of the 2^3S and 2^1S metastable

states, which might reach sufficient population densities to take significant part in the absorption process. To do this, the regular NSCR model is solved using the absorption from the ground state as the primary mechanism. The given solution of population densities for the grid of T_e and n_e values are then used to evaluate the new absorption coefficients for the ground and metastable states. These generate a new OEF, which is used in the next iteration of the matrix solver. This iteration process continues until the populations for each excited state are within 0.1% of the previous iteration. It should be noted that this assumes the metastable states are uniform throughout the geometry like in the ground state.

Figure 4.20 shows the OES measurements using the different intensity ratios and metastable iterations compared to the Langmuir probe at 80 mm when varying arc current. The primary ratios include only the commonly used I_{728}/I_{706} and I_{667}/I_{728} ratios. Additional ratios include those mentioned above, and additional ratios plus the metastable opacity uses the iteration procedure discussed previously. For all other input parameter variations of the ion source operation, the trends of electron temperature and density are the same as in the nominal case with the two primary ratios. However, only with the arc current does the additional ratios (including with metastable iterations) actually change the entire trend of electron temperature. In this case, this measures an electron temperature that is negatively correlated with arc current, which is likely not the case based on Langmuir probe measurements. Other issues with the metastable iteration procedure are significant computational time increases and further disagreement with the electron density measurement from the Langmuir probe. For these reasons, OES measurements will be kept using the more commonly used I_{728}/I_{706} and I_{667}/I_{728} ratios.

4.6 Cold Cathode Penning Ion Source

Due to technical issues with the primary Glassman EV series power supply, only preliminary data could be obtained for the PIG source under high current hot cathode operation. However, access to a Glassman EV series (8 kV x 140 mA) power supply allows the ion source to be operated in a cold cathode mode with minor modifications. This is useful because a cold cathode ion source generally has lower electron density and consequently are closer to corona-type plasmas. These are

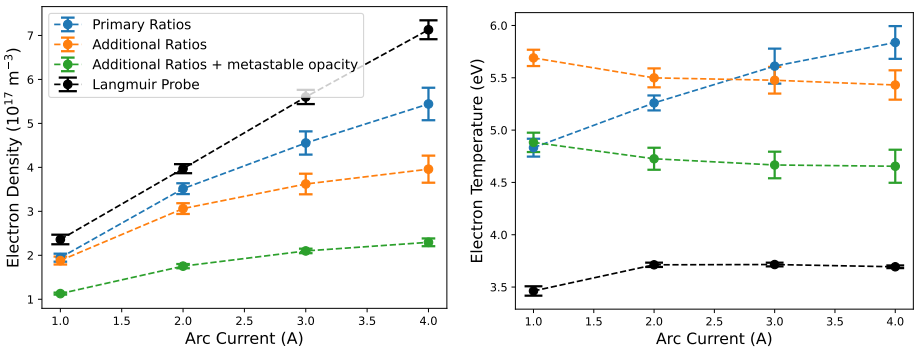

(a) Electron Density

(b) Electron Temperature

Figure 4.21: OES measurements using typical two ratios, additional I_{501}/I_{728}, I_{447}/I_{706}, and I_{492}/I_{728} ratios, and using these additional ratios combined with iterations to include radiation trapping from the metastable states. Measurements are for a) electron density and b) electron temperature. Langmuir probe measurements also shown.

simpler to model for OES diagnostics and within plasma simulations due to the approximation of most electron-neutral reactions being with the dominant neutral ground state population. As the OES is the only diagnostic that can currently be used on the PIG source, it is important to have secondary confirmation of what is measured using modeling techniques. Therefore, a cold cathode operation will allow for better comparison between models, which is an important stepping stone before operating in the more complex hot cathode mode.

In order to use the PIG source in the cold cathode mode, a thicker neck graphite cathode needed to be made which replaces the thin necked tantalum cathode used to keep the cathode hot (figure 3.22). A photo of one of the graphite cathodes after use is shown in figure 4.22. A clear light circle is seen where the cathode is exposed to the plasma, which is where the ions from the plasma bombard the cathode as expected.

Experimental observations showed that there are essentially two different regimes within the cold cathode operating mode. There is the high pressure and low magnetic field regime, which happens at gas flows of > 15 sccm and magnetic fields strengths of < 0.08 T. Higher magnetic fields cause the plasma to transition to a hot cathode mode which maximizes the current to 140 mA while lowering the set

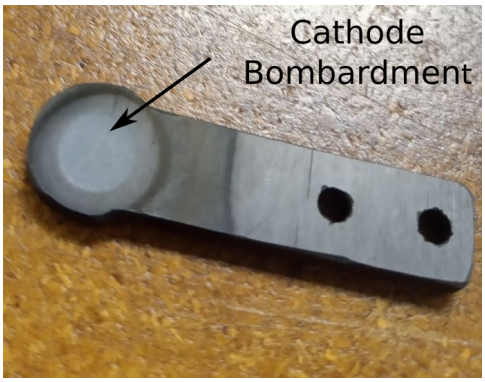

Figure 4.22: Graphite cathode for cold cathode operation after use. Light spot in center is region where plasma ions bombard the cathode.

arc voltage. The other regime is the low pressure and high magnetic field regime. This happens at gas flows < 6 sccm and magnetic field strengths > 0.1 T. Higher pressures will also cause the ion source to arc to a hot cathode regime which peaks the current of the power supply. Both regimes operate at greater than 1 kV arc voltage.

The operational parameters of the PIG source under the cold cathode mode is the output arc voltage V_{arc}, the magnetic field strength, and the gas flow of helium within the ion source. This means the arc current I_{arc} is dependent on these parameters, so changing any of these parameters will also change I_{arc}. Figure 4.23 shows how I_{arc} varies as a function of each operational parameter (while keeping other parameters constant). I_{arc} increases with the increase of each parameter. This is likely due to an increase of ionizations of background gas for gas flow, and increase of electron energy available for ionizations for V_{arc}, and the increased confinement of electrons with magnetic field. Figure 4.24 shows similar plots but for the low pressure at high magnetic field regime. Here we see similar trends in I_{arc} for the various operational parameters for the same reason.

4.6.1 OES Measurements

Measurements using the OES diagnostic were implemented via a collimator attached to an optical feedthrough placed on a flange directly across the ion source

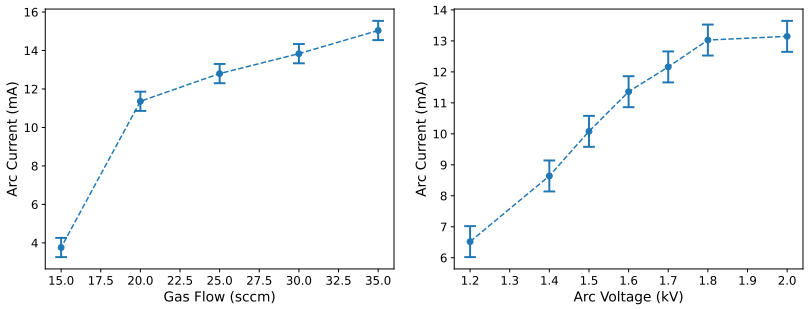

(a) I_{arc} vs gas flow

(b) I_{arc} vs V_{arc}

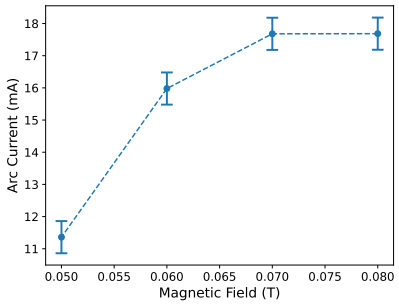

(c) I_{arc} vs magnetic field

Figure 4.23: I_{arc} as a function of (a) gas flow, (b) V_{arc}, and (c) magnet field strength in the high pressure low magnetic field regime. Constant parameters for each variation are (a) 1.6 kV and 0.05 T, (b) 20 sccm and 0.05 T, and (c) 20 sccm and 1.6 kV.

in the vacuum box. A simplified schematic is shown in figure 4.25. The light passes through two optical fibers and an attenuator (which is simply an air gap of about 40 mm) before being collected by the HR2000+ OceanOptics spectrometer. This setup is relatively calibrated with the HL-3P-CAL light source. As done for measurements with the TRIUMF filament ion source, each measured line intensity peak is integrated over its broadened profile. In this case, there is no background light intensity that needs to be subtracted out due to a lack of any hot filament within view of the optical collimator.

The PIG source was run varying gas flow, arc voltage, and magnetic field while keeping the other operational parameters constant. For each case, the varying parameter was swept from lowest to highest value. This is to avoid hysteresis effects,

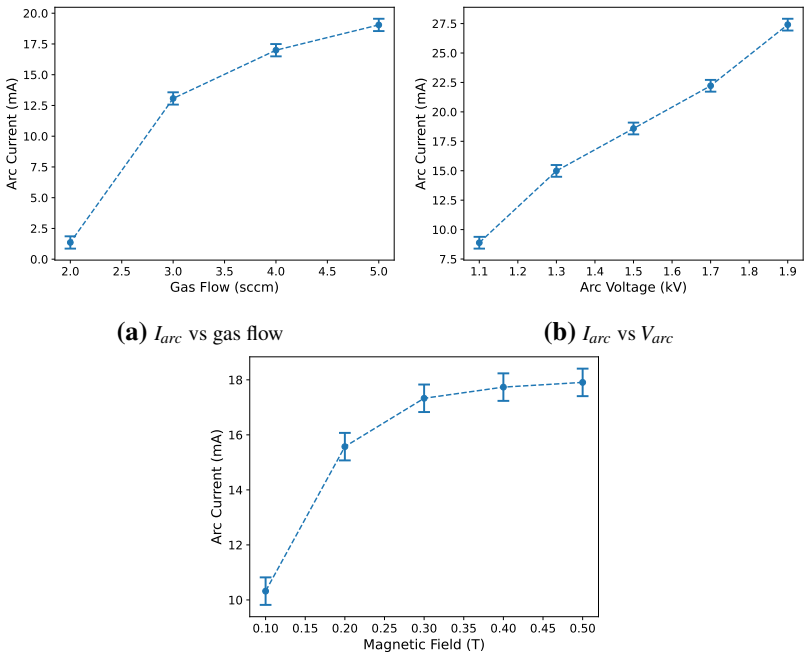

(a) I_{arc} vs gas flow

(b) I_{arc} vs V_{arc}

(c) I_{arc} vs magnetic field

Figure 4.24: I_{arc} as a function of (a) gas flow, (b) V_{arc}, and (c) magnet field strength in the low pressure high magnetic field regime. Constant parameters for each variation are (a) 1.4 kV and 0.4 T, (b) 4 sccm and 0.39 T, and (c) 4 sccm and 1.45 kV.

which have been observed when varying each parameter. The hysteresis effects are not enough to change the trends in I_{arc} as a function of each varying parameter. The ranges of each parameter are limited as lower values will dissipate the discharge, while higher values will make the discharge transition into a hot cathode state. Each point in parameter space selected is the same as shown in figure 4.23 and 4.24. For each point, up to 10 spectral measurements are taken and used to solve for the plasma parameters within the source. The OEF from equation 4.28 is used as it is most appropriate for measurements taken radially from a cylindrical ion source. The OEF is applied to direct radiative transitions to the ground state, with the assumption that the ground state helium atoms are the dominant source of absorption. Figure 4.26 shows the simulated neutral density for various input

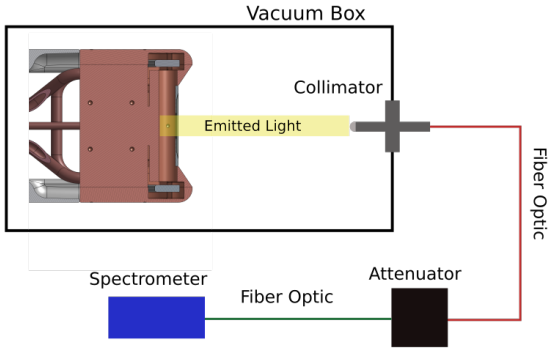

Figure 4.25: Simplified schematic of OES diagnostic setup for the Penning ion source. The collimator is held up by the optical feedthrough on a flange about 160 mm from the center of the ion source aperture. A UV-visible fiber goes through an attenuator filter (40 mm air gap), through a IR-visible fiber, and then to the HR2000+ OceanOptics spectrometer.

helium gas flows within the Penning ion source using MolFlow+, along with the corresponding linear fit. This is used to estimate the neutral density within the ion source for the NSCR.

Figure 4.27 shows the measured n_e and T_e as a function of each operation parameter as measured with the OES diagnostics. Shown are the solutions for the OES diagnostics using just the primary ratios (I_{728}/I_{706} and I_{667}/I_{728}) as circles and all ratios as squares. Electron temperature is in red and electron density in black. It is unsurprising that the electron density increases with increases of each parameter, since I_{arc} also increases. Since the magnetic field is either constant or increasing for each variation, making the radial confinement either the same or better, the electron density has to increase in order to have more electrons satisfying the current constraint on the anode.

As in the case of the TRIUMF ion source, figure 4.27a shows that the electron temperature is negatively correlated with an increase in gas flow. This is likely due to the increased collisions with background gas particles increasing the energy

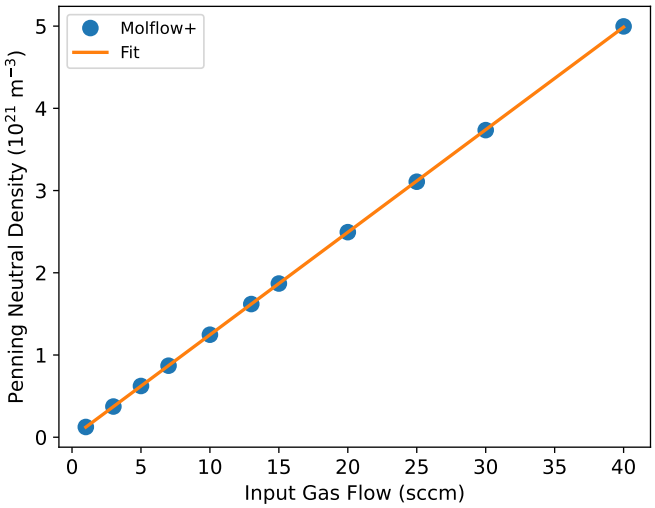

Figure 4.26: Neutral gas density vs gas flow within the Penning ion source using MolFlow+ (blue), and the corresponding linear fit (orange).

loss per primary electron. This is the same reason why we see a decrease in figure 4.27c, where an increased confinement means a primary electron undergoes more collisions. It is interesting however that the electron temperature is reduced as a function of V_{arc}, even though each primary electron is expected to be at a higher energy and would thus increase the electron temperature.

Figure 4.28 shows the same plots but for the lower pressure and higher magnetic field case. We see the same general trends as in the high pressure case, except for at high magnetic fields. Figure 4.28c shows a very interesting trend where past about 0.3 T, the electron temperature starts to rise again while the electron density decreases. This might be attributed to the increased bowing of the magnetic field. As shown in figure 3.3, it is expected that the bowing of the magnetic field increases the proportion of the magnetic field pointing towards the anode. It could be that this slight bowing drastically increases electron dumping to the anode past 0.3 T, and thus the confinement is actually decreased. However, in these type of plasma geometries it turns out that the two regimes being tested refer to two different modes of operations [59]. The low pressure and high magnetic field mode corresponds to an increase in plasma instabilities, theorized to be dominated by

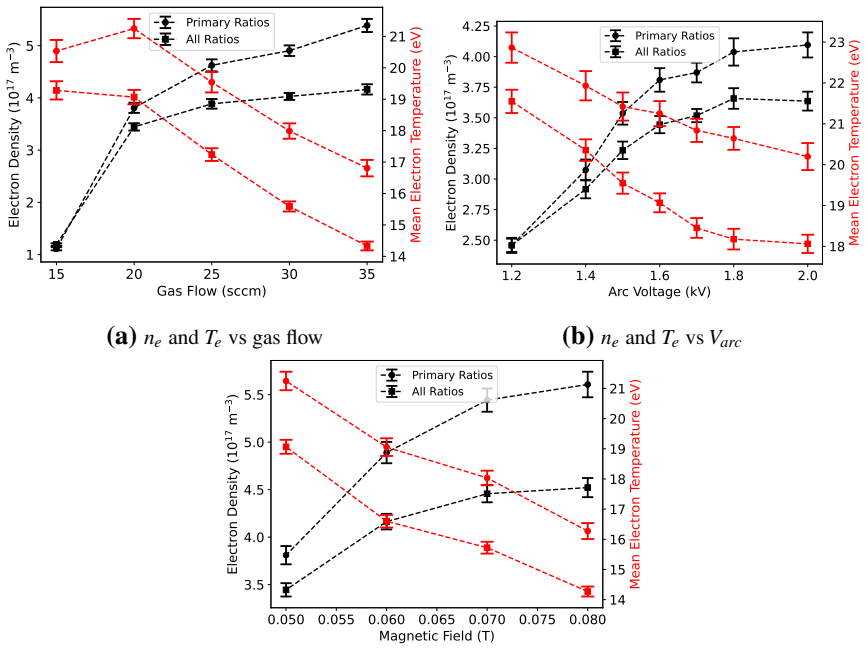

(a) n_e and T_e vs gas flow

(b) n_e and T_e vs V_{arc}

(c) n_e and T_e vs magnetic field

Figure 4.27: n_e (black) and T_e (red) as a function of (a) gas flow, (b) V_{arc}, and (c) magnet field strength in the high pressure low magnetic field regime. Measured using OES with two primary ratios (circle) and all ratios (square). Constant parameters for each variation are (a) 1.6 kV and 0.05 T, (b) 20 sccm and 0.05 T, and (c) 20 sccm and 1.6 kV.

beam plasma instabilities due to two electron beams flowing against each other from opposite cathodes [60], and instabilities that lead to increased plasma diffusion across the magnetic field [61]. It is possible that the strange trends in plasma parameters switching at 0.3 T is related to an increased electron transport due to these instabilities, which causes more electrons to be dumped onto the anode at a particular magnetic field strength.

Like in the TRIUMF ion source, these trends can only be explained by our understanding of fundamental plasma dynamics. However, it would be useful to simulate this ion source to make sure we can replicate these findings, and therefore have a better understanding of the plasma processes that lead to these trends. This will be discussed in the following chapter.

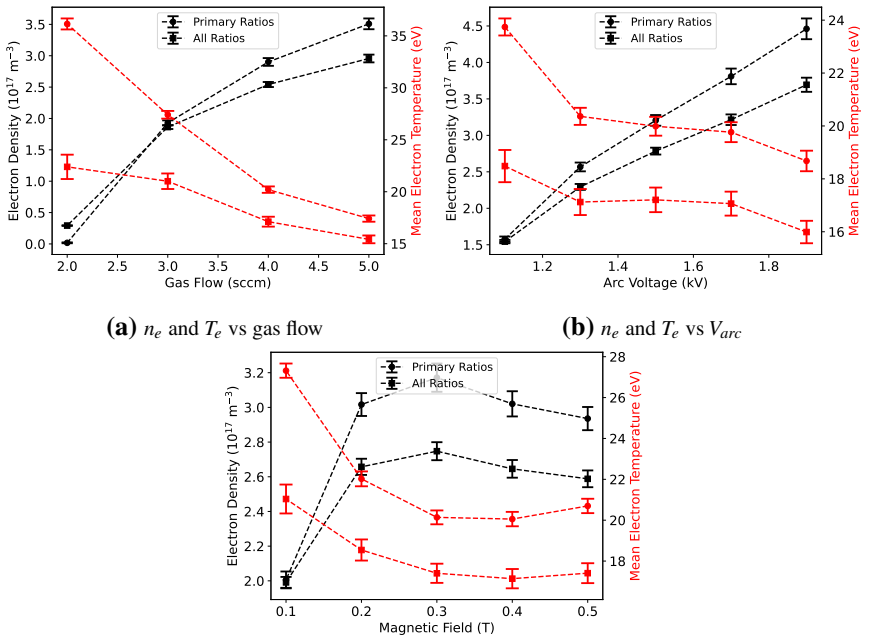

(a) n_e and T_e vs gas flow

(b) n_e and T_e vs V_{arc}

(c) n_e and T_e vs magnetic field

Figure 4.28: n_e (black) and T_e (red) as a function of (a) gas flow, (b) V_{arc}, and (c) magnet field strength in the low pressure high magnetic field regime. Measured using OES with two primary ratios (circle) and all ratios (square). Constant parameters for each variation are (a) 1.4 kV and 0.4 T, (b) 4 sccm and 0.39 T, and (c) 4 sccm and 1.45 kV.

Chapter 5

Plasma Modeling

5.1 Plasma Modeling in Ion Sources

Plasma physics is fundamentally a many-body problem which has high degrees of complexity. Typically in ion sources, the combination of low neutral gas pressures and high electro-magnetic fields makes models based on general particle statistics (such as fluid models) less than ideal. For this reason, Particle-in-Cell (PIC) codes are often used for such ion sources [62–65], usually in combination with Monte-Carlo (MC) methods for randomized collisions.

These types of codes use up to millions of macro-particles which represent the collection of charged electrons and ions. However, unlike the charged particle tracing module, Maxwell's equations are solved self-consistently for each time step for all particles on a grid. In addition, other interactions (such as collisions or surface reactions) may be added for each time step, which further complicates the computation. This requires parallelization, which is doing simultaneous calculations on many CPUs.

Though these codes can simulate most fundamental plasma processes, the coding involved is difficult, and the simulation times are large. For example, even a 2-D PIC simulation of a low-pressure Penning ion source along the center of the discharge typically takes 5-10 days [63]. Such codes would take years to develop, and would still be very impractical to use when changing ion source parameters due to the amount of time needed for an average run. For this reason, alternative

codes must be used which are relatively simpler that can give qualitative results of what happens to an ion source plasma when the input parameters are changed.

It is for this reason that the plasma module from COMSOL Multiphysics™ is used. This module solves the drift diffusion equations described in section 2.5.1. This is described in the Plasma Module User's Guide [66]. Like most COMSOL™ modules, this solves a set of partial differential equations on a spacial grid (from 1-3 dimensions) using the finite element method. This assumes a collisional plasma with Maxwellian electron energy distributions. This may be valid in the bulk plasma of ion sources, but in the sheaths and in areas where there may be anomalous effects (such as from plasma waves), this will not work. However, there are ways to modify this code so that it is better adapted to the ion sources at more moderate pressures ($>$ 20 mTorr) explored with the PIG source in this thesis. In this way, while the code will never be able to give the most accurate results due to its simplification of a complex many-body problem, it should be able to give qualitative trends for the physical processes as a function of the input parameters. This would allow us to explore why changing input parameters leads to various changes in plasma beam parameters without resorting to complex codes which takes multiple days for single runs.

5.2 Comsol Plasma Model

5.2.1 Particle Transport

The plasma domain solves for the time dependency of electron density n_e, the mean electron energy $\bar{\varepsilon}$, and the electric potential V. An isotropic Maxwellian distribution of electrons is assumed, and therefore $\bar{\varepsilon} = \frac{3}{2}T_e$. The time dependency of the electron density is described by:

$$\frac{\partial n_e}{\partial t} = \nabla \cdot \Gamma_e + R_e \tag{5.1}$$

$$\Gamma_e = n_e \vec{u_e} = -(\mu_e \cdot \vec{E}) n_e - \nabla(D_e n_e) \tag{5.2}$$

where Γ_e is the electron flux, μ_e is the electron mobility, R_e is the electron production rate, and D_e is the electron diffusion coefficient. This is essentially just the basic continuity equation in a fluid, in which the rate of change of n_e in a volume is equal to the influx of particles on the volumetric surface in addition to the production of electrons in the volume.

For electrons, the software also solves for the time dependent energy density, which is defined as $n_\varepsilon = n_e\bar{\varepsilon}$. This is defined as:

$$\frac{\partial n_\varepsilon}{\partial t} + \nabla \cdot \Gamma_\varepsilon + \vec{E} \cdot \Gamma_e = S_{en} + Q/q \tag{5.3}$$

$$\Gamma_\varepsilon = -(\mu_\varepsilon \cdot \vec{E})n_\varepsilon - \nabla(D_\varepsilon n_\varepsilon) \tag{5.4}$$

$$D_\varepsilon = \frac{5}{3}D_e\ ,\ \mu_\varepsilon = \frac{5}{3}\mu_e \tag{5.5}$$

where S_{en} is the volumetric electron energy loss/gain due to inelastic collisions, Q is a heat source, μ_ε is the electron energy mobility, D_ε is the electron energy diffusivity, and Γ_ε is the electron energy flux.

The electron volumetric production is given by the sum of the volumetric rates which is equation 2.14 multiplied by the electron density for each ionized n_k background species:

$$R_e = \sum_k K_k^{ion} n_k n_e \tag{5.6}$$

The volumetric electron energy loss is the sum of all electron energy loss due to inelastic collisions with species n_k:

$$S_{en} = \sum_k K_{kj} n_k n_e \Delta\varepsilon_{kj} \tag{5.7}$$

5.2.2 Magnetic Field Effects

As discussed in section 2.5.2, strong DC magnetic fields will affect the trajectories of colliding electrons perpendicular to these fields. In COMSOL™, this causes

the mobility coefficient to become a tensor as the mobility becomes non-isotropic. This creates a mobility along the magnetic field which is the same as the non-magnetic case, and a separate mobility which represents severely restricted drifts perpendicular to this field. In addition, there is also a Hall drift, which is the electron drift in the $\vec{E} \times \vec{B}$ direction.

However, Penning ion sources would not be able to reach the large currents in arc discharges if classical diffusion was the dominant source of cross-field diffusion. It turns out in devices with strong magnetic fields and pressure gradients, anomalous diffusion comes into play due to plasma instabilities [63, 67–76]. These instabilities have shown to be essential in Penning-type discharges as well in order to reproduce the observed currents [61, 63, 77].

While these anomalous diffusion effects are an active area of plasma research, the exact reasons for these processes are still not very well known. The consensus is that the dominant source of diffusion perpendicular to a magnetic field is due to resistive drift waves, as explained by Curreli [78]. This is a result of density gradients which are seen in all confined plasmas, hence why these instabilities are referred to as universal instabilities. The way it works is shown in figure 5.1. Random oscillations in plasma density create oscillations in voltage, with relative positive and negative potential shown by the + and - symbols. This creates electric fields (green) which in combination with the magnetic field cause an $\vec{E} \times \vec{B}$ drift outwards. Since the ions have much larger gyroradii in the magnetic field which may not be fully contained in the electric field, the electrons tend to drift out a bit quicker. This causes a negative charge to build up and causes the next density oscillation to be shifted slightly downwards. This makes it so that these electrons are then caught in the next $\vec{E} \times \vec{B}$ drift, creating a net outward diffusion to the walls.

An important feature that allows these oscillations to exist is that charge imbalances cannot be readily compensated by electrons along the magnetic field lines. This is because electrons will undergo collisions with background particles preventing the neutralization of any oscillations, hence why these are called resistive drift waves.

Results from several experiments show a $\frac{1}{B}$ scaling of this diffusion (classical is $\approx \frac{1}{B^2}$) and also a proportionality to electron temperature. The empirical diffusion coefficient which has come about due to these observations following what is

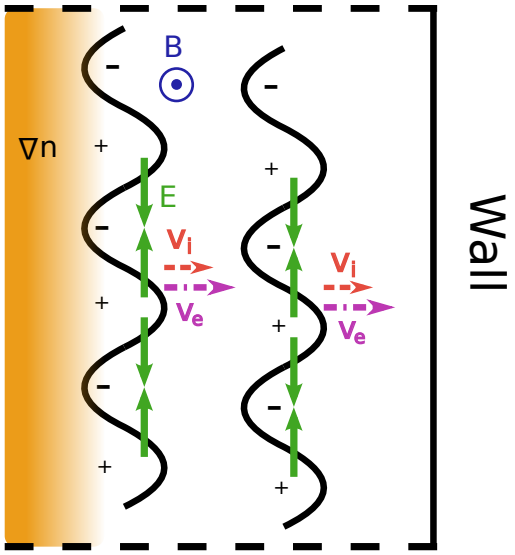

Figure 5.1: Schematic for resistive drift waves. Oscillations in plasma density and therefore voltage shown, with resultant electric fields in green, and resultant $\vec{E} \times \vec{B}$ drift for the electrons (purple) and ions (red).

referred to as the Bohm diffusion coefficient:

$$D_{bohm} = \frac{T_e}{16B} \tag{5.8}$$

where T_e is represented in eV and B the strength of the magnetic field in T. The $\frac{1}{16}$ term is an empirical number which agrees with many experiments within a factor of 3 [23].

There are simplified models of electron mobility by those working in the field of hall-thrusters where anomalous cross-field drift is also observed. In this case, many use the classical equation 2.22 but instead of using an electron-neutral collision frequency, one finds the effective frequency [79]:

$$\nu_{eff} = \nu_{en} + \nu_{ei} + \frac{1}{16}\alpha_p \omega_e \tag{5.9}$$

where ν_{en} is the electron-neutral collision frequency, ν_{ei} is the electron ion collision frequency, and the last term represents the anomalous collision frequency due to

the gyrofreqency of the electron ω_e. α_p is an parameter usually used for fitting experimental results in hall-thruster experiments. In this case, the classic case of $\alpha_p = 1$ will be used as it is unknown what it may be for PIG sources. This is called the *mixed mobility* case.

5.2.3 Heavy Particle Drift

For each heavy particle species, in this case the various states of helium, the particle transport for species n_k is:

$$\frac{\partial n_k}{\partial t} = \nabla \cdot \vec{j_k} + R_k - (\vec{u} \cdot \nabla) n_k \tag{5.10}$$

where n_k is the population density of species k, R_k is the volumetric rate for the species, $\vec{u}$ the total fluid velocity vector, and $\vec{j_k} = n_k \vec{v_k}$ is the diffusive flux where:

$$\vec{v_k} = D_k \frac{\nabla n_k}{n_k} - z_k \mu_k \vec{E} \tag{5.11}$$

with D_k the diffusion constant for species k, z_k the species charge, and μ_k the species mobility. Just like in the electron case the species mobility can be a tensor if a DC magnetic field is introduced. It should be noted that the energy equation is not solved for heavy particles, as it is assumed their energy contribution is negligible compared to the electrons due to a much lower temperature.

With the existence of different charged particles, the equations are closed by solving for the electric fields in the domain due to variations in space charge as these charged particles move. This is done by solving Poisson's equation, shown in equation 3.6.

5.3 1-D Model

In addition to anomalous magnetic field effects, strong electric fields such as those found in the high voltage cathode sheath of a DC discharge are also problematic for COMSOL™ and cannot be well represented by the drift-diffusion model. From equation 5.11 and 5.2 for the ions and electrons respectively, we see that the velocity of the charged particles due to an electric field is linear with $\vec{E}$ and independent of the actual change in electric potential, since it's assumed that the particle veloc-

ities are limited by collisions with the background gas. This may be valid for low values of $\frac{|\vec{E}|}{n_g}$, but when this ratio is especially high, the electron will not undergo collision within the field due to its high speed and the decrease in collision cross section at higher kinetic energies. This means that the drift velocities in the model will be much higher then their theoretical limit.

In order to describe this sheath, the model needs to be modified. COMSOL™ contains an advanced feature which allows for arbitrary PDEs in common forms to be coupled to whatever physics equations are already being solved by the time-dependent solver. A PDE is created which implements equation 2.13 for an ion species, which is usually necessary in low-pressure plasmas with high fields [80]. This however introduces a non-linear velocity term referred to as the *inertial term* $(\vec{u}\cdot\vec{\nabla})\cdot\vec{u}$, which makes 2-D modeling very difficult to converge and computationally expensive. It is expected that these high voltage sheaths are along the magnetic field and hence a 1-D model representing the dimension along the magnetic field of the ion source is made to get consistent convergence of the steady state solver.

The 1-D model is simply a line from the coaxial center of the Penning ion source down to the center of one of the cathodes, which is 25.5 mm in length. Only half the length has to be solved due to symmetry of the ion source about its center. For this reason, a $\vec{E}\cdot\vec{n} = 0$ boundary (or *Neumann boundary*) is applied to the point at the center of the discharge for Poisson's equation. At the other end where the cathode is, the voltage is set to ground with V = 0 (a *Dirichlet boundary*). A simplified schematic of the 1-D model is shown in figure 5.2.

Each point on the 1-D domain represents a circular cross-section of the PIG source, which has a 4 mm radius (which we symbolize as R). Radial losses of electrons to the anode walls is included. The drift diffusion equations (5.11 and 5.2) at steady state are applied in this simplified case so that the total loss rate at the wall for a linear drop in density along the radius (using divergence theorem) is $\Gamma\frac{2}{R}$. For the electrons, we assume the mobility μ_e is derived from the classical case (equation 2.23) or using the effective frequency used by hall thruster physicists (equation 5.9). The Einstein relation is used to then find the diffusion coefficient, which turns out to be very similar to the Bohm diffusion coefficient for the mixed mobility case. The radial electric field is also assumed to be linear, and so $E_r = \frac{V_{arc}-V}{R}$ where V is the voltage parameter solved along the domain in COMSOL™ along the 1-D

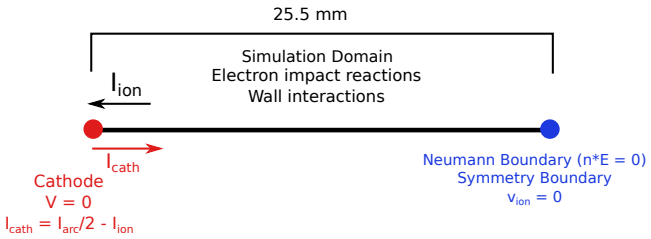

Figure 5.2: Schematic of 1-D plasma model in COMSOL™. Red boundary represents a metal cathode at ground, upon which the emitted electron current from the cathode surface is the arc current subtracted by the bombarding ion current. The blue boundary represents the center of the symmetric Penning ion source with a Neumann boundary for electric field and Dirichlet boundary for ion drift velocity. The black is the domain, whose list of included interactions are shown in table 5.1.

axis. The particle density is also estimated to drop linearly with radius, so that ∇n simplifies to $\frac{n}{R}$. The energy density loss (equation 5.3) is solved assuming linear drops in density from the center, which is where the domain variables (T_e, V, and n_e) are solved for.

The electron-impact collisions included in the model are shown in table 5.1. These include the electron-impact reactions which contribute to the electron continuity and energy equation, as well as the wall impact reactions which turn excited or ionized helium back to the ground state. The latter are based on radial diffusion to the walls. The interactions include the primary source of ionization (and therefore plasma generation) from the heavily-populated ground state of helium. However, as 2^1S and 2^3S excited states are metastable, their lifetimes are long and may lead to relatively large populations which might become another important pathway for ionization. For this reason, the metastable species are included in the simulation by adding the excitation (and de-excitation) process with the ground state, along with ionization of these states. These cross sections are the same used in the CR-model [52]. Other excited states, while important to the internal chemistry of the plasma, will not severely affect the trends in the solved electron temperature and density for various input parameters which is the primary interest

in this thesis. Finally, the ionizations which lead to α particles [81, 82] are found from the NIFS database [83].

The mean escape time for neutral particles is approximated assuming a radial linear density gradient by $\frac{R^2}{2D_n}$, with D_n the diffusion coefficient for the neutral particles. This coefficient is taken from the binary diffusion coefficient for helium solved for automatically in the COMSOL™ plasma module, but with an additional factor for 'free falling' atoms with escape time $\frac{R}{v_{therm}}$. v_{therm} is the thermal velocity of the ions at the gas temperature of 300 K. Then, similar to what is done in section 4.3.2, the total wall impact rate becomes $\left(\frac{R^2}{2D_n} + \frac{R}{v_{therm}}\right)^{-1}$. The volume and surface interactions included in the model are shown in table 5.1.

Reaction	**Type**
e + He $\Rightarrow$ e + He	Elastic
e + He^+ $\Rightarrow$ e + He^+	Elastic
e + He $\Rightarrow$ 2e + He^+	Ionization
e + He $\Rightarrow$ 3e + α	Double Ionization
e + He^+ $\Rightarrow$ 2e + α	Ionization
e + He $\Leftrightarrow$ e + He(2^3S)	Excitation/De-excitation
e + He(2^3S) $\Rightarrow$ e + He^+	Ionization
e + He $\Leftrightarrow$ e + He(2^1S)	Excitation/De-excitation
e + He(2^1S) $\Rightarrow$ e + He^+	Ionization
He(2^3S) $\Rightarrow$ He	Wall Impact
He(2^1S) $\Rightarrow$ He	Wall Impact
He^+ $\Rightarrow$ He	Wall Impact
α $\Rightarrow$ He	Wall Impact

Table 5.1: Reactions and their types in the COMSOL™ model.

For ions, the classical diffusion coefficient based on the helium ion mobility is given by COMSOL™, which is given as a function of electric field. The classical diffusion coefficient across the magnetic field is calculated from these given values (equation 2.22). The wall impact rate is then calculated the same way as for the neutrals for the diffusion component. As it is unclear from the literature whether the ions in such a source would also follow the same Bohm diffusion as electrons, the Bohm diffusion coefficient will also be used as a comparison to see its effects on the plasma model.

At the cathode, the total current must be equal to $I_{arc}/2$ since it represents half the total cathode area. This means that the emitted electron current I_{cath} into the domain must be:

$$I_{cath} = \frac{I_{arc}}{2} - I_{ion} \tag{5.12}$$

where I_{ion} is the ion current bombarding the cathode from the plasma. It is assumed in the case of the cold cathode mode that all emission of electrons from the cathode is due to secondary emission. Secondary emission is when the local Coulomb potential of an ion at the cathode surface causes electrons to escape the cathode and recombine with the ion. In this case, if the work function W_f, or the energy required for an electron to escape a metal, is much lower than the ionization potential of an ion, then an extra electron can be pulled out as well. The work function for graphite is 4.62 eV [84]. The chance of this happening is called the *secondary emission coefficient* γ_i and is usually much less than 1 for most cases [24]. However, this is heavily dependent on the ion energy and the properties of the material's surface. The energy of these secondary electrons (E_{SE}) is assumed to be the leftover energy from the ionization potential (ΔE_{ion}) subtracted by the work function and divided by the amount of released electrons ($E_{SE} = \Delta E_{ion} - 2W_f$). There are also wall impact reactions implemented on the cathode surface, where each excited state and ion on the surface becomes ground-state helium. The cathode wall is made to be perfectly reflecting for the electrons, meaning that an electron that is emitted from the cathode is trapped in the plasma domain.

It is assumed that since I_{cath} comes from secondary emission due to ion bombardment, the current density of electrons emitted from the cathode $\frac{dI_{cath}}{dA_{cath}}$ is proportional to the ion flux towards the cathode where A_{cath} is the cathode surface area exposed to the plasma. Thus the emitted electron current density from the cathode is:

$$\frac{dI_{cath}}{dA_{cath}} = I_{cath} \frac{\frac{dI_{ion}}{dA_{cath}}}{\int \frac{dI_{ion}}{dA_{cath}} dA_{cath}} \tag{5.13}$$

For the 1-D model we have to assume that the ion distribution on the cathode is uniform, and thus equation 5.13 simplifies to I_{cath}/A_{cath}. One should keep in mind

though that the mean free path of an electron entering the domain is still larger than the plasma column. Therefore, we have to take into consideration that many electrons will go through the column without collisions and be absorbed by the cathode at the other end. From the common Beer-Lambert law for attenuation, we can find the capture probability of the emitted electrons as:

$$P_e = 1 - \exp\left(-2\sum_i \int_0^l \sigma_i n_g dx\right) \tag{5.14}$$

where each index i is for each electron-impact interaction, l is the length of the simulation domain, and the factor 2 is used because the electron has length $2l$ to be trapped as only half the simulation domain is used due to symmetry. Since the current at one cathode is the total emitted current subtracted by the current coming from the other side that hasn't been trapped, the net emitted current on the cathode boundary is reduced by the factor P_e. With the assumption of uniform emission along the cathode, the actual emitted current is I_{cath}/P_e.

The PDE of equation 2.13 is applied to the ions by adding the general coefficient form PDE in COMSOL™ from the *Mathematics* module, which allows for the introduction of general PDEs with user selected coefficients. Equation 2.13 was implemented with $\vec{u} \times \vec{B} = 0$ as the dimension we are modeling is along the axis of the magnetic field. We assume the ion temperature to be the same as the neutral gas temperature (300 K), and due to its acceleration in electric fields $\vec{u} - \vec{u_0} \approx \vec{u}$. It is also assumed that this temperature is constant, so that $\nabla p = k_B T \nabla n$. The plasma module comes with data for the helium ion mobility as a function of reduced electric field. The collision frequency is derived from this data by using the relation between the mobility and collision frequency (equation 2.16). As we have no information on α mobility within a helium gas background, we assume that the collision frequency for this particle is that of the singly-charged state multiplied by $\sqrt{2}$. In the collision drift-diffusion case, this makes the drift velocity for the α-particles to be $\times\sqrt{2}$ that of the He^+ ions, which is what we expect from energy conservation in the electric field. A Dirichlet boundary condition of $u_i = 0$ is applied to the center symmetry point of the plasma as we expect the total ion drift here to be zero. As the PDE solves for $\vec{u_i}$ ($\vec{u_i}$ the ion velocity), one must then go through the internal calculations within the plasma module and replace all variables solving for the ion

flux ($\vec{j_k}$ in equation 5.10) with the newly calculated flux from the implemented PDE solver.

The electrons also need an inertial term since they start at zero potential at the cathode and accelerate to high speeds within the sheath, which also generate unrealistically large speeds in the drift-diffusion model. However, adding another non-linear PDE for the electron velocity which then couples with the continuity and energy equation leads to convergence issues within the model. A simpler way to implement this is to add a term in the calculation of electron collision frequency, which is used to calculate the mobility/diffusion terms and consequently the fluid velocity. The plasma module in this case solves for the collision frequency using the sum of all collision frequencies for each interaction between electrons and neutral particles integrated over the local Maxwellian EEDF (equation 2.14). However following the procedure from Lishev [85], the inertial term can be approximated as an additional collision frequency term which is large (and therefore limits the particle speed) within the high electric fields. If we take equation 2.13 at steady state ($\frac{\partial \vec{u}}{\partial t} = 0$) along the magnetic field axis x for electrons we have:

$$\begin{aligned} m_e n_e \frac{\partial u}{\partial x} u &= -e n_e E_x - \frac{\partial p}{\partial x} + m_e n_e \nu u \\ 0 &= -e n_e E_x - \frac{\partial p}{\partial x} + m_e n_e \left(\nu - \frac{\partial u}{\partial x} \right) u \end{aligned}$$

So we effectively have the drift-diffusion equation but with an additional term in the collision frequency of $-\frac{\partial u}{\partial x}$. We approximate this term in the case of collisionless sheaths where $\nu << -\frac{\partial u}{\partial x}$ due to very high fields. In this case, we also assume that the pressure gradient is much less than the electric field component since the voltage drop across the sheath is much greater than the electron temperature in the bulk plasma. The last assumption is that the electron flux velocity at steady state conditions in the sheath is from the maximum kinetic energy an electron can have when released from the cathode due to the voltage gain.

$$\frac{\partial u}{\partial x}\sqrt{2em_e(V_{SE}+V-V_{min})} = -eE_x$$

$$\frac{\partial u}{\partial x} = -E_x\sqrt{\frac{e}{2m_e(V_{SE}+V-V_{min})}}$$

And thus we have the total collision frequency as:

$$\tilde{\nu_{en}} = \nu_{en} + E_x\sqrt{\frac{e}{2m_e(V_{SE}+V-V_{min})}} \tag{5.15}$$

where V_{SE} is the energy in eV of the electrons emitted due to secondary emission, which is assumed to be 15.35 eV. V_{min} is the minimum voltage in the domain, which is 0 V at the cathode. This makes it so that when ν_{en} = 0, the speed of the electrons is capped for an electron with kinetic energy equal to what is gained from the electric potential. So all that is required is for ν_{en} in the COMSOL™ calculation to be replaced with the modified $\tilde{\nu_{en}}$.

It should be noted that the spatial mesh on which the PDEs are solved gets finer near the cathode where the high voltage sheath is expected to be. This is done to better resolve the high gradients in voltage and particle densities within this region.

5.3.1 1-D Results

The 1-D model requires an input of parameters actually observed from the PIG source, which are taken from the experimental sweeps discussed in the previous section (figure 4.23 and 4.24). To show the basic features of the PIG source using the 1-D model, a simulation is run for input parameters of 20 sccm, 0.05 T, and 1.5 kV which corresponds to an arc current of 10.08 mA. This corresponds to a high pressure and low magnetic field regime, which is closest to the type of plasmas that can be ideally modeled with the COMSOL™ plasma module. Figure 5.3a shows the results for the calculated kinetic energy over charge of the ions compared to the maximum energy gain possible from the electric potential. A similar plot is shown for the electrons in figure 5.3b. The blue line corresponds to the total possible kinetic energy of the electrons V + V_{cath} + T_e. Here the kinetic energy components are separated into two different drift components which come from the electric

field via the mobility and the density gradient via diffusion, as shown in equation 5.2. Near 5 mm where there is a sharp drop in voltage along the cathode sheath, and hence a large energy gain for both particles, we see the particles have velocities that correspond to kinetic energies far above what is possible based on energy gain from the electric fields (no other power deposition is included in the model). This shows the primary issue with a drift-diffusion model in low pressure DC discharges which rely on large static fields for plasma operation. This is because the mean free path for these particles at high speeds becomes larger than the size of the sheath, so many particles do not undergo collisions. This is why the inertial term in the particle momentum equation, which is neglected for drift-diffusion equations, is necessary in these regions.

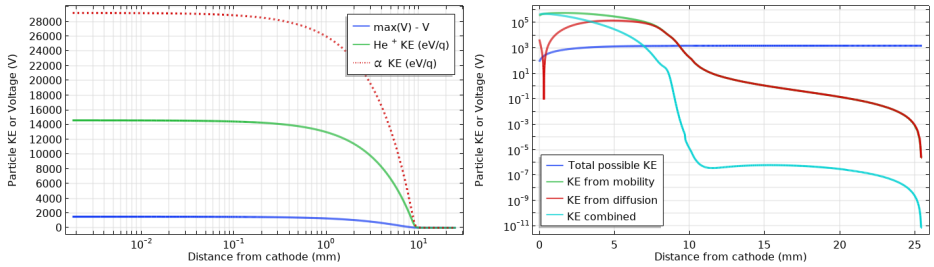

(a) Ions KE **(b)** Electron KE

Figure 5.3: Ion and electron kinetic energy calculated from $\frac{1}{2}mv^2$, where v is calculated from the drift velocities, as a function of the potential energy gain in voltage along the source length for the 1-D model using only the standard drift-diffusion equation. The electron is separated into drift velocities from its mobility and diffusion terms.

Figure 5.4 shows the results when the additional PDE for the momentum equation is included for the ions, in addition to the inertial term approximation added to the electron collision frequency. We see in this case the ion energy (figure 5.4a) from the drift is less than the maximum possible from the energy gain in the electric field, which presents a much more realistic picture of the plasma process. However, one should keep in mind that the energy equation is not solved for heavy particles, so it is still assumed that the temperature always stays the same. The same restriction applies to the electrons in figure 5.4b, whose derived kinetic energy from the mobility and diffusive drifts are also less then the maximum allowed. Since

the drift velocities are normally countering each other, the kinetic energy from the total drift velocity is shown in cyan, which either matches or is below the maximum allowed. So using a rather simple assumption, the drift-diffusion model for electrons can be significantly improved.

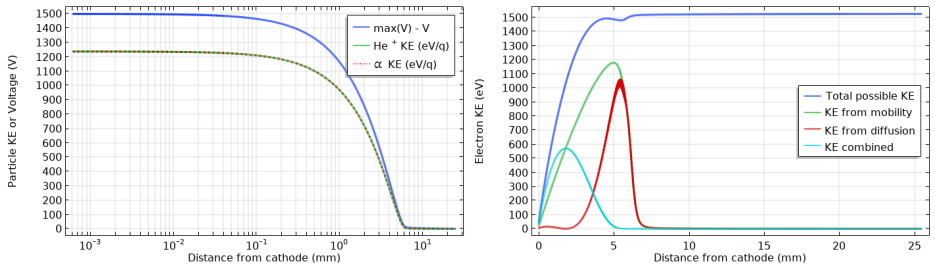

(a) Ions KE **(b)** Electron KE

Figure 5.4: Ion and electron kinetic energy calculated from $\frac{1}{2}mv^2$, where v is calculated from the drift velocities, as a function of the potential energy gain in voltage along the source length. This is for the model with additional momentum equation for ions and an approximation of the inertial term from the electron momentum equation added to the collision frequency.

Figure 5.5 shows two scales, particle density and voltage as a function of distance from the cathode, on a log-log scale. All the qualitative aspects of the model are as expected for a DC discharge for a Penning ion source. As expected from literature reviews, most of the voltage drop in the plasma is across a small distance near the cathode. All densities are peaked at the center of the discharge, and drop drastically within the sheath. The electron density falls at a greater rate due to the differences in particle mass, and therefore speed, within the sheath. This difference in negative/positive particle density is also what creates the large voltage drop near the sheath. However, the electron density does start to increase within a mm of the sheath heading towards the cathode. This is because the electrons start with very little energy on the cathode wall, and hence need a larger density to reach the appropriate current density to sustain the arc current I_{arc} on this electrode.

The electric potential within the plasma peaks within the center of the discharge, and is lower than the arc voltage, though by only about 0.5 V. This means the electron current to the anode is very weakly dependent on the radial electric

field pushing the electrons out, and mostly comes from radial diffusion within this model.

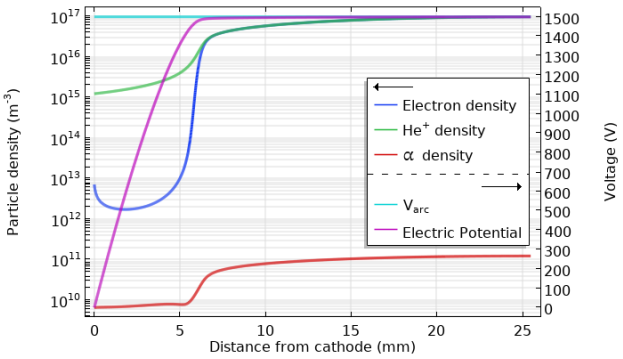

Figure 5.5: Charged particle densities and voltage as a function of distance from the cathode. The particle densities shown are for electrons (dark blue), He^+ (green), and α (red) particles. On the voltage scale is the electric potential in the plasma (cyan) and the total arc voltage (or anode potential, purple).

Figure 5.6 shows the electron temperature and ionization rate constants for ground state and singly-ionized helium atoms. The electron temperature increases significantly within the sheath due to the energy gain from the electric field and the energy gain from the diffusing electrons from the bulk plasma. As the electron temperature rises, more electrons are within the high energy tail of the Maxwellian EEDF with energies above the ionization threshold, which results in a maximal ionization frequency. However, since the ionization rate has an additional multiplicative factor of n_e, the rate actually peaks near the center of the discharge despite the lower electron temperature plateau. This is why for both ionization rates, there is a slight dip after the peak electron temperature, where the electron density is still not high enough to overcome the lower electron temperature.

5.3.2 Applied 1-D Model

The 1-D model is applied for all measured operational parameters for the cold cathode Penning ion source seen in figure 4.23 and 4.24. For each solution corresponding to a set of operational parameters for the Penning ion source, the average

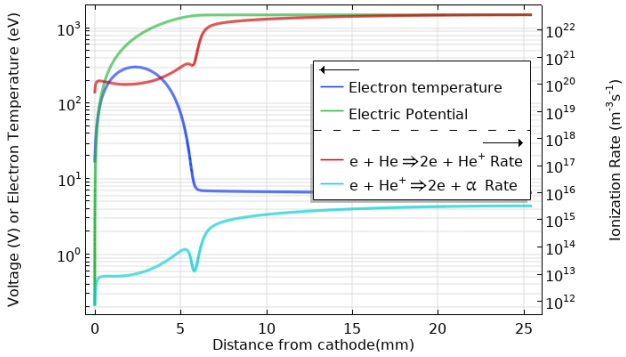

Figure 5.6: Electron temperature and ionization rate for He→He$^+$ and He$^+$ → α as a function of distance from the cathode.

electron density and temperature is calculated from the edge of the domain (Neumann boundary representing half the ion source length) to 5 mm within the plasma domain. This corresponds to the region of the ion source that the OES measurement collects emitted light from, and is thus the region of interest for comparing to the trends seen with the OES.

As we are not sure which diffusion and mobility coefficients best represent the dynamics of the charged particles across the magnetic field, we solve the model using various mobility and diffusion coefficients for the electrons and ions. The ions are typically assumed to have classical diffusion coefficients. However, analytical models on similar discharges solved by Chen [61] shows that the potential dip seen in most reflex discharges (essentially Penning discharges) is best fit by a model with ions diffusing with the Bohm diffusion coefficient, but the mobility still taken at the classical value. In general, it is unknown whether the pressure is low enough for the ions to be fully magnetized and therefore undergo the same E×B drifts across the magnetic field due to plasma instabilities. For this reason, models are also run with the ion diffusion coefficient set to the Bohm diffusion as done by Chen, which is larger than the classical diffusion due to the higher electron energy $T_e >> T_{ion}$.

Thus we have three different sets of diffusion and mobility coefficients we solve for. The first is with the electrons and ions following the classical equation

for cross field diffusion and mobility (equation 2.23 and 2.24). The second case is where instabilities cause electrons to have mixed mobility and diffusion (equation 5.9), but the ions are still assumed to be unmagnetized with gyro-radii larger than local perturbations, therefore keeping classical diffusion. The last case is where ions are magnetized enough to be transported in these E$\times$B drift instabilities, and therefore have Bohm diffusion. The electrons in this latter case still have mixed mobility and diffusion.

The results of the averaged T_e and n_e as a function of varied operational parameters are shown in figure 5.7. The case of electrons and ions both having classical mobility and diffusion is labeled 'Classical'. The case of electrons have mixed mobility and diffusion but the ions are still classical is labeled 'Mixed Mob.'. The last case is where the electrons have mixed mobility and ions follow Bohm diffusion is labeled 'Mixed Mob. w/ Bohm'. We see that when compared to figure 4.27, all the general trends in electron density and electron temperature as a function of each operational parameter are the same except for when varying arc voltage. Thus the electron density increases for an increase in each operational parameter, while the electron temperature decreases, as seen in the OES measurements.

The reasoning for each remains the same. When gas flow increases, each electron has greater probability of interaction with a neutral particle which leads to greater ionization and thus electron density. These increased energy-exchange interactions also cause the electron temperature to decrease. This is also essentially what happens with the magnetic field increase, except in this case the increased magnetic field forces greater amount of electron interactions through plasma confinement, which then reduces the electron temperature through greater energy exchange reactions. This is why the electron density increases and electron temperature decreases when classical transport is used compared to the mixed mobility model.

What is interesting is the case of a varying arc voltage. An increase of electron density is unsurprising due to greater ionization per primary electron. However, the decrease in temperature seen in the OES measurements (figure 4.27b) is unexpected due to the increased energy for each electron. The 1-D simulations (figure 5.7d) show an essentially flat electron temperature dependence. The reason becomes clear when looking through the simulations, where one will notice that the

inelastic power loss increases with arc voltage. This means that the magnetic confinement is high enough so that each primary electron from the cathode will lose most of its energy to collisions before being dumped on the anode wall, regardless of the energy increase of these primary electrons due to an increasing arc voltage. In addition, each primary electron generates an 'avalanche' of secondary electrons for each ionization, each of which undergoes their own inelastic collisions. This means that the remaining kinetic energy, after taking into account all the inelastic collisions, is spread out among a larger number of electrons assuming many of these collisions are ionizations. Thus the average energy per electron at equilibrium (the electron temperature) can be kept constant or decrease as arc voltage is increased. This allows for the overall temperature to actually decrease in the 1-D model, though almost negligibly compared to what we see from the OES measurements. This suggests that in reality, there is a greater increase of total inelastic collisions per primary electron as arc voltage is increased. This would result in the more severe decrease in electron temperature measured by the OES. The odd minor jump in electron temperature from 1.8 kV to 2.0 kV in the 1-D model corresponds to a relatively constant arc current (figure 4.23b). This means the electron density stays about the same, resulting in the higher energy of the primary electrons at 2 kV being less diluted among a similar electron population. This is why we see a slight increase in temperature within the simulation.

The same simulations were run for the low pressure and high magnetic field mode. These simulations could not be run using classical cross-magnetic field transport for the charged particles due to convergence issues. This is likely because the confinement for electrons is too high at such large magnetic fields, where plasma instabilities may lead to anomalous diffusion. Hence why these simulations only use the 'Mixed Mob.' or 'Mixed Mob. w/ Bohm' option. It should be mentioned that the 2 sccm gas flow case could not be simulated due to convergence issues at such low gas pressures. The results of these simulations are shown in figure 5.8. The constant parameters for each variation are: 1.4 kV and 0.4 T for gas flow, 4 sccm and 0.39 T for arc voltage, and 4 sccm and 1.45 kV for magnetic field.

We see that the plasma parameters have the same trends as in the high pressure low magnetic field case for all the same reasons. However, figure 4.28c shows the odd trend of a sudden increase in electron temperature and decrease in elec-

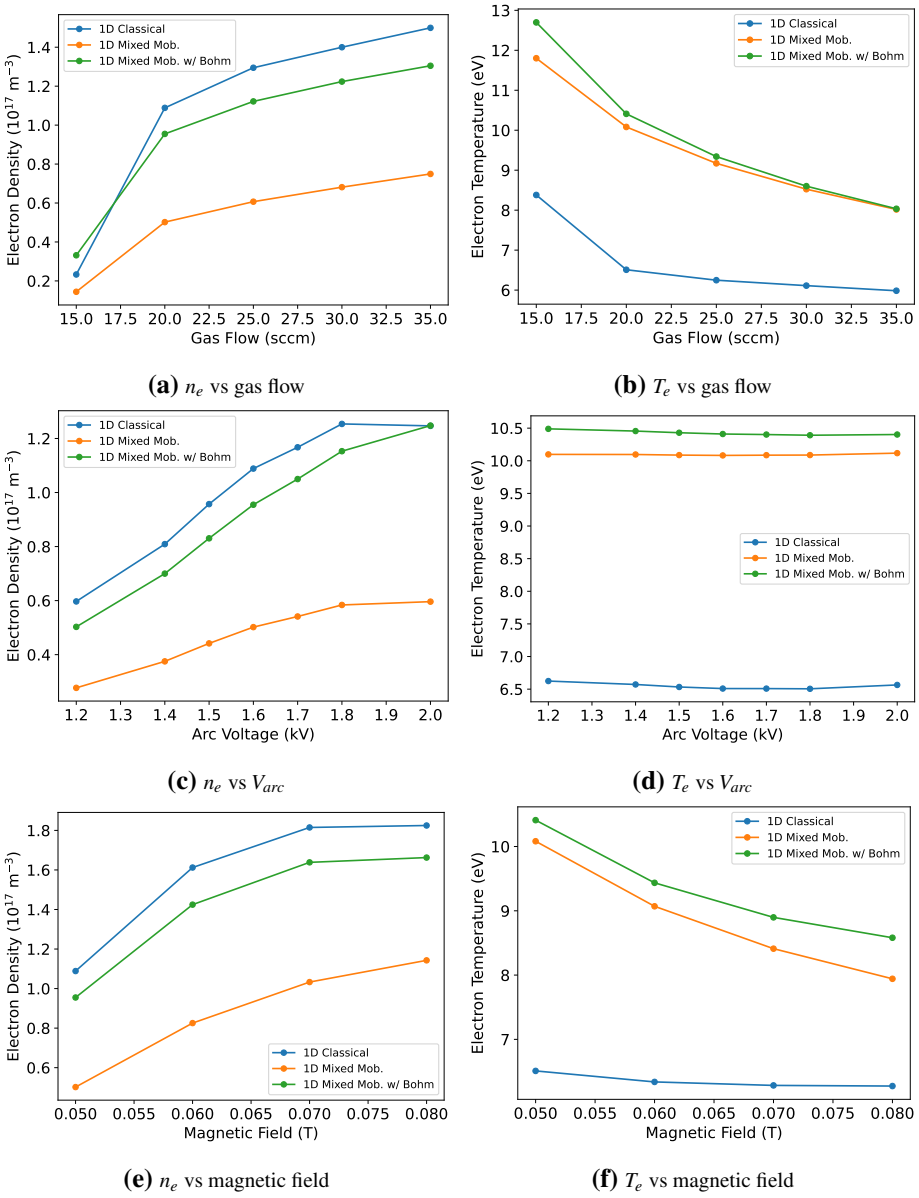

(a) n_e vs gas flow

(b) T_e vs gas flow

(c) n_e vs V_{arc}

(d) T_e vs V_{arc}

(e) n_e vs magnetic field

(f) T_e vs magnetic field

Figure 5.7: n_e and T_e as a function of (a,b) gas flow, (c,d) V_{arc}, and (e,f) magnet field strength in the high pressure low magnetic field regime. Plasma parameters taken as average in 10 mm of source. Solved for various sets of mobility and diffusion coefficients for electrons and ions.

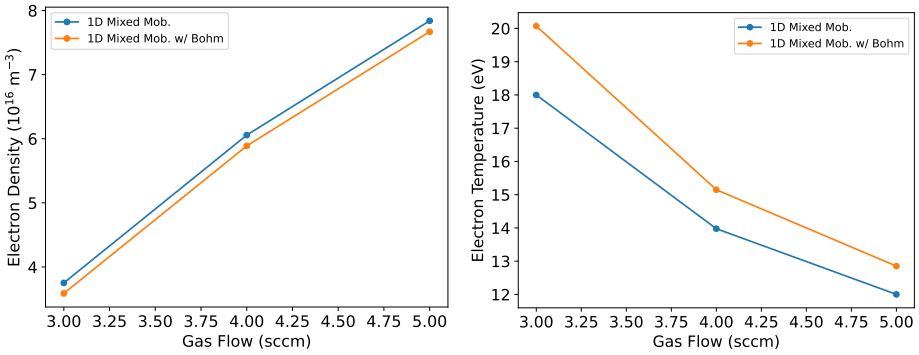

(a) n_e vs gas flow

(b) T_e vs gas flow

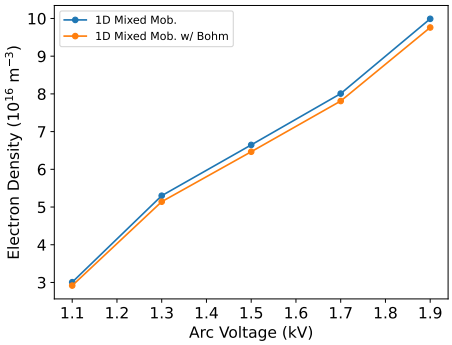

(c) n_e vs V_{arc}

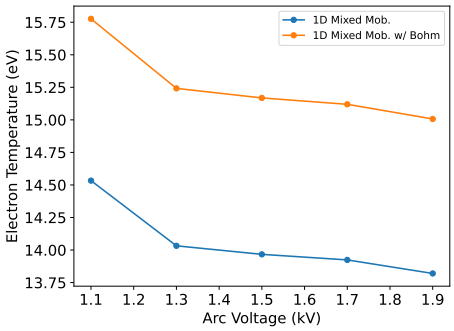

(d) T_e vs V_{arc}

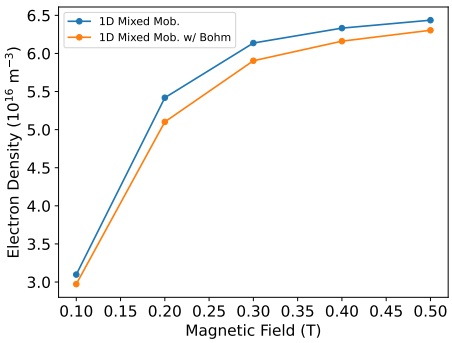

(e) n_e vs magnetic field

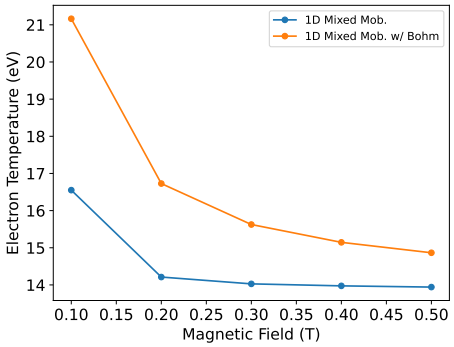

(f) T_e vs magnetic field

Figure 5.8: n_e and T_e as a function of (a,b) gas flow, (c,d) V_{arc}, and (e,f) magnet field strength in the low pressure high magnetic field regime. Plasma parameters taken as average in 10 mm of source. Solved for various sets of mobility and diffusion coefficients for electrons and ions.

tron density past 0.3 T as measured by the OES diagnostic. This corresponds to a flattening of density (figure 5.8e) and temperature (figure 5.8f) within the 1-D model. Hence we see that the model cannot explain this measurement by the OES. As mentioned before, this effect is likely due to either introduction of severe instabilities or the effect of the bowing of magnetic field, either of which would lead to lesser confinement of the electrons. In general, when compared to the experimental OES measurements, the simulated densities are up to a factor of 5 lower than measured with the OES, and the temperature up to a factor 2 lower.

The cold cathode discharge should generally have secondary emission coefficients of less than 0.3 for singly charged helium ions [24]. As the 1-D model solves for the current at the cathode self-consistently, the secondary emission coefficient can be calculated by dividing the emitted electron current on the cathode boundary by the capture probability integrated along the entire domain length, or I_{cath}/P_e. P_e uses equation 5.14 for electron-impact interactions with ground state state helium, which are the most probable reactions. An example of the calculated secondary emission coefficient is shown in figure 5.9.

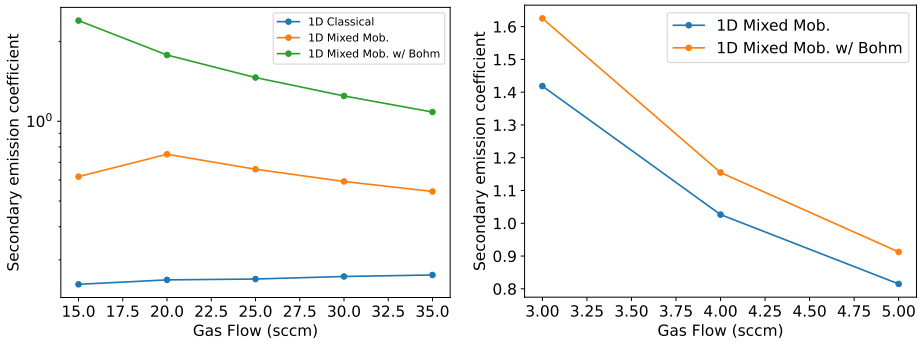

(a) High pressure low magnetic field

(b) Low pressure high magnetic field

Figure 5.9: Calculated secondary emission coefficient at cathode boundary for 1-D model as function of gas flow at (a) high pressure and low magnetic field and (b) low pressure and high magnetic field.

We see that using classical transport in figure 5.9a outputs secondary emission coefficients closest to what is expected at less than 0.3. However, the introduction of transport due to anomalous diffusion makes it much higher. While this might

lead us to believe that using classical transport coefficients is the best model, this might not be the case. It has been determined that plasma instabilities can actually significantly improve the capture efficiency of primary electrons up to 50% [60], compared to a maximum of about 5% calculated in the low pressure case. This means P_e might be up to an order of magnitude higher, which would decrease the calculated secondary emission coefficient up to a factor 10, giving the expected range for secondary emission coefficients. Thus one cannot determine the best model based on this criteria.

5.3.3 Charged-Particle Tracing Ionization

One issue with the fluid or drift-diffusion model is that the electrons are assumed to be Maxwellian. This means that it is assumed all electrons everywhere in space are defined by this isotropic temperature distribution, and any change in local temperature from the pressure gradient or local electric field does not change this distribution. In reality however, especially within the sheath, it is expected that the electrons have energy corresponding to the gain in voltage from the cathode and with velocity component mostly along the electric field parallel to the magnetic field. This is therefore a highly non-isotropic case. For this reason, it is expected that simulations will underestimate electron flow along the magnetic field direction, as in reality there will always be fast non-colliding electrons with energies close to the electric potential gain relative to the cathode.

To show how these fast electrons from the sheath change the plasma properties from the steady state 1-D plasma model, a 2-D model using the charged particle tracing (CPT) module from COMSOL™ is made for the high pressure and low magnetic field case of 20 sccm, 1.5 kV, and 0.05 T. The simplified schematic of this model is shown in figure 5.10. It is composed of a rectangle with dimensions 25.5 mm $\times$ 8 mm in an (x,y) coordinate grid to represent half of the discharge length from the 1-D plasma model. Within this domain, the solution to the voltage, electron density, electron temperature, and ion density from the 1-D plasma model (solved using classical mobility and diffusion across the magnetic field) is projected along the domain length. One end of the domain is a wall that emits uniform electrons with current equivalent to the solution of the total secondary electron

current (including dividing by the capture probability P_e) from one cathode in the plasma 1-D model, which is 1.24 mA and is represented by 5000 macroparticles. The charged particle tracing module has a *specify current* option, which allows each macroparticle to represent a current of particles per second. This is done by giving each particle a *release frequency* parameter, which represents the release frequency for each particle at the cathode $f_{rel} = \frac{I_{cath}}{eN_p}$ where N_p is the number of macroparticles. This allows for the calculation of parameters which rely on the integrated value of particle rates within a mesh, such as space charge which is the collection of charged particles in a mesh volume integrated over time.

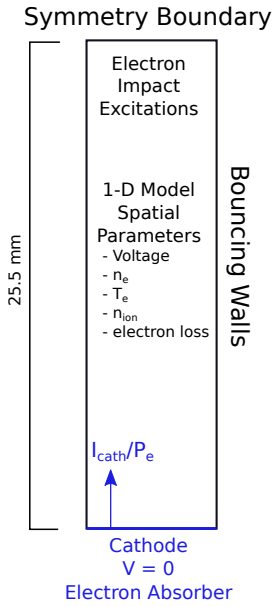

Figure 5.10: Schematic of 2-D CPT model in COMSOL™. Blue boundary is the cathode boundary where electron macroparticles are emitted into the domain. The other walls are bouncing (induce perfect elastic collisions). The domain along the ion source length from the 1-D model is projected onto this model along the length, with parameters of voltage, electron/ion density, electron temperature, and electron loss rate used.

The electrons within the domain can interact with a background gas of ground

state helium, whose particle density is set to the average from the 1-D plasma case (2.493×10^{21} m^{-3} at 20 sccm) and temperature set to 293.15 K. Only ground state helium is included since it's the dominant source of electron impact interactions due to its large population density. These interactions from the ground state are the same as in the 1-D plasma model, which includes ionization, excitation to 23S and 21S states, and elastic collisions. Ionization collisions in this module assume that the secondary electrons produced have zero energy, and the primary electrons have the remaining energy and inherit the macroparticle release frequency. There are also elastic collisions with the background electrons and ions (with density taken from 1-D plasma model) with cross section from the Coulomb cross section also used in the 1-D plasma model. The temperatures of the ions are assumed to also be 293.15 K, and the electron temperatures are taken from the plasma 1-D model.

In order to take into account the loss of electrons, an artificial attachment collision node is added which eliminates particles based on collision frequency. In this case, the electron loss rate as a function of discharge length from the 1-D plasma model is used, which has a minimum frequency of 3.74×10^5 Hz. This means a $\approx$10 μs simulation time is needed to get an approximate equilibrium solution, as this would leave about 2% of the original emitted particles.

The cathode (where electrons are emitted) is programmed so that any electrons that come back in are absorbed and taken out of the domain. The other three walls are set to perfectly bounce any electrons off the walls. For the discharge length walls (representing the anode walls), we assume that a magnetic field will confine electrons until lost by the loss rate set from the plasma 1-D model, therefore they are not absorbing. As a result, the CPT simulation needs to be 2-D to include scattering of electrons into the plane perpendicular to the magnetic field after undergoing a collision. This allows us to observe the effects of possible anisotropy of the electron velocities. On the top symmetric boundary (representing the center of the source), this is bouncing because it's assumed that any electron that escapes results in a 'mirror' electron coming in from the other side.

The simulation is run over 10μs in order to make sure that the electrons reach approximate equilibrium. This simulation takes 8.5 hrs to run. The electron capture percentage of the initial beam is 17.48%, compared to 15.83% from the plasma 1-D model, showing good similarity between simulations. Accumulator nodes are

used which sum up macroparticle parameters for each macroparticle that is within a mesh grid within some unit time. The integrated variables are electron energy, particle count, and ionization frequency. This is essentially done by integrating the rate for each macroparticle parameter, which is the parameter multiplied by the release frequency, over time. Each parameter can then be projected onto the discharge length by averaging along the x-axis.

Figure 5.11 shows the normalized ionization rate (normalized to value at the center of the discharge) from the CPT simulation and the 1-D plasma simulation. The ionization rates are from ground state helium and from He^+. It should be mentioned that the change of this rate over the last 9 - 10 μs is minimal, showing that the values are at an approximate equilibrium. The ionization frequency from the ground state is much flatter over the domain than in the plasma 1-D case, which shows a key component missing in the fluid model. The increased ionization after the sheath compared to the center is because the discharge ionization is significantly impacted by the constant flux of fast electrons with energies higher than the local Maxwellian temperature. This means that even as the electrons start to reach an equilibrium, there will always be a dominant contribution within the domain from fast electrons, which implies a non-Maxwellian distribution as expected from such ion sources. It's also interesting to notice that the peak seen at around 0.4 mm is due to the energy of the electrons at this location corresponding to the maximum cross section for ionization. For the case of ionization of ions to α-particles, the ionization rate does not have a plateau as it is dependent on the local background density of ions which increases as one gets closer to the discharge center. However, it is also higher than in the plasma 1-D model due to the contribution of higher energy primary electrons from the cathode.

Figure 5.12 shows mean electron energy derived from the CPT simulation and the 1-D plasma simulation. The mean elecron energy from the CPT simulation is derived by dividing the total integrated electron kinetic energies by the integrated electron number (integrated sum of macroparticles) to get the mean kinetic energy. This is separated into the portion of kinetic energy parallel and perpendicular to the magnetic field. We see that the mean energy from the CPT model, which has reached close to its equilibrium value, has the same general shape as from the plasma 1-D model, but the portion parallel to the magnetic field is much larger

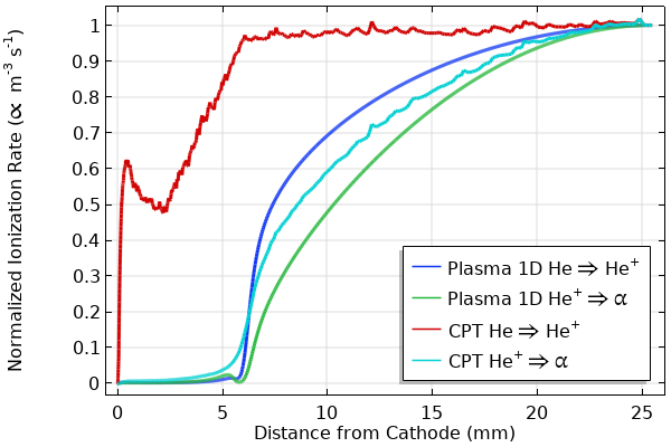

Figure 5.11: Normalized ionization rates along the discharge length from the charged particle tracing simulation and the plasma 1-D model.

than the portion perpendicular. This is again because of the high energy contribution from the fast electrons before they reach equilibrium, which means not only is there likely a non-Maxwellian distribution with high energy electrons at equilibrium, but this distribution is highly anisotropic. The higher temperature along the magnetic field is due to the smaller scattering angle of electrons at higher momentum, thus it takes many collisions for electrons to be scattered perpendicular to the magnetic field. This might contribute to the decrease in electron temperature with arc voltage observed in the PIG source, since an increased arc voltage leads to higher energy (thus higher momentum) electron beams which require more collisions to get sufficient momentum perpendicular to the magnetic field to escape to the anode walls. Note that this simulation only takes into account two dimensions, so the amount of anisotropy likely changes in 3-D. We also see that the mean electron energy drops as we get closer to the center of the discharge, which is due to the electric potential continually pushing electrons toward the center where they lose more energy through collisions.

Figure 5.13 shows the normalized electron density derived from the CPT simulation and the 1-D plasma simulation. The CPT electron density is derived by dividing the integrated macroparticle number by the local mesh area, and is averaged

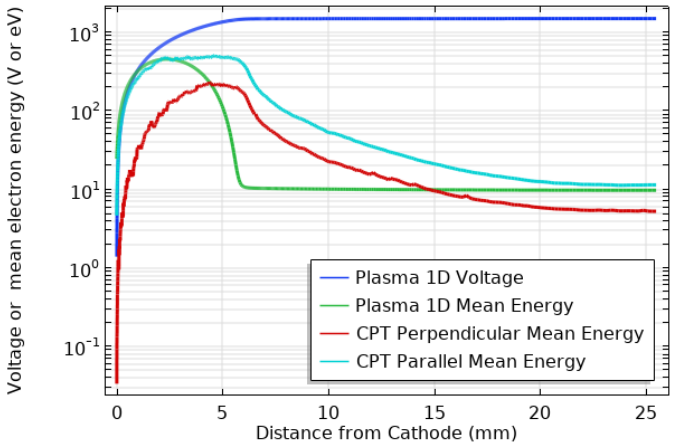

Figure 5.12: Mean electron energy from the CPT simulation and plasma 1-D model, along with the electric potential from the plasma 1-D model.

along the x-axis. The plasma 1-D and CPT models again follow similar shapes, but because of the higher ionizations close to and within the sheath, the electron density in these areas is much greater in the CPT model. This would likely change the potential distribution of the plasma as well since this changes the local space charge contribution of the electrons. This would require a full PIC-MC (Particle-in-cell Monte-Carlo) code to take into account the self-consistent electro-magnetic field changes.

It is clear from the CPT simulations that the plasma 1-D model neglects a core part of power deposition (via inelastic collisions) in the plasma from high-energy electrons. This unfortunately is not implemented into the COMSOL™ plasma models, and adding additional electron kinetic equations would require significant re-development of the model. Thus we have to be wary of this limitation when evaluating the results of these simulations.

5.4 2-D Axi-Symmetric Model

The 1-D model, while significantly improved upon with respect to the standard drift-diffusion model, is still lacking detail in the dimension across the magnetic field. However, there may be important radial effects that change the trends we

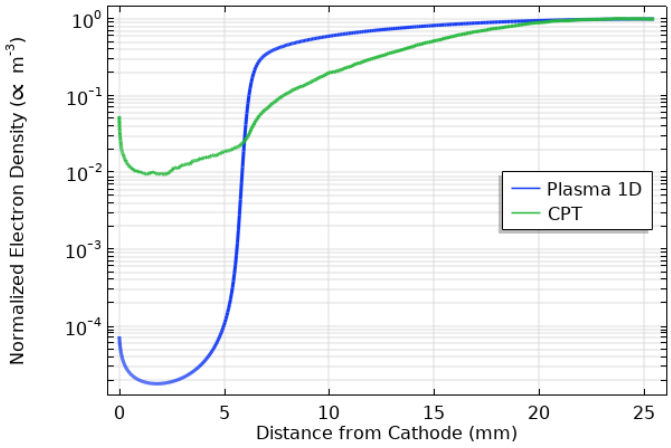

Figure 5.13: Normalized electron density from CPT simulation and plasma 1-D model, along with the electric potential from the plasma 1-D model.

might see when varying input parameters on the ion source. For this reason, it is necessary to increase the dimension of this model to include the radial dependence of plasma parameters within the discharge. For this, an axi-symmetric model of the Penning ion source is developed using the drift-diffusion plasma module in COMSOL™. Though in principle anomalous diffusion is based on azimuthal ($\hat{\theta}$) asymmetries, we solve for the $\hat{\theta}$-averaged plasma parameters which leaves us with the $\hat{z}$ and $\hat{r}$ dimensions.

The simplified schematic of this model is shown in figure 5.14. In order to avoid the high energy particles in the sheath, which would necessitate additional non-linear momentum equations within the model for both dimensions resulting in convergence issues (at least when attempted by this author), a boundary is added which represents the edge of the cathode sheath. At this boundary, electrons are emitted with a flux (particle flux $\vec{n} \cdot \Gamma_e$ and energy flux $\vec{n} \cdot \Gamma_\varepsilon$) corresponding to the flux necessary to satisfy the arc current constraint. The assumption is that the sheath is non-collisional for the fast electrons. This means the steady-state current density of electrons at the cathode is the same as that on the sheath edge, which is typically the case in discharges and is what is seen in the 1-D model. It is

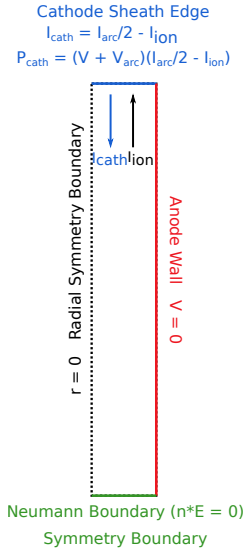

Figure 5.14: Simple schematic of the 2-D axi-symmetric plasma model. The blue line is the edge of the cathode sheath where an input electron particle flux energy flux is applied. The green line is the Neumann boundary which represents the center symmetry boundary point of the Penning ion source. The red line is the anode wall at ground. The dotted line is the r = 0 axi-symmetric boundary.

assumed that secondary emission is the dominant process due to the cathode being cold, and thus the electron flux is proportional to the ion flux onto the domain (see equation 5.13). It is assumed that the energy gain of each electron is the voltage drop within the sheath. This means $\Gamma_\varepsilon = (V_{arc} + V_b) \cdot \Gamma_e$, where V_b is the voltage on the sheath edge boundary. In addition, it is assumed that for every ion which hits the boundary, there is recombination at the cathode surface which produces a neutral ground helium particle going inside the bulk plasma. The flux of the He^+ ions into the boundary, which is assumed to be the primary ion flux, is considered to be $\Gamma_i = n_i v_{Bohm}$ where v_{Bohm} is taken as the ion Bohm velocity shown in equation 2.25. Therefore the ion current I_{ion} is this flux integrated along the boundary multiplied by the single ion charge. It should be mentioned that the 1-D model does show

an ion velocity of about v_{Bohm} at the sheath edge, and so this boundary, which is a typical boundary condition for the sheath in plasmas, is expected to be a good approximation. The metastable states are also assumed to be de-excited to the ground state when colliding with any wall.

The flux of ions and electrons on the anode wall in COMSOL™ is the product of the mean thermal velocity and the particle density on that boundary. In addition, there is also mobility-based migrations of charged particles to the wall by the electric field, if the field is pointing in the correct direction. In order for the solver to reach a steady state, the sum of the electrical currents from the charged particle at the anode wall or cathode edge must be equal to half the arc current. The green boundary is simply a Neumann boundary which keeps the electric field perpendicular to this boundary at 0. This establishes a symmetry at this boundary, which allows us to model only half the full ion source.

The bulk electron interactions within the plasma module are the same as shown in table 5.1, with the collision frequencies dependent on the local Maxwellian temperature of electrons. Like in the 1-D model, the collision frequencies are used to compute the mobility and diffusion of the electrons along the magnetic field. The existence of the magnetic field turns these coefficients into tensors. The mobility and diffusion across the magnetic field for electrons uses either classical or mixed mobility.

The model was purposely chosen to be a simple rectangle representing the primary plasma column so that the mesh can divided into rectangular squares, which simplifies the computation and allows for easier convergence. Like in the 1-D model, the mesh is made much finer closer to the walls where we expect larger particle density gradients. As these gradients are expected to be much smaller near the middle of the discharge, they are allowed to be coarser within these regions. The largest mesh area at the border of the symmetry boundary and r=0 boundary is 0.05 mm by 0.11 mm, and the smallest mesh at the corner of the cathode edge and anode wall is less than 0.001 mm by 0.001 mm. The fine mesh is especially important at the anode wall because the wall condition for the electrons is based on thermal motions of the electrons, which can only happen if the mesh size is smaller than the gyroradius of the particle in the magnetic field.

5.4.1 2-D Model Results

Example plots of the electron density, electron temperature, and electric potential for high pressure low magnetic field operation (20 sccm, 1.5 kV, 0.05 T) is shown in figure 5.15. This is for the case of classical transport across the magnetic field for the charged particles. The cathode sheath edge boundary is the top, while the symmetric Neumann boundary is the bottom. Though it's difficult to see in a 2-D mesh-plot, the electron density actually peaks between the middle of the ion source and the cathode sheath, unlike in the 1-D model. This becomes worse at higher gas pressures. This is likely because in the drift-diffusion model the sheath boundary only describes the electron flux ($v_e n_e$) and energy flux, but does not specify the actual speed of the electrons since the momentum equation is not solved for. Therefore the self-consistent model can generate electrons with lower drift velocity but higher electron density which do not penetrate as deeply within the plasma before diffusing radially. However, the overall flux of electrons and the energy they give to the plasma does not change, thus the effect of the input parameter variations on the overall bulk plasma parameters should not change significantly. The electron temperature is highest near the sheath edge where there are high energy electrons, and peaks near the center due to the greater amount of collisions in the center. This is also seen in the 1-D model. The electric potential has a typical positive voltage with respect to the anode like in a non-magnetized plasma, which is surprising as many PIG sources typically have negative electric potentials with respect to the anode. This is because the much higher electron temperature allows the diffusion of the electrons to still be higher than that of the ions, which allows for a positive sheath potential.

Example plots of the electron density, temperature, and electric potential for low pressure high magnetic field operation (4 sccm, 1.45 kV, 0.4 T) is shown in figure 5.16. This is for the case of anomalous transport across the magnetic field for the charged particles (mixed mobility electrons, Bohm ion diffusion). In this case the electron density is peaked near the center because of the higher mobility (and thus drift velocity) of the electrons in a lower pressure background gas. The electron temperature however is actually peaked at the edge of the discharge near the anode wall. This is because of an overall gain of electron energy from the center

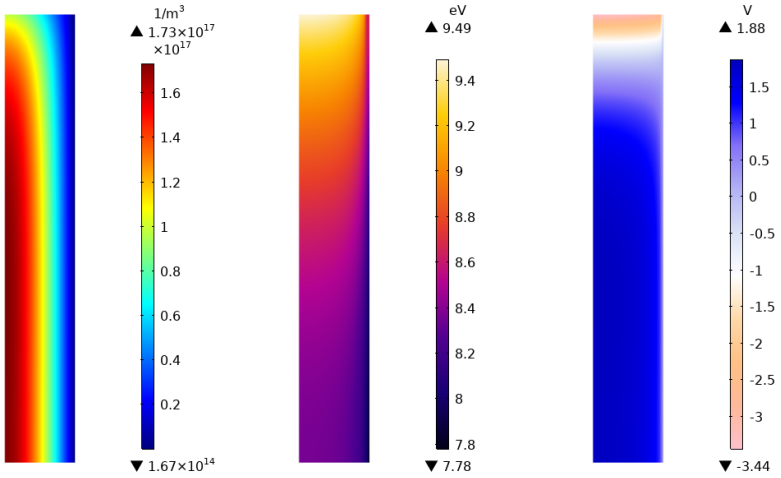

(a) Electron Density **(b)** Electron Temperature **(c)** Electric Potential

Figure 5.15: Example plots of a) electron density b) electron temperature and c) electric potential within the 2-D plasma model for parameter of 20 sccm, 1.5 kV, and 0.05 T. Solved with classical transport for electrons and ions. See figure 5.14 for a visual reference of boundary conditions.

to the anode wall from the negative voltage dip with respect to the anode, which is more typical of low pressure Penning discharges. This is required due to the increased confinement of the electrons due to reduced electron-neutral collisions and increased magnetic field strength, which thus requires an electric field that pushes the electrons mostly in the center of the discharge out to the anode to sustain the arc current constraint.

To see how the different mobility and diffusion coefficient settings changes the radial profiles of the primary plasma properties, we need to plot the radial profiles of these properties for each setting. To get the profile for the primary plasma properties as a function of radius, these parameters are projected unto the radial axis by averaging along the discharge length (z-axis). This is done for the ion density, electron temperature, and electric potential. It should be noted that due to quasi-neutrality, the primary ion and electron densities are essentially the same throughout the discharge except within the thin sheath near the anode wall. The resultant averaged parameters are shown in figure 5.17.

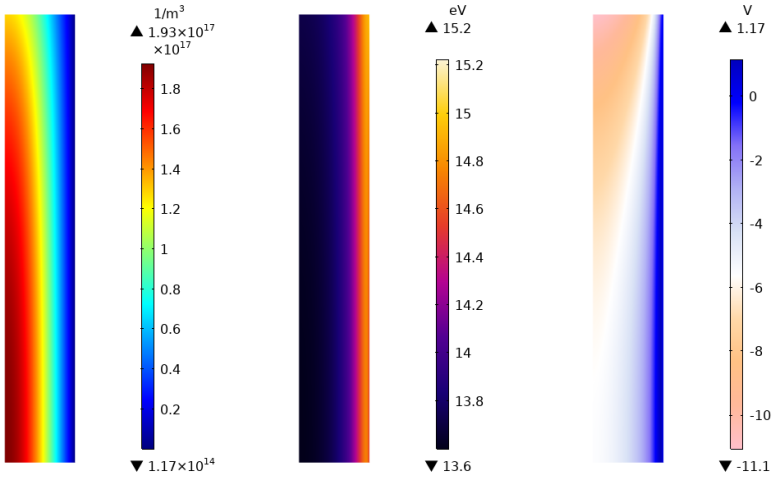

(a) Electron Density **(b)** Electron Temperature **(c)** Electric Potential

Figure 5.16: Example plots of a) electron density b) electron temperature and c) electric potential within the 2-D plasma model for parameter of 4 sccm, 1.45 kV, and 0.4 T. Solved with anomalous transport for electrons and ions. See figure 5.14 for a visual reference of boundary conditions.

From figure 5.17a, we see that the ion density is peaked when using classical transport coefficients, since these coefficients are smallest for a certain magnetic field strength and thus leads to reduced loss of the ions (and electrons) to the anode wall. It also corresponds to a better electron confinement which leads to more ionization of the ground state helium within the discharge, and thus to a lower electron temperature due to greater energy loss from collisions in figure 5.17b. Increasing the radial electron mobility (Mixed Mob.) leads to less confinement and thus less ionization and energy loss, leading to decreased ion production and increased electron temperature. Adding Bohm diffusion to the ions increases their diffusion to the anode walls, which decreases the electric potential (due to less positive space charge) and therefore allows the electrons to diffuse faster, which further reduces confinement. This results in further decrease of ion and electron density, and greater electron temperature, when compared to the Mixed Mob. case.

We see from figure 5.17c that there is a positive plasma potential with respect

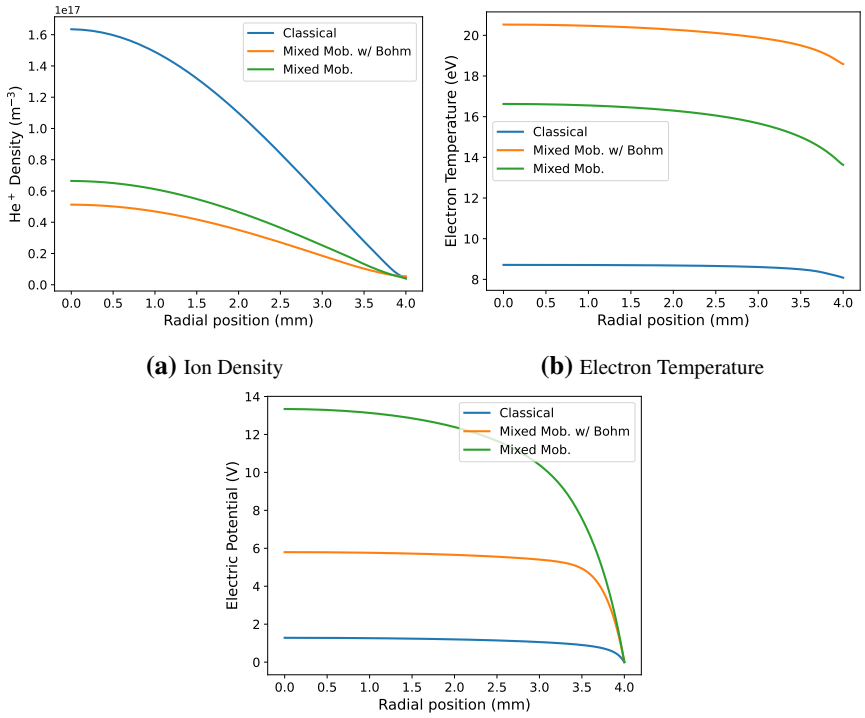

(a) Ion Density

(b) Electron Temperature

(c) Electric Potential

Figure 5.17: Average a) ion density, b) electron temperature, and c) electric potential as a function of radius for various cross field transport coefficients in the high pressure low magnetic field condition.

to the anode wall. This is because the magnetic field is weak enough and the radius of the discharge small enough that the electrons can still escape to the anode walls a bit faster than the ions. We see though that the electron temperature is not completely correlated with the magnitude of the electric potential within the plasma, since when the ions undergo Bohm diffusion, which is proportional to the electron temperature, the ions escape faster resulting in a reduced electric potential within the plasma compared to when the ions undergo classical diffusion. This also helps retard the ion flux to the anode wall at steady-state conditions which would otherwise decrease the total current on the anode wall (which is constrained to a set value).

Figure 5.18 shows the same axially averaged plots of the radial distribution of

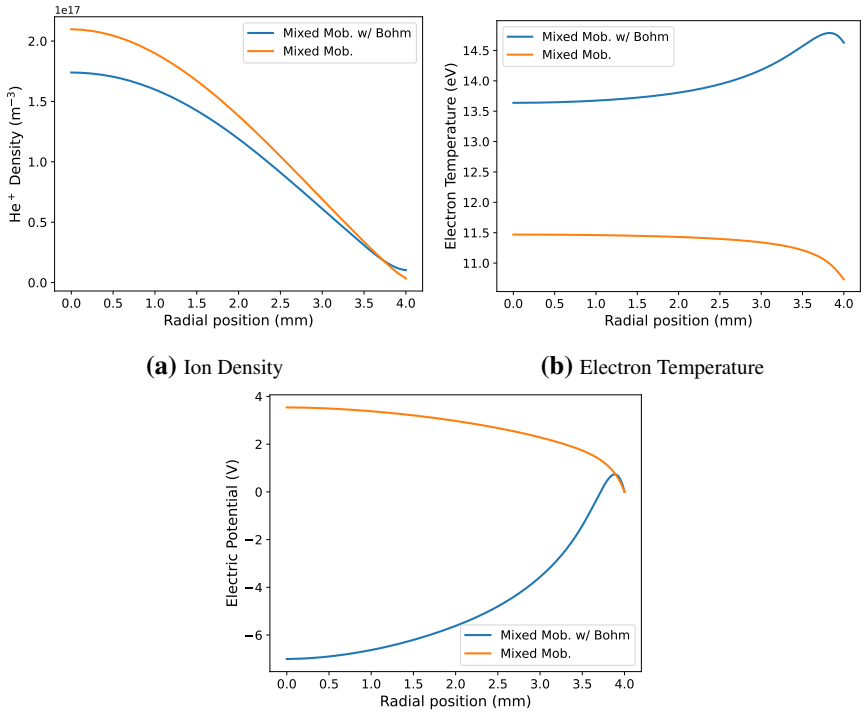

(a) Ion Density

(b) Electron Temperature

(c) Electric Potential

Figure 5.18: Average a) ion density, b) electron temperature, and c) electric potential as a function of radius for various cross field transport coefficients in the low pressure high magnetic field condition.

each plasma parameter, except for the low pressure high magnetic field case of 1.45 kV, 0.4 T, and 4 sccm. We see the comparisons of the different cases of mixed mobility electrons with either classical or Bohm diffusing ions are the same as in the high pressure case. However, one interesting note is that a negative potential(figure 5.18c), often seen in these type of discharges, is generated when Bohm diffusion for the ions is used. This negative dip is to generate the electric field that pushes out the electrons towards the anode, in order to compensate for the increased diffusion of the ions. It implies that in such a discharge, the ions also follow any E×B drift instabilities across the magnetic field, as also determined by Chen [61]. Unfortunately, there is currently no way of measuring the plasma potential within the Penning ion source, though it would be an interesting comparative diagnostic

to implement in the future. It's also shown in figure 5.18b that the negative voltage results in an energy gain of electrons in this radial electric field when moving towards the anode wall, resulting in a rise in electron temperature rather than a fall. However the wall conditions at the anode (which assumes the electron flux is from their thermal velocity) still create a small positive potential sheath at the anode edge.

5.4.2 Applied 2-D Model

Now we use the 2-D model to solve for the same input parameter variations done within the 1-D model from the OES experiments. The averaged ion densities, electron temperature, and voltage in the volume 5 mm from the center (representing the slit height) is shown as a function of parameter changes in figure 5.19. As done with the 1-D model, the variations are done for different mobility and diffusion combinations for the charged particles. The label for each combination is the same as for previous plots.

We see from figure 5.19 that the trends from the 2-D model for electron density as a function of the operational parameters is generally the same as in the 1-D model. However, figure 5.19a shows the electron density starts to decrease slightly as a function of gas flow after peaking lower than 35 sccm. This is because the peak electron density is no longer in the center of the discharge due to increased gas pressure actually increasing the radial to $\hat{z}$ electron mobility ratio. This means that electrons are less mobile along the discharge length with increased gas pressure, and thus deposit most energy in ionization before reaching the center. As mentioned before, this is likely because the electrons at the sheath edge are slower than would be expected from the energy gain in the sheath, which is why the 1-D model which improves on the charge particle speed does not have this issue. When comparing the peak or average electron density along the entire discharge, the electron density doesn't decrease with gas pressure at any point. The electron density still increases regularly with all other input parameter variations, which happens for the same reasons as explained in the 1-D model section.

Electron temperature also has the same trends as in the 1-D model except for arc voltage, which shows a similarly flat temperature with increasing arc voltage,

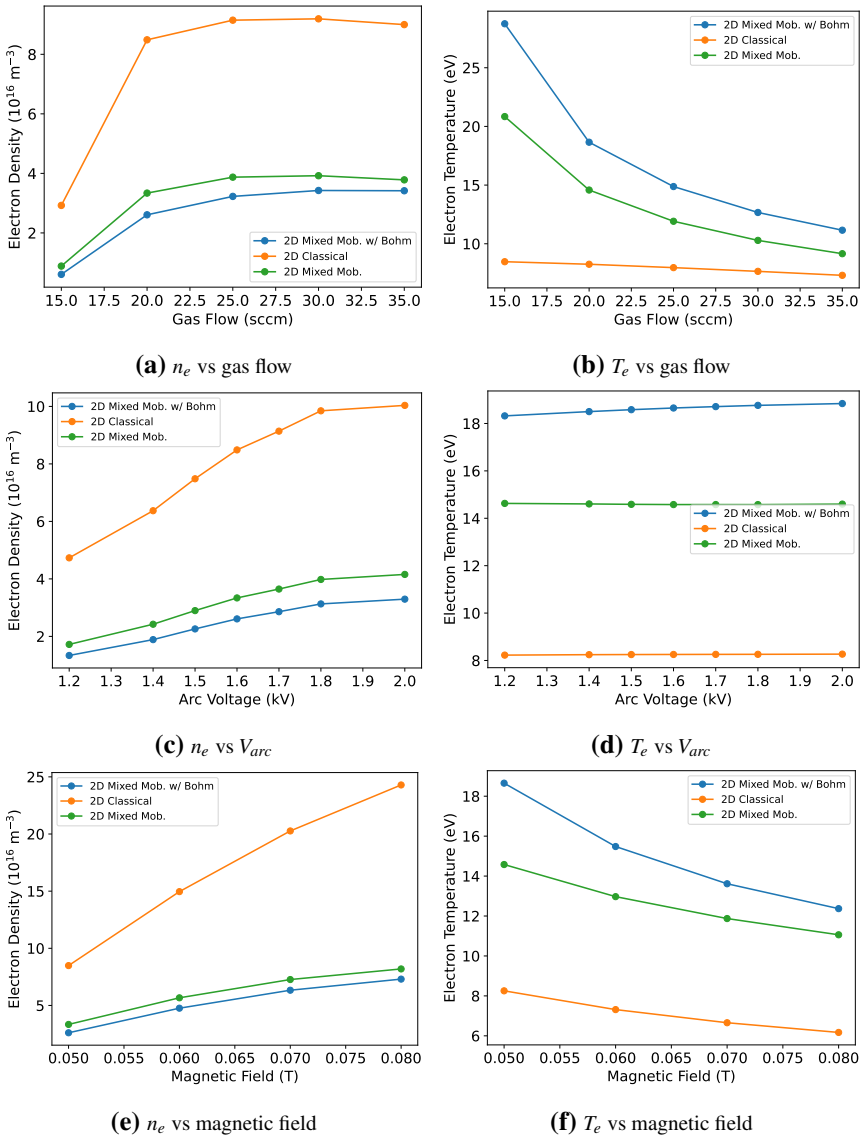

(a) n_e vs gas flow

(b) T_e vs gas flow

(c) n_e vs V_{arc}

(d) T_e vs V_{arc}

(e) n_e vs magnetic field

(f) T_e vs magnetic field

Figure 5.19: n_e and T_e as a function of (a,b) gas flow, (c,d) V_{arc}, and (e,f) magnet field strength in the high pressure low magnetic field regime using the 2-D model. Plasma parameters taken as average within 5 mm from the center. Solved for various sets of mobility and diffusion coefficients for electrons and ions.

though in this case the temperature does slightly increase. The trend though is still insignificant. Thus the 2-D model also doesn't explain the decreases in temperature we see from the OES measurements.

Figure 5.20 shows the same plots for the case of the low pressure high magnetic field regime. The trends are exactly the same, even though using Bohm diffusion for the ions creates a generally negative electric potential well within the discharge with respect to the anode wall. Once again, the classical fluid description of the charged particles cannot be solved for these cases. An interesting note is that the case for the magnetic field of 0.1 T (at 1.5 kV and 4 sccm), is not shown due to lack of convergence, which happens because the electron temperature goes too high due to lack of confinement. Thus at very low magnetic fields, the magnetic confinement using anomalous mobility for the electrons actually too weak to reach the arc current constraint. This further implies (in addition to the changing trends in figure 4.28c) that there is a variation in the charged particle transport coefficients perpendicular to the magnetic field as the magnetic field strength changes.

It is clear that as done by Chen, Bohm diffusion has to be applied to the ions in order to get the expected negative potential well typically seen in the low pressure high magnetic field regime. Regardless of the coefficients chosen or which plasma model (1-D or 2-D) is used, the simulations show clear trends of the plasma parameters as a function of gas flow and magnetic field which match the OES measurements. Unfortunately, the arc voltage variations for electron temperature are not consistent with those seen from the OES diagnostic. In addition, it seems likely that the particle transport coefficients across the magnetic field are still overly simplified, as it does not explain the change of plasma parameter trends at 0.3 T in the low pressure high magnetic field mode. It is clear that further studies on the Penning ion source need to be performed using PIC-MCC methods which use fundamental physics rather than empirical coefficients used in the drift-diffusion model to simulate the complex plasma dynamics. This is also further shown from the CPT simulations, which also show that fast electrons tend to be scattered in parallel with the magnetic field, causing a highly anisotropic electron energy distribution not taken into account in the COMSOL™ models. Overall, the 1-D model is better than the 2-D model because it shows the experimental trend of electron density increasing with gas flow at the discharge center seen from the OES mea-

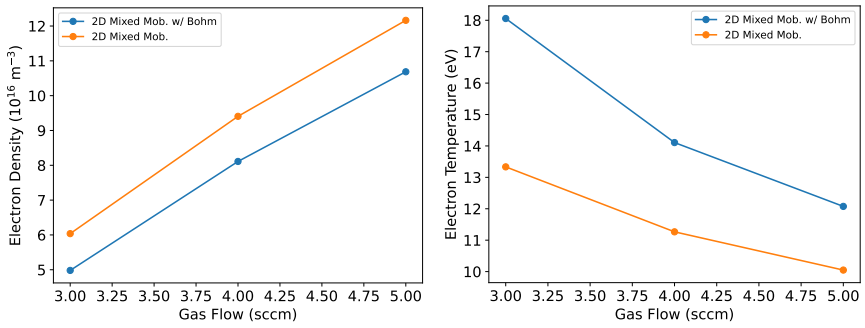

(a) n_e vs gas flow

(b) T_e vs gas flow

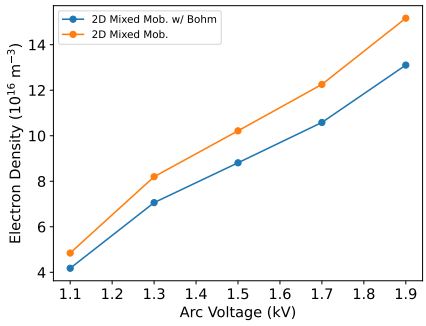

(c) n_e vs V_{arc}

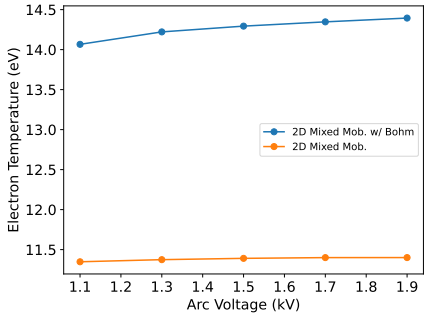

(d) T_e vs V_{arc}

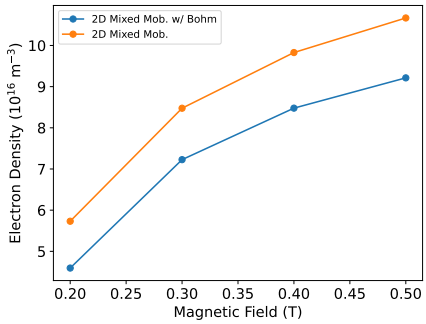

(e) n_e vs magnetic field

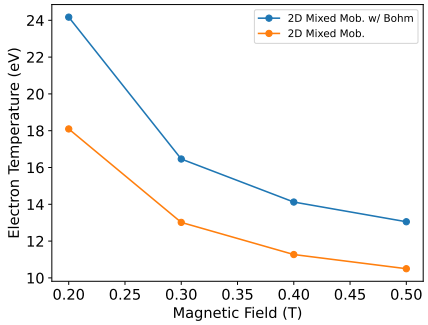

(f) T_e vs magnetic field

Figure 5.20: n_e and T_e as a function of (a,b) gas flow, (c,d) V_{arc}, and (e,f) magnet field strength in the low pressure high magnetic field regime using the 2-D model. Plasma parameters taken as average within 5 mm from the center. Solved for various sets of mobility and diffusion coefficients for electrons and ions.

surements. This is because the 1-D model actually fixes the issues with charged particle speeds calculated from the drift-diffusion model, unlike in the 2-D model. It would be worth spending greater time in the future to have the 2-D model include the cathode boundary, along with fixes to the charge particles speeds along the magnetic field. However, both models can accurately describe the trends in electron density within the discharge when varying input parameters.

Though it is not expected to produce the 100s of μA of α particles typically seen in hot cathode ion sources, the cold cathode mode's high arc voltage might allow for a high ionization rate of He^+ to α due to higher energy electrons. The density of α particles averaged within the center 5 mm of the ion source within the 1-D and 2-D simulations are shown in figure 5.21 as a function of input parameter variations. This is shown for the low pressure and high magnetic field case, as this is the case where we expect higher α production.

We see from figure 5.21a that the density is expected to decrease with gas flow due to the large decrease in electron temperature and greater probability of an electron ionizing background neutrals rather than He^+ ions. However, figure 5.21b shows an increase of α density with V_{arc} despite the flat temperature profile within the simulations. This means the increased electron density is enough to increase the He^+ ionization rate due to a lower amount of neutral gas particles. With the OES measurements however, a drop in electron temperature was observed with increasing V_{arc} so it is uncertain whether the α density will actually increase. Lastly, the magnetic field variations show a drop in α density (figure 5.21c) for the 2-D models, but the 1-D models show a fairly flat change. This is because the 1-D models show a plateau of electron temperature with magnetic field, whereas the 2-D model shows a much more drastic drop of temperature with magnetic field strength, allowing for a lower ionization rate of the He^+ ions. The α density is clearly not just correlated with electron density since the population is much lower than that of the He^+ ions, which follow electron density due to quasi-neutrality requirements of the plasma. Thus the only way to actually get an idea of whether more α particles are produced is to attempt to extract them from the plasma.

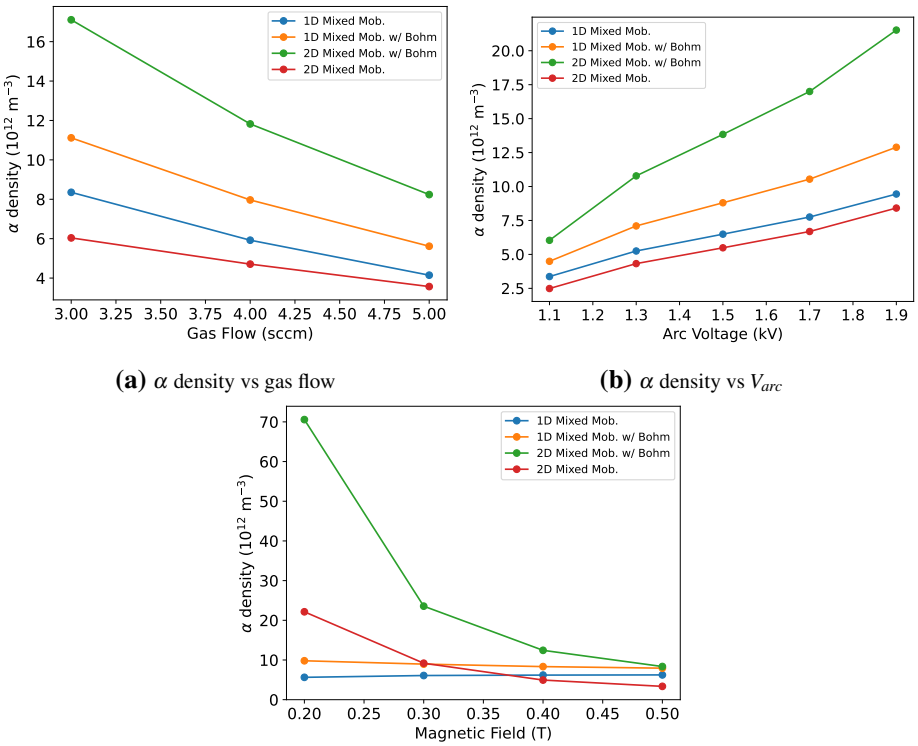

(a) α density vs gas flow

(b) α density vs V_{arc}

(c) α density vs magnetic field

Figure 5.21: α density as a function of (a) gas flow, (b) V_{arc}, and (c) magnet field strength in the low pressure high magnetic field regime using the 2-D and 1-D model. Plasma parameters taken as average within 5 mm from the center. Solved for various sets of mobility and diffusion coefficients for electrons and ions.

Chapter 6

Beam Extraction and Conclusion

Due to the last minute failure of the primary power supply used for the hot cathode mode, extraction studies are done in cold cathode operation to see how output beam current correlates with the plasma parameters measured by the OES and estimated by the COMSOL™ models.

6.1 Beam Extraction

The setup of the Faraday Cup (F-Cup) is shown in figure 6.1. The F-Cup is simply a copper block with a grounded shield in front. A 2 mm wide and 62 mm high slit on this grounded shield allows ions to pass through to the copper piece which then gets passed through a passive low pass filter (R = 10 kΩ and C = 3.2 nF) and finally read by a DAQ device (TI USB-6001). The DAQ device has an input voltage reading of 0 to 10 V. Other ions will either land on the beam dump, on the puller, or get lost due to divergence above/below the beam dump onto the magnet poles. As discussed in section 3.5.3, these ions might cause secondary emission and create electrons which contribute to sparking at the back insulator. Thus the electron trap electrodes are used to prevent this happening, allowing for stable operation.

The current on the F-Cup is read out by measuring the voltage across a load resistor (which connects to ground potential) on the DAQ device. Due to the much smaller current of the α beam when compared to the He^+ beam, experiments have to be run with different load resistors to resolve the two particle currents. For

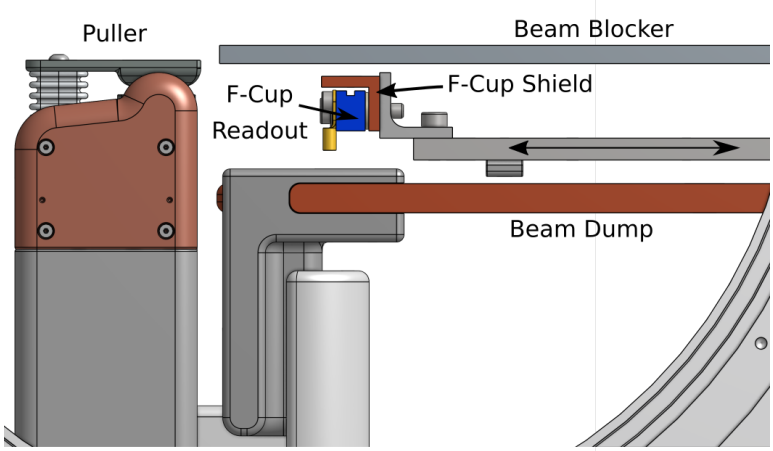

Figure 6.1: Schematic of the Ion Source and the F-Cup setup. The beam comes out from the puller and rotates. This beam can be measured by the movable faraday cup which scans back and forth. The F-Cup is simply a copper block with a grounded shield with a 2×62 mm wide slit that lets through the ions. The rest of the ions are dumped on the beam dump.

resolving He^+ currents, a load resistor of 15 kΩ is used whereas a 1 MΩ load resistor is used for resolving α currents. In order to prevent overloading the DAQ device when measuring He^+ currents on the 1 MΩ resistor, a 10 V metal oxide varistor (MOV) is placed in parallel to cut out these higher voltages. A 3.2 kΩ resistor is placed between the beam dump and ground as a load resistor in order to measure the current on the beam dump, with the voltage being read out on the PLC control system at the ISTF. A similar technique is used to read out the beam current on the puller, which uses a 10 kΩ load resistor.

The F-Cup is moved via a vacuum compatible linear stage (Zaber LSM200A-V2T4, X-MCB1 controller), and scans are done by a LabVIEW™ program which moves the F-Cup back and forth whilst reading the currents as a function of its distance. An example scan is shown in figure 6.2a, with the measured current as a function of the mass to charge ratio. Due to the large number of points and relatively small error, the error for each measurement is not shown, but the error

is estimated to be 10 μA for each point. The independent variable is actually the distance traveled from the ion source center, but is estimated as the mass to charge ratio by assuming the distance traveled is the diameter (so 2$\times$ the gyroradius):

$$d_\omega = 2\frac{m}{|q|}\frac{v_\perp}{B} \tag{6.1}$$

where $\frac{m}{|q|}$ is the particle mass to charge ratio, and $v_\perp$ the ion speed perpendicular to the magnetic field B. $v_\perp$ is calculated assuming the ion has gain the full energy from the extraction voltage and is coming out perpendicular to the puller slit. There are a few reasons why each particle shows a smaller mass to charge ratio than expected from equation 6.1. The ions will have velocity along the magnetic field, which will reduce $v_\perp$ and therefore d_ω. The ions may not reach the full energy from the extraction voltage because of collisions with background gas or due to space-charge effects which create a positive potential within the beam, consequentially lowering the energy of the ions and therefore $v_\perp$. In addition the effects of the plasma on extraction can create a plasma meniscus, which can create a curve in the electric potential near extraction causing the ions to follow a diverging or converging electric field. This can change the initial angle that the particles are extracted, which would make the ion trajectory intersect with the F-Cup's path closer to the ion source. It should be mentioned that the distance from the ion source (d_ω) is based on CAD models, and stack up tolerances along with minor changes will introduce an unknown systematic error that is estimated to be up to 5 mm. However, this does not explain why the broadening exists.

To show that a broadened peak below an estimated mass to charge ratio isn't unusual, a Charged Particle Tracing simulation in COMSOL™ was performed using a simplified model of the puller and anode discharge. In this case, about 2 mA of He^+ current and 10 μA of α particles are input into the simulation domain uniformly onto the slit area about 0.5 mm inside the anode plate's slit. The anode is set to 2.5 kV with the puller and surrounding walls at ground. The magnetic field is based on a measured magnetic field mapping of the C-magnet along the pole gap's center with peak field of about 0.4 T. These parameters are chosen to closely match the experimental conditions of the example scan. A surface which represents the approximate total surface area swept by the F-Cup is used as a particle accumula-

tor, which is a node that allows for the calculation of the particle current passing through this surface mesh. The resultant expected current measured by the F-Cup as a function of mass to charge ratio, with this calculated in the same way as in equation 6.1, is shown in figure 6.2b. We see that like in figure 6.2b, the mass to charge ratio is very broad and less than the expected 4 for He^+ and 2 for α. Thus even without considering the effects of a plasma meniscus or collisions with background gas, a significant broadening is seen due to some portion of velocity going along the magnetic field, the different directions of the particles when coming out the puller resulting in different intersections with the F-Cup path, and some ions not gaining all the possible energy due to the space charge of the beam creating a positive potential along the beam path. It should be mentioned that the results are similar even when assuming a constant 0.4 T field, thus this is not due to a changing magnetic field along the ion trajectory.

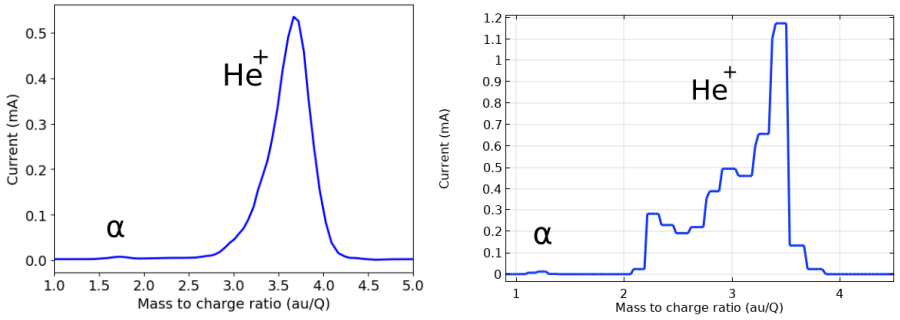

(a) Experimental scan

(b) Simulated scan

Figure 6.2: (a) F-Cup measurement using 15 kΩ load resistor at V_{ext} = 2.5 kV, V_{arc} = 1.7 kV, Q = 4 sccm, and magnetic field strength of 0.4 T. (b) Simulated F-Cup measurement at 0.4 T, V_{ext} = 2.5 kV, for input currents of 2 mA of He^+ and 10 μA of α particles

One should note that when measuring with larger load resistors for α resolution, we find current bumps at charge to mass ratios lower than 1 which must be H^+ ions. Thus one might expect H_2^+ molecular ions to be formed within the plasma as well if this comes from residual H_2 molecules, which unfortunately has the same mass to charge ratio as α particles. However, similar sources running hydrogen gas have much lower currents of H_2^+ than H^+ [13]. In addition, the likely source

of these ions is water left within the V-Box, which typically dissociates into OH^- and H^+. Thus it is assumed that the currents read out on the current bump below the primary He^+ beam is mostly composed of α particles.

An interesting initial observation when extracting beam from the ion source in cold cathode mode, where the the arc current without extraction is on the order of 10s of mA, is that the extracted beam takes out so many charged particles that the arc current of the plasma discharge is reduced. This is shown in figure 6.3, where the bias current (red) and arc current (blue) are plotted as a function of extraction voltage (V_{ext}) between the puller and anode. This data is taken at 4 sccm gas flow, 1.5 kV arc voltage, and 0.2 T magnetic field strength. The bias current is the total current read on the bias power supply, which supplies the extraction voltage. Thus it is essentially the total ion current hitting grounded portions within the vacuum box, in addition to any secondary electrons which may be produced. We see that the arc current decreases with increasing bias current, and what is not shown is that past about 3 kV (depending on discharge conditions), the discharge is dissipated (arc current drops to 0 mA). This is likely because enough ions are pulled out that the discharge can no longer sustain itself through ion bombardment of the cathode, and therefore the discharge dissipates. It should be noted that from preliminary data with the hot cathode discharge, where arc currents reach up to 3 A, bias currents could go above 35 mA at 15 kV with negligible change to the arc power. The reason the extracted beam current to arc discharge current ratio is smaller within the hot cathode mode is because the electric field cannot penetrate as deeply within the discharge. This is because the higher electron density produces a smaller debye length, meaning electrostatic fields cannot penetrate as deeply into the plasma.

In order to estimate the total current for a particle in a single Faraday cup scan, a peak finding algorithm from the signals module (which is within the SciPy package) in Python is used to find the bases of the peaks. The peak is then integrated between the two baselines and then divided by the 2 mm slit width of the F-Cup grounded shield. Up to 10 Faraday cup scans are performed, with a peak finding and integration procedure performed for each scan. The measured current is then the mean and standard deviation of these current measurements. The measured He^+ currents are read out as a function of the primary input parameter variations, which are shown in figure 6.4. The extraction voltage is held constant at 2.5 kV.

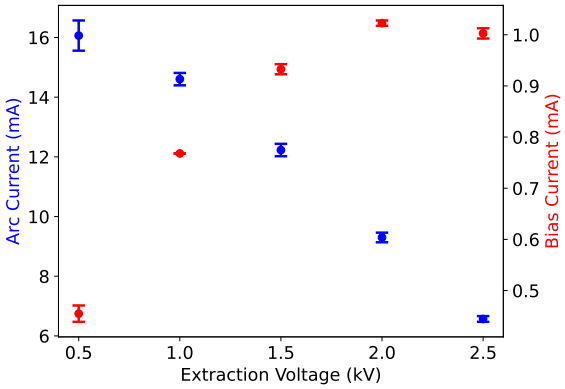

Figure 6.3: Total current from bias power supply (red) and discharge arc current (blue) as a function of extraction voltage between puller electrode and anode.

The total current read out on the beam dump and the total bias current is also shown for each case. The ion beams in the high pressure low magnetic field regime cannot be measured since the low magnetic field does not curve the ion trajectory enough to be measured by the Faraday Cup.

The He^+ current is less than the total bias current for each parameter variation. Since the beam is almost entirely composed of He^+ particles (which we see since the He^+ current is slightly below the beam dump current), this suggests that the beam is diverging enough along the magnetic field to hit the poles of the electromagnetic within the vacuum box. This is seen in the COMSOL™ simulations and observed as scorch marks on the magnet pole. Thus we cannot actually measure the entire beam in this current configuration. The puller current is not shown since the current is much lower than the measured He^+ current, thus it is insignificant. It is clear though that an increase in each input parameter results in an increase of He^+ current extracted. This corresponds exactly to the increase in electron/ion density observed through the OES measurements (section 4.6.1) and within the COMSOL™ simulations (section 5.3.2 and 5.4). Thus it is confirmed by three separate methods that the ion, and thus electron density, increases with gas flow, arc voltage, and magnetic field strength.

Unfortunately, there is no way of directly measuring the α density within the

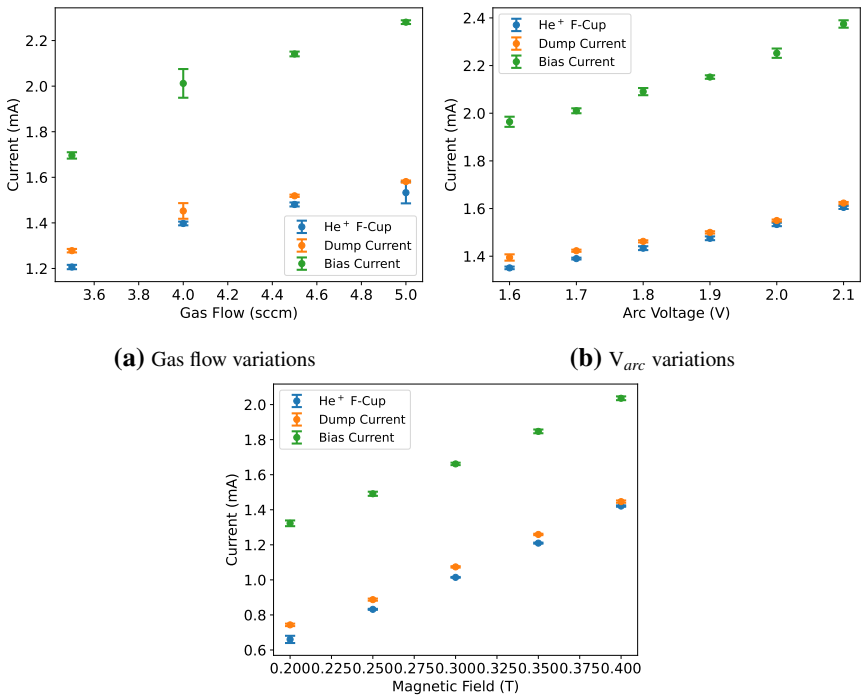

(a) Gas flow variations

(b) V_{arc} variations

(c) Magnetic field variations

Figure 6.4: Variations of He^+, beam dump, and bias current are shown as a function of variations in (a) gas flow, (b) arc voltage and (c) magnetic field at V_{ext} = 2.5 kV. The values of other constant parameters for each case are: (a) V_{arc} = 1.5 kV and B-Field = 0.41 T, (b) Q = 4 sccm and B-Field = 0.4 T, and (c) Q = 4 sccm and V_{arc} = 1.75 kV.

plasma using the current experimental setup. Therefore the only way to get information is by direct extraction. However, a problem is quickly seen when measuring the α current from the F-Cup, as shown in figure 6.5. This shows the integrated α current from the F-Cup in red and the measured puller current in blue. One may be tempted to make judgements from such plots, for example in figure 6.5c where it seems the α current increases with magnetic field whilst the puller current decreases. However, as the puller current is several times higher than the α current, it is possible that most of the reduction on the puller is from more He^+ ions making through, whereas the opposite happens to the α particles due to the differences in curvature in the magnetic field. The same can be said for the other plots.

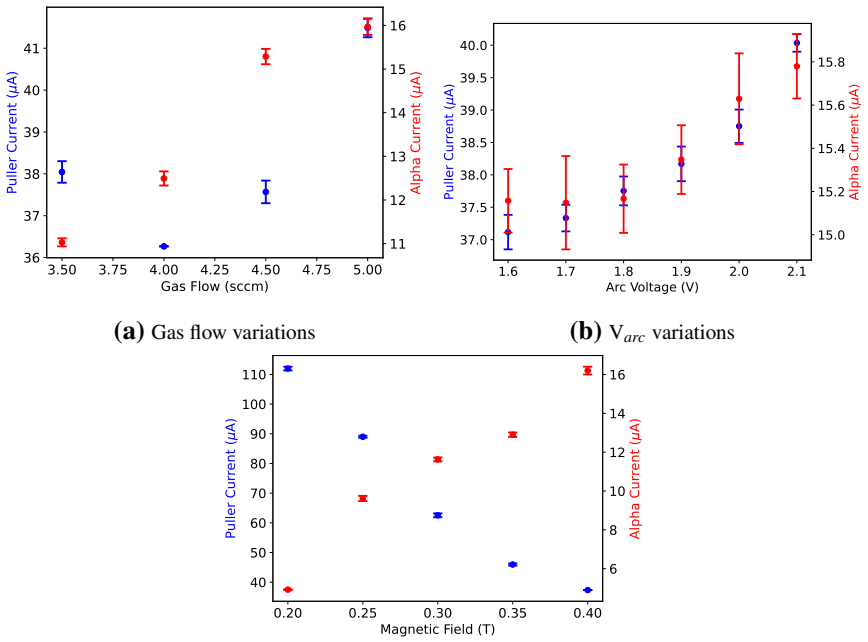

(a) Gas flow variations

(b) V_{arc} variations

(c) Magnetic field variations

Figure 6.5: Variations of α (red) and puller current (blue) are shown as a function of variations in (a) gas flow, (b) arc voltage and (c) magnetic field at V_{ext} = 2.5 kV. The values of other constant parameters for each case are: (a) V_{arc} = 1.5 kV and B-Field = 0.41 T, (b) Q = 4 sccm and B-Field = 0.4 T, and (c) Q = 4 sccm and V_{arc} = 1.75 kV.

The primary issue of course is that the extraction voltage is 6× lower than the 15 kV it is designed for. Thus the extracted ions do not accelerate as quickly and can therefore more easily hit the puller. In the future, these experiments will be performed for the hot cathode mode as intended at 15 kV extraction. Therefore, extraction studies with the cold cathode source using the current system can only confirm the increase of He^+ currents with all varied input parameters, with an open question as to how much α particles are produced as a function of the input parameters.

6.2 Conclusion

An experimental setup for studying a Penning ion source discharge using helium gas was designed and manufactured. The purpose of this test stand is to characterize the Penning discharge as a function of operational parameters such as the input gas flow, arc power, and magnetic field strength using helium gas. This is done to better understand the underlying plasma physics within the ion source and how they change as the input parameters are varied. A better understanding of the plasma physics could lead to future developments of this source that can optimize ion beam output. It is specifically of interest to develop a source that can maximize α particle output, which would then be a commercially viable alternative to ECR sources that are currently used to produce these particles in medical accelerators.

Chapter 3 of this thesis reviewed the engineering and physics involved to create this test stand. The test stand is composed of a large C-magnet that generates a magnetic field used to confine the plasma and to curve the trajectory of the extracted ion beam for current measurements with a Faraday cup. The original test stand was setup within a couple of years, but experiments ultimately showed that the ion source could not be operated under high voltage due to potential triple points and secondary electrons generating sparks near exposed insulators. A new ion source was designed to fix these issues, with heavy reliance on COMSOL™ Multiphysics to simulate various portions of the source. This included simulating electrostatics to make sure the electric fields are low enough to not generate sparks, heat transfer to make sure components stay at appropriate temperatures to avoid additional electron emission, and charged-particle tracing to design the extraction system. The new ion source was able to sustain up to 15 kV at gas flows up to 40 sccm without issue, but adding the plasma discharge showed that secondary electrons were still an issue due to E$\times$B drifts directing them towards the high voltage insulators. An electron trap was designed to trap these electrons, and along with improvements to avoid cathode sputtering affecting the plasma discharge, the ion source was made operational. The final ion source can now be operated up to 15 kV extraction voltage, 0.94 T, and to 40 sccm.

In order to see how internal plasma properties are affected by input parameter variations of the PIG source, we need a way of measuring the plasma prop-

erties. One way of diagnosing the plasma is using optical emission spectroscopy (OES), which is a method of evaluating the plasma properties such as electron density and temperature using the emitted light from the helium excited states within the plasma. A collisional-radiative model for helium plasmas was created in order to do this, as shown in chapter 4. This collisional-radiative model compares well with another collisional-radiative model developed at IPP Garching called Yacora on the Web, and actually improves upon it using approximations for radiation trapping. This is shown by comparing this diagnostic to another diagnostic made for this thesis called the Langmuir probe. This comparison was done on an ion source that is fairly robust and can be diagnosed using both methods. It was found that trends in electron density match well between the two diagnostics, but electron temperature does not always match due to the possible existence of non-Maxwellian electrons from the electron beam produced at the cathode sheath. This means that the portion of high-energy electrons increases when approaching the cathode sheath, which was shown using measured spatial variations of the β parameter within the TRIUMF-licensed filament ion source using the Langmuir probe. The non-Maxwellian portion of electrons was shown to be up to 4% of the total electron population, with the electron temperature between 3 - 4.5 eV for operations of 1 - 5 A arc current, 100 - 200 V arc voltage, and 7 - 35 sccm gas flows. This non-Maxwellian component led to electron temperatures measured by the OES to be up to 6 eV. The OES diagnostic, applied to the Penning discharge in the cold cathode mode, shows that electron density increases with all three input parameters (gas flow, arc voltage, and magnetic field strength), thus increases of each is expected to increase ion current. It was shown that electron temperatures for cold cathode Penning discharges under low pressure (2-6 sccm), high magnetic field ($\geq$ 0.2 T) operation can be between 16 - 35 eV with electron densities of 0.5×10^{17} - 4.5×10^{17} m^{-3}. When operating under high pressures ($\geq$ 15 sccm) and low magnetic field ($\leq$ 0.08 T), the electron temperatures are decreased to 14 - 23 eV whilst electron density is increased to 1×10^{17} - 5.7×10^{17} m^{-3}. Using these OES measurements, the properties of the Penning ion source plasma can now be compared to expected values from simulated models, and correlated with ion beam output for varied operational parameters.

Chapter 5 describes the simulations of the Penning ion source using COM-

SOL™ to better understand and explain the plasma properties as a function of the input parameters. COMSOL™ was chosen due to availability and to see whether a relatively simple model (based on the drift-diffusion model) can explain the plasma properties observed. Simulations were done in 1-D and 2-D. The 1-D model was significantly improved by modifying the COMSOL™ model to more accurately simulate the charge particle's speed in high electric fields within the cathode sheath. Though this model could predict most of the trends measured using the OES diagnostic, it was shown using the charged-particle tracing module that likely fast non-Maxwellian electrons exist which are anisotropic with respect to the magnetic field. Therefore, the model still neglects what may be an important plasma property when studying the effects of input parameter variations on plasma dynamics. The 2-D model, while also able to predict the same trends in electron density and electron temperature as in the 1-D model, still has these flaws. In general, the electron temperatures and densities are lower than measured using the OES diagnostic. For example, the 1-D model high pressure and low magnetic field simulations predict electron temperatures of 6 - 13 eV, whereas the OES measured electron temperatures of 14 - 23 eV. The electron density measured by the OES was 1×10^{17} - 5.7×10^{17} m^{-3}, with the simulated densities lowered to 0.1×10^{17} - 1.8×10^{17} m^{-3}. Despite their limitations, both models are consistent with the OES measured trends except: when comparing electron temperature as a function of arc voltage, and when observing the changing trends in the plasma parameters at high magnetic fields under low pressure operation. Thus such models can be used for qualitative modeling of ion sources under various operational states, but more studies should be performed to improve the modeling of high energy electrons from the cathode sheath, and particle transport perpendicular to the magnetic field. These models also included the formation of α particles, which showed that the α particle density within the ion source is expected to decrease with increasing gas flow, increase with increasing arc voltage, and decrease with increasing magnetic field strength.

Lastly, extraction of the ions from the source showed that for the cold cathode mode operation, only lower voltages up to 3 kV can be applied, otherwise the reduction of plasma ions will dissipate the discharge. The increase of electron density shown in both OES measurements and plasma simulations clearly corresponds to an increase in ion extraction as expected. However, a higher puller current com-

pared to the extracted α current makes comparisons of α current vs input parameter variation impossible at the moment. Only up to 16 μA of α particle current could be extracted in the cold cathode mode. However, in the hot cathode mode where the arc current is increased by a factor greater than $\times 100$, it is expected the currents will be at least on the order of 100s μA.

6.2.1 Future studies

Something that is both fortunate and unfortunate about research and design done in a set amount of time is that all the questions you get to answer will only lead to more questions you want to answer. Though this thesis has led to many insights, many open questions still exist that we hope to answer in the future.

It's clear from this thesis that the assumption of Maxwellian electrons used within most plasmas is likely not applicable to low pressure ion sources. Thus we need a better way to model these ion sources to understand what is going on within the plasma as we change its operational state. As discussed beforehand, the best way to simulate the plasma which gives this sort of information are particle-in-cell codes, and D-Pace is currently looking into creating such a code within the next few years with the help of Dr. Gwenael Fubiani. Though the simplified model within COMSOL™ has worked well for replicating the trends we see for primary ion production (He^+ in this case), it is clear that more details on electron kinetics are needed to properly describe the plasma dynamics. Most importantly, this would lead to a better model of α production, which likely relies heavily on high-energy electrons due to the high ionization energy of He^+. This would allow us to better model how these parameter variations change α production rather than simply the electron density.

There are also further experiments that will need to be done to study how α particle production depends on the operational parameters in the hot cathode mode. For this, we will need to operate the ion source while varying the operational parameters of gas flow, magnetic field strength, and arc current at maximum extraction voltage (15 kV). This will be used to determine what values of each parameter are needed to maximize α particle extraction. It is possible that some combination of optimal extraction cannot be reached given the current Penning ion source

design. In which case, re-designs will have to be done using modern engineering solutions in order to reach this optimized operational mode. In addition, we will measure the plasma properties using the OES diagnostic to provide clues as to why these operational parameters optimize α particle production. Using this information, it might be possible to implement unique engineering solutions when designing an ion source which allow us to optimize α extraction without simply pushing the limits of an operational parameter, which may be difficult or costly to do.

In addition, improvements to extraction experiments will likely need to be done to better resolve the α particle currents. One way to do this is by using a movable puller, which can be positioned until a maximum α current is readout on the F-Cup. This would allow us to readout α currents while minimizing bombardment of these particles on the puller. A movable puller has already been designed and manufactured which can be placed on the flange opposite the one used for the ion source, and we hope to start experiments with this puller within the next year.

Bibliography

[1] Nicolas Savard, Dave Potkins, Philip Jackle, J. Theroux, Stephane Melanson, Giulia Marcoux, and Morgan Dehnel. Development of a penning ion source test stand for production of alpha particles. *Proceedings for the 9th International Particle Accelerator Conference (IPAC 2018)*, 05 2019. → page vi

[2] Nicolas Savard, Alexey Groutso, Stephane Melanson, Dave Potkins, and Morgan Dehnel. Trapping secondary electrons in exb drift for an alpha generating penning ion source. *Proceedings for 19th International Conference on Ion Sources (ICIS 2021)*. → page vi

[3] Ben Dotson. How particle accelerators work. https://www.energy.gov/articles/how-particle-accelerators-work. → page 1

[4] Radioisotopes in medicine. https://world-nuclear.org/information-library/non-power-nuclear-applications/radioisotopes-research/radioisotopes-in-medicine.aspx. → page 1

[5] Michael R. Zalutsky and Marek Pruszynski. Astatine-211: Production and availability. *Current Radiopharmaceuticalse*, 4(3):177–185, 2011. → page 1

[6] Richard Pardo. Review of high intensity ion source development and operation. *Review of Scientific Instruments*, 90(12):123312, 2019. → page 2

[7] W. Kleeven, M. Abs, J.L. Delvaux, E. Forton, Y. Jongen, L. Medeiros Romao, B. Nactergal, V. Nuttens, T. Servais, T. Vanderlinden, and S. Zaremba. Recent development and progress of iba cyclotrons. *Nuclear Instruments and Methods in Physics Research Section B: Beam Interactions with Materials and Atoms*, 269(24):2857–2862, 2011. Proceedings of the 10th European Conference on Accelerators in Applied Research and Technology (ECAART10). → page 2

[8] Bernhard Wolf. *Handbook of Ion Sources*. CRC Press, 2020. → pages 2, 3, 33

[9] R. L. Darling and R. H. Davis. Analysis of high-charge state output from a penning ion source. *Review of Scientific Instruments*, 44(4):375–378, 1973. → page 3

[10] J. R. J. Bennett. A review of pig sources for multiply charged heavy ions. *IEEE Transactions on Nuclear Science*, 19(2):48–68, 1972. → pages 3, 33, 51, 62

[11] M. L. Mallory and D. H. Crandall. A penning multiply charged heavy ion source test facility. *IEEE Transactions on Nuclear Science*, 23(2):1069–1072, 1976.

[12] J. R. Bennett and Basil Gavin. A high power penning source for multiply charged heavy ions. *Particle Accelerators*, 3:85–90, 1972. → page 5

[13] Carl E. Anderson and Kenneth W. Ehlers. Ion source for the production of multiply charged heavy ions. *Review of Scientific Instruments*, 27(10):809–817, 1956. → page 155

[14] Royce J. Jones and Alexander Zucker. Two ion sources for the production of multiply charged nitrogen ions. *Review of Scientific Instruments*, 25(6):562–566, 1954. → page 3

[15] Lin-xing Chen and Nao-bei Chen. An intense alpha ion sources for inrs cyclotron. *IEEE Transactions on Nuclear Science*, 32(5):1773–1775, 1985. → pages 3, 4, 53

[16] T. Y. T. Kuo and J. S. Laughlin. *Initial Experience in Ion Production Using an Ultra-high Power Density Method*, pages 381–385. Birkhuser Basel, Basel, 1975. → pages 3, 4, 33, 53

[17] John Backus. Studies of cold cathode discharges in magnetic fields. *Journal of Applied Physics*, 30(12):1866–1869, 1959. → page 4

[18] Rafal Walczak, Seweryn Krajewski, Katarzyna Szkliniarz, Mateusz Sitarz, Kamel Abbas, Jaroslaw Choinski, Andrzej Jakubowski, Jerzy Jastrzebski, Agnieszka Majkowska, Federica Simonelli, and et al. Cyclotron production of 43sc for pet imaging. *EJNMMI Physics*, 2(1), Dec 2015. → page 5

[19] D-pace inc. https://www.d-pace.com/. → page 5

[20] W. C. Martin and W. L. Wiese. Atomic spectroscopy - a compendium of basic ideas, notation, data, and formulas, Nov 2019. → pages 9, 10

[21] Lawrence A. Kennedy and A. A. Fridman. *Plasma physics and engineering*. Taylor and Francis, 2004. → pages 12, 13, 18, 22

[22] Michael A. Lieberman and Allan J. Lichtenberg. *Principles of plasma discharges and materials processing*. Wiley-Interscience, 2005. → pages 12, 13, 18, 20, 21, 57, 59

[23] Francis F. Chen. *Introduction to plasma physics and controlled fusion*. Plenum Press, 2011. → pages 14, 15, 18, 47, 84, 114

[24] Boris M. Smirnov. *Theory of gas discharge plasma*. Springer International Pu, 2016. → pages 22, 69, 119, 131

[25] Comsol multiphysics™ v5.5. www.comsol.com. → pages 26, 28

[26] Jack Dutton. Survey of electron swarm data. *J. Phys. Chem. Ref. Data*, 4:577, 1975. → page 28

[27] https://www.pfeiffer-vacuum.com/en/know-how/introduction-to-vacuum-technology/fundamentals/conductance/. → page 31

[28] R. Kersevan and J.-L. Pons. Introduction to molflow+: New graphical processing unit-based monte carlo code for simulating molecular flows and for calculating angular coefficients in the compute unified device architecture environment. *Journal of Vacuum Science & Technology A*, 27(4):1017–1023, 2009. → page 31

[29] Steven Battel. High voltage engineering techniques for space applications. → page 37

[30] V.a. Godyak, V.p. Meytlis, and H.r. Strauss. Tonks-Langmuir problem for a bi-Maxwellian plasma. *IEEE Transactions on Plasma Science*, 23(4):728–734, 1995. → page 58

[31] Kil-Byoung Chai and Duck-Hee Kwon. Optical emission spectroscopy and collisional-radiative modeling for low temperature ar plasmas. *Journal of Quantitative Spectroscopy and Radiative Transfer*, 227:136–144, 2019. → pages 58, 71

[32] Damiano Pagano, Claudine Gorse, and Mario Capitelli. Modeling multicusp negative-ion sources. *IEEE Transactions on Plasma Science*, 35(5):1247–1259, 2007. → page 58

[33] J Bretagne, G Delouya, M Capitelli, C Gorse, and M Bacal. On electron energy distribution functions in low-pressure magnetic multicusp hydrogen discharges. *Journal of Physics D: Applied Physics*, 19(7):1197–1211, 1986. → page 58

[34] J Komppula and O Tarvainen. Vuv diagnostics of electron impact processes in low temperature molecular hydrogen plasma. *Plasma Sources Science and Technology*, 24(4):045008, Jul 2015. → page 59

[35] H Chung, R Lee, M Chen, and Y Ralchenko. *FLYCHK*. NIST, 2008. → page 60

[36] Sarah Luisa Siepa. *Global collisional-radiative model for optical emission spectroscopy of argon and argon-containing plasmas*. PhD thesis, 2017. → pages 61, 71

[37] U Fantz. Basics of plasma spectroscopy. *Plasma Sources Science and Technology*, 15(4), 2006. → page 61

[38] W. Moller. Plasma and surface modeling of the deposition of hydrogenated carbon films from low-pressure methane plasmas. *Applied Physics A Solids and Surfaces*, 56(6):527–546, 1993. → page 64

[39] K. L. Junck, M. L. Brake, and W. D. Getty. Optical emission spectroscopy of electron-cyclotron-resonance-heated helium mirror plasmas. *Plasma Chemistry and Plasma Processing*, 11(1):15–39, 1991. → page 65

[40] R. F. Boivin, J. L. Kline, and E. E. Scime. Electron temperature measurement by a helium line intensity ratio method in helicon plasmas. *Physics of Plasmas*, 8(12):5303–5314, 2001. → pages 65, 75

[41] R Fischer and V Dose. Electron energy distribution reconstruction in low-pressure helium plasmas from optical measurements. *Plasma Phys. Control. Fusion*, 41:1109–1123, 1999. → pages 71, 72

[42] Takashi Fujimoto. A collisional-radiative model for helium and its application to a discharge plasma. *Journal of Quantitative Spectroscopy and Radiative Transfer*, 21(5):439–455, 1979. → pages 65, 72, 79

[43] D Nishijima and E M Hollmann. Determination of the optical escape factor from the he i intensity ratio technique applied for weakly ionized plasmas. *Plasma Physics and Controlled Fusion*, 49(6):791–802, 2007. → page 75

[44] Wonwook Lee, Kyungdeuk Park, Duck-Hee Kwon, and Cha-Hwan Oh. Optical diagnostics with radiation trapping effect in low density and low temperature helium plasma. *Physics of Plasmas*, 23(6):063516, 2016. → pages 65, 71, 94

[45] Shin Kajita, Noriyasu Ohno, Shuichi Takamura, and Tomohide Nakano. Comparison of heiline intensity ratio method and electrostatic probe for electron density and temperature measurements in nagdis-ii. *Physics of Plasmas*, 13(1):013301, 2006. → pages 65, 72, 94

[46] B. Schweer, G. Mank, A. Pospieszczyk, B. Brosda, and B. Pohlmeyer. Electron temperature and electron density profiles measured with a thermal he-beam in the plasma boundary of textor. *Journal of Nuclear Materials*, 196-198:174–178, 1992.

[47] Shuiliang Ma, John Howard, Boyd D. Blackwell, and Nandika Thapar. Measurements of electron density and temperature in the h-1 heliac plasma by helium line intensity ratios. *Review of Scientific Instruments*, 83(3):033102, 2012. → page 65

[48] Shin Kajita and Noriyasu Ohno. Practical selection of emission lines of he i to determine the photon absorption rate. *Review of Scientific Instruments*, 82(2):023501, 2011. → pages 65, 71, 75

[49] D. Wunderlich, M. Giacomin, R. Ritz, and U. Fantz. Yacora on the web: Online collisional radiative models for plasmas containing h, h2 or he. *Journal of Quantitative Spectroscopy and Radiative Transfer*, 240:106695, 2020. → page 65

[50] Welcome to python. https://www.python.org/. → page 66

[51] https://numpy.org/. → page 67

[52] Yu. Ralchenko, R.K. Janev, T. Kato, D.V. Fursa, I. Bray, and F.J. de Heer. Electron-impact excitation and ionization cross sections for ground state and excited helium atoms. *Atomic Data and Nuclear Data Tables*, 94(4):603–622, 2008. → pages 70, 79, 117

[53] Xi-Ming Zhu, Yi-Kang Pu, Yusuf Celik, Sarah Siepa, Edmund Schüngel, Dirk Luggenhölscher, and Uwe Czarnetzki. Possibilities of determining non-maxwellian eedfs from the oes line-ratios in low-pressure capacitive and inductive plasmas containing argon and krypton. *Plasma Sources Science and Technology*, 21(2):024003, 2012. → page 71

[54] K Behringer and U Fantz. The influence of opacity on hydrogen excited-state population and applications to low-temperature plasmas. *New Journal of Physics*, 2:23–23, 2000. → page 71

[55] Masamoto Otsuka, Ryuiti Ikee, and Kazushige Ishii. Optical escape factors and population densities for tpd-plasma. *Journal of Quantitative Spectroscopy and Radiative Transfer*, 21(1):41–53, 1979. → pages 72, 73

[56] R. Mewe. Interpolation Formulae for the Electron Impact Excitation of Ions in the H-, He-, Li-, and Ne- Sequences. *Astronomy and Astrophysics*, 20:215, August 1972. → page 79

[57] Usb-6001 ni. https://www.ni.com/en-ca/support/model.usb-6001.html. → page 85

[58] Scipy. https://www.scipy.org/. → page 86

[59] E.B. Hooper. A review of reflex and penning discharges. volume 27 of *Advances in Electronics and Electron Physics*, pages 295–343. Academic Press, 1970. → page 107

[60] H. Schulte, B. H. Wolf, and H. Winter. Ion and electron flow in hot-cathode pig sources for multiply charged heavy ions. *IEEE Transactions on Nuclear Science*, 23(2):1053–1060, Apr 1976. → pages 108, 132

[61] Francis F. Chen. Radial electric field in a reflex discharge. *Phys. Rev. Lett.*, 8:234–237, Mar 1962. → pages 108, 113, 126, 145

[62] I M Montellano, Dirk Wunderlich, S Mochalskyy, and U Fantz. 3d-pic modelling of a low temperature plasma sheath with wall emission of negative particles and its application to nbi sources. *J. Phys. D: Appl. Phys.*, 52, Mar 2019. → page 110

[63] Johan Carlsson, Igor Kaganovich, Andrew Powis, Yevgeny Raitses, Ivan Romadanov, and Andrei Smolyakov. Particle-in-cell simulations of anomalous transport in a penning discharge. *Physics of Plasmas*, 25(6):061201, 2018. → pages 110, 113

[64] Jingfeng Zhang et al. A Particle-in-Cell/Monte-Carlo-Collision Code for the Simulation of Stepwise Ionization of Lithium in 2.45 GHz ECR Ion Source. In *23rd International Workshop on ECR Ion Sources*, page TUP26, 2019.

[65] M. Rafieian Najaf Abadi, M. Mahjour-Shafiei, and M. Yarmohammadi Satri. Simulation and optimization of a negative hydrogen penning ion source. *Physics of Plasmas*, 25(12):123501, 2018. → page 110

[66] COMSOL Multiphysics™v5.5, COMSOL AB, Stockholm, Sweden. *Plasma Module User's Guide*, 2019. → page 111

[67] M. V. Umansky, P. Popovich, T. A. Carter, B. Friedman, and W. M. Nevins. Numerical simulation and analysis of plasma turbulence the large plasma device. *Physics of Plasmas*, 18(5):055709, 2011. → page 113

[68] John M. Dawson, Hideo Okuda, and Robert N. Carlile. Numerical simulation of plasma diffusion across a magnetic field in two dimensions. *Phys. Rev. Lett.*, 27:491–494, Aug 1971.

[69] Vivien Croes. *Plasma discharge modeling of a Hall effect thruster*. PhD thesis, 2017.

[70] Justin W. Koo and Iain D. Boyd. Modeling of anomalous electron mobility in hall thrusters. *Physics of Plasmas*, 13(3):033501, 2006.

[71] Fred Schwirzke. Electron and ion transport across a magnetic field in an arc diffusion experiment. *The Physics of Fluids*, 9(11):2250–2253, 1966.

[72] R Kawashima, K Hara, and K Komurasaki. Numerical analysis of azimuthal rotating spokes in a crossed-field discharge plasma. *Plasma Sources Science and Technology*, 27(3):035010, mar 2018.

[73] T. Lafleur, S. D. Baalrud, and P. Chabert. Theory for the anomalous electron transport in hall effect thrusters. ii. kinetic model. *Physics of Plasmas*, 23(5):053503, 2016.

[74] Jean-Pierre Boeuf. Rotating structures in low temperature magnetized plasmas—insight from particle simulations. *Frontiers in Physics*, 2:74, 2014.

[75] Hideo Okuda and John M. Dawson. Theory and numerical simulation on plasma diffusion across a magnetic field. *The Physics of Fluids*, 16(3):408–426, 1973.

[76] B B Kadomtsev and A V Nedospasov. Instability of the positive column in a magnetic field and the anomalous diffusion effect. *Journal of Nuclear Energy. Part C, Plasma Physics, Accelerators, Thermonuclear Research*, 1(4):230–235, jan 1960. → page 113

[77] F. C. Hoh. Instability of penning-type discharges. *The Physics of Fluids*, 6(8):1184–1191, 1963. → page 113

[78] Davide Curreli and Francis F Chen. Cross-field diffusion in low-temperature plasma discharges of finite length. *Plasma Sources Science and Technology*, 23(6):064001, oct 2014. → page 113

[79] Richard Hofer, Ioannis Mikellides, Israel Katz, and Dan Goebel. Wall sheath and electron mobility modeling in hybrid-pic hall thruster simulations. volume 3, 07 2007. → page 114

[80] G J M Hagelaar, G Fubiani, and J-P Boeuf. Model of an inductively coupled negative ion source: I. general model description. *Plasma Sources Science and Technology*, 20(1):015001, jan 2011. → page 116

[81] M. R. Talukder, A. K.F. Haque, and M. A. Uddin. Electron impact double ionization cross sections of light elements. *The European Physical Journal D*, 53:133–139, Jan 2009. → page 118

[82] T. Pattard and J.M. Rost. Cross Sections for (Multiple) Ionization of Ions in Collisions with Electrons. *Physica Scripta Volume T*, 80(2):295–297, January 1999. → page 118

[83] Nifs database. http://dbshino.nifs.ac.jp/. → page 118

[84] S. C Jain and Kariamanikkam Srinivasa Krishnan. The thermionic constants of metals and semi-conductors i. graphite. *Proc. R. Soc. Lond. A*, 213(1113):143–157, 1952. → page 119

[85] St. St. Lishev, A. P. Shivarova, and Kh. Ts. Tarnev. On the inertia term in the momentum equation in the free-fall regime of discharge maintenance. *Journal of Plasma Physics*, 77(4):469–478, 2011. → page 121

Appendix

The appendix for this thesis will simply be informal notes from the author. This allows for a simpler 'narrative flow'. These are pieces of information that are not significantly important to the general thesis, but may be important to those attempting to do similar work.

Ion Source Design Issues

The first iteration of the ion source design also had issues holding high voltage in other areas, such as in the delrin insulator that acted as the high voltage flange. Steel rods at high voltage were placed through to control the ion source puller. However, sparking events were constant, and eventually the rod was just replaced with a delrin rod. I have no clue why the rod would spark along the delrin insulator, as electrostatic simulations showed that electric fields are quite low here. This may have been a triple point issue, though it seems unlikely based on the spacing provided. In general, always try to avoid exposed insulators if possible from my experience.

Sputtering of the tantalum cathode onto the insulators was also an issue with the first iteration. So imagine my surprise when the second iteration, which had the cathode facing the plasma a fair distance away from the insulators, still coated it. It might be because some sputtered tantalum flies off at very low angles relative to the cathode surface. Or more likely because of parasitic discharges away from the plasma column which sputters off towards the insulators.

OES

Since non-Maxwellian EEDFs are clearly important, I did attempt to implement it into the OES in many ways. One way which got closest to matching langmuir measurements was taking several of the local minimums, and doing a weighted average of the parameters using $1/err$ as the weight. Ultimately the results were too inconsistent, and so it is unknown whether this could truly work.

Not a lot of effort was put into solving different OEF factors for a given geometry and different density profiles. The complexity, which means time drawn from the many other things on my plate with this project, pushed it to last on the list of important things to do. Such is the reality with these sort of projects. However, in the future, it would be useful to see how more complicated assumptions change the OEF results. For the sake of trends in parameters though, measuring radially and using the OEF (equation 4.28) commonly used by others is adequate, and is very commonly used by other groups as referenced in the thesis.

Langmuir Probe

An ongoing issue with the Langmuir probe in the TRIUMF ion source is that sputtering from the filament (or maybe the probe itself) was a constant issue that'd cause surface of the probe to be covered with tantalum. Make sure to shield the probe sufficiently in these types of plasmas, and also take care not to overload the probe. This can be done by avoiding the electron saturation current region, which has led to one too many probes melting on me.

Plasma modeling

I do believe that it is possible to make a better 2-D model. This could be done by completely re-making a set of PDE solvers in COMSOL™ which include the ion and electron velocity and energy equations. However, it would have to be done over many small steps with careful testing of each step with known theoretical results. It would take time, but would probably be worth it if it can improve on the models in this thesis, yet still be much shorter to solve then PIC codes. However, convergence with several non-linear PDEs might take certain initial conditions. For

the models described in this thesis, it was already a bit of a pain to get the right initial conditions that can be resolved.

Such a code could also include multiple electron distributions, such as a bi-Maxwellian, to better improve the model. However, at this point we might end up with the same issue, where a set of equations with many unknown variables might have several ways to achieve the same solution, some of which may be unrealistic.

Hot Cathode Arc

It's a shame that the bias power supply failed before the ISTF left NZ, then after several months of shipment delays thanks to a certain pandemic, another power supply failed. Thus the data taken in the hot cathode regime is incomplete. Some notes on this operation mode are as follows.

The capacitive discharge circuit, whilst fine for igniting the source when it couldn't ignite for unknown reasons, was not as effective as simply increasing the gas flow so that it could be more easily ignited with the main power supply. It may be that other arc plasma igniters we used as examples did not have high gas pressures they could use to ignite the arc discharge as we did.

The OES when used on the hot cathode ion source used a different light from Oceanoptics which is supposed to have a blackbody output at 2800 K. However, lack of other technical details (how closely it follows this for example) are not given despite several email exchanges, so there's very little reason to trust this. It did still give decent results for trends when compared to the Langmuir probe. However, when applied to the hot cathode PIG source, no observed trends could be seen when changing magnetic field or arc current (the controllable for this mode). This may be because at such high current densities the OES model fails due to greater interactions of energetic heavy particles, more Coulomb collisions, existence of plasma waves, significance of higher energy excited states in discharge, etc. Due to lack of experimentation, it is unknown at the moment what the issue may be. The usual trends of increased electron density and decreased electron temperature with gas flow were still observed though, this seems quite universal.

When extracting from this mode, very high bias currents past 35 mA were observed. The helium ion current went up with each input parameter of gas flow,

magnetic field, and arc current, which implies that the electron density within the plasma also goes up with each. This makes sense due to the same arguments made for the cold cathode, except in this case a higher arc current means greater cathode electron emission, and thus greater electron density. α-currents were observed up to about 300 uA in a preliminary dataset, which is quite promising.